Synthesis of a nickel (II) photomagnetic switch

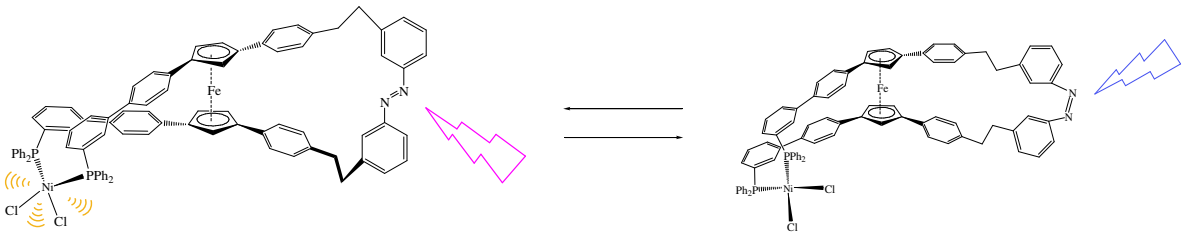

Thèse présentée à l'Institut de Chimie

Faculté des Sciences

Université de Neuchâtel

Pour l'obtention du grade de docteur ès sciences

Par

Yves Casta

Thèse soutenue le 25 novembre 2008 devant le jury composé par :

Prof. Ward Thomas, directeur de thèse, Université de Bâle, Suisse

Prof. Decurtins Silvio, rapporteur, Université de Berne, Suisse

Dr. Therrien Bruno, rapporteur, Université de Neuchâtel, Suisse

Prof. Kinbara Kazushi, rapporteur, Université de Tohoku, Japon

Université de Neuchâtel

2009

Université de Neuchâtel

FACULTE DES SCIENCES
Secrétariat-Décanat de la faculté
Rue Emile-Argand 11
CP 158
CH-2009 Neuchâtel

IMPRIMATUR POUR LA THESE

Synthesis of a Nickel (II) Photomagnetic Switch

Yves CASTA

UNIVERSITE DE NEUCHATEL

FACULTE DES SCIENCES

La Faculté des sciences de l'Université de Neuchâtel,
sur le rapport des membres du jury

MM. T. Ward (directeur de thèse), B. Therrien,
S. Decurtins (Berne) et K. Kinbara (Tohoku, Japon)

autorise l'impression de la présente thèse.

Neuchâtel, le 13 février 2009

Le doyen :
F. Kessler

UNIVERSITE DE NEUCHATEL
FACULTE DES SCIENCES
Secrétariat - décanat de la faculté
Rue Emile-Argand 11 - CP 158
CH-2009 Neuchâtel
Félix Kessler

Téléphone : +41 32 718 21 00 E-mail : secretariat.sciences@unine.ch www.unine.ch/sciences

Keywords: Nanotechnologies, molecular machines, molecular scissors, spin crossover, ferrocene, nickel and rhodium complexes, phosphinated scissor ligand, UV-visible photoisomerization, *trans-cis* isomerization.

Mots-clés: Nanotechnologies, machines moléculaires, ciseaux moléculaires, spin crossover, ferrocène, complexes de nickel et de rhodium, ligands ciseaux phosphinés, photoisomérisation, isomérisation *trans-cis*.

Table of contents

Acknowledgements

Foremost, I would like to thank Professor Thomas Ward for having me in his laboratory during 4 years and giving me the chance to work in the field of nanotechnology. I also thank him for giving me the unique opportunity to work in Japan for a year and for the trust and confidence he had in the subject during difficult times.

I would like to thank the members of the jury for reading and judging this doctorate: Professor Thomas Ward, Professor Silvio Decurtins, Doctor Bruno Therrien and Professor Kazushi Kinbara.

I would also like to address all my gratitude to, Professor Kazushi Kinbara, Assistant-Professor Takahiro Muraoka, Professor Takuzo Aida, Shinji Nara and especially Eri Hirahara. They all participated in making my stay in Japan, an unforgetable memory.

I would like to show all my gratitude to all my colleagues and the people at the University of Neuchâtel for all the great memories. Particularly Manuel Tharin, Christophe Thomas, Sébastien Lanaspèze, Anca Pordea, Julien Pierron, Thibaud Rossel, Inès Hafner, Jean-Christophe Prost, Johan Mattsson and Christelle Schenk. My thanks also go to Tony Keene and Silvio Decurtins from the University of Bern for accepting me in their laboratory and for their immensely appreciated help.

Finally I would like to dedicate this thesis to my Mother, Sister, Father, Mohamed, Ayla, Sadri, Raphaël, Skagit, Laurent, Marc and Silvio for their unconditional support during these 4 years. It would not have been possible without them. I also dedicate this work to Virginie, who pushed me towards chemistry and made this thesis a reality.

Abstract

Synthesis of a nickel (II) molecular photomagnetic switch

The purpose in this research is the development of a molecular photomagnetic switch based on the magnetic properties of four coordinate nickel (II) complexes. A Cambridge structural database search of all $[NiCl_2(PR_3)_2]$ complexes reveals that the four coordinate geometry around nickel correlates with the P–Ni–P bite angle. Indeed, large P–Ni–P bite angles favour tetrahedral and thus paramagnetic complexes, while small bite angles yield square planar, diamagnetic complexes. Introduction of a photoisomerizable moiety within a diphosphine backbone may thus allow a reversible photoinduced interconversion between the two nickel spin states. We present the coordination properties of a diphosphine derived from a ferrocene moiety bearing remote azobenzene functionality. The photoisomerization of the azo group induces a movement of the scissors blades (diphosphines) to trigger a change in the coordination of the nickel.

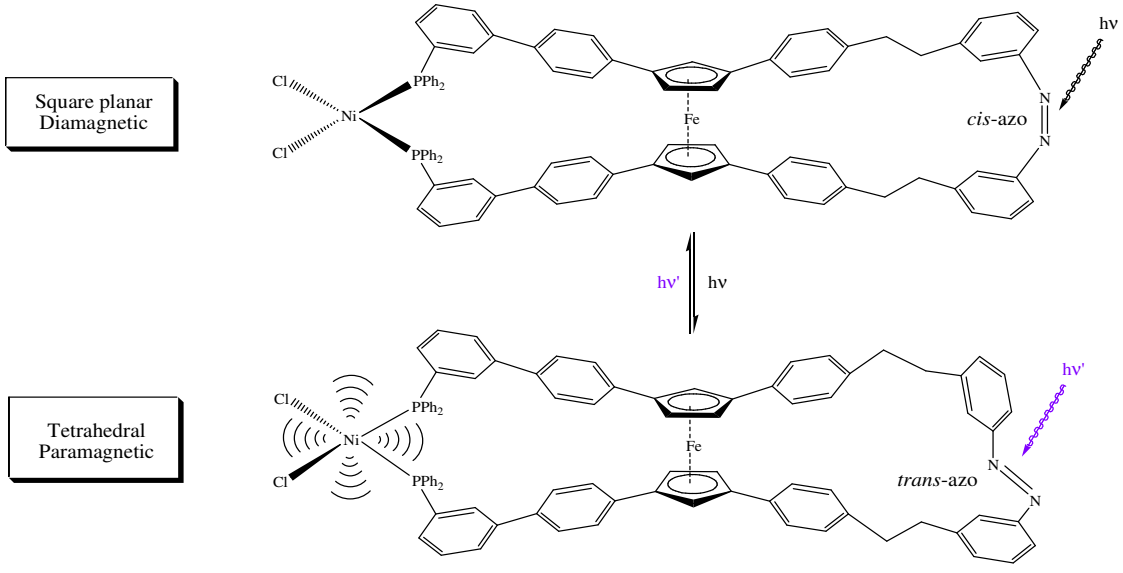

Résumé

Synthèse d'un interrupteur moléculaire photomagnétique de nickel (II)

Le but de cette recherche est le développement d'un interrupteur moléculaire photomagnétique basé sur les propriétés magnétiques des complexes de nickel (II) de coordination quatre. Une recherche dans la base de données stucturale de Cambridge (Cambridge structural database) de tous les complexes de type $[NiCl_2(PR_3)_2]$ révèle que la géométrie autour du nickel est en corrélation avec l'angle de coordination P–Ni–P. En effet, de grands angles de coordination P–Ni–P favorisent des complexes tétraédriques paramagnétiques, alors que de petits angles fournissent des complexes plan carré diamagnétiques. L'introduction d'une fonction photoisomérisable à l'intérieur de l'architecture de la diphosphine pourrait ainsi permettre une interconversion photoinduite réversible entre les deux états de spin du nickel. Dans cette thèse, nous présentons les propriétés de coordination d'une diphosphine chélatante, dérivée de ferrocène, contenant une fonction azobenzène isolée. La photoisomérisation du groupement azo induit un mouvement des lames (diphospohine) de ciseaux qui déclenche un changement de coordination du nickel.

- Chapter I -

Introduction

1 Molecular machines

The recent explosion of results in the field of molecular biology has demonstrated the crucial role of biological molecular machines in nature and our daily life. These protein-based molecular machines are much more sophisticated than their present synthetic equivalent and are involved in many biological events, mainly those of cell activities. The active research on these machines has allowed a better understanding of the mechanisms of motions at the molecular level and inspired chemists around the world to develop new artificial molecular designs. In this introduction, we first deal with natural biological molecular devices in order to underline the key points of their structures, working and mechanism of motion. On the other hand we compare some of the existent artificial molecular machines with their biological counterparts and discuss their potential applications. This thesis has the purpose to build a photomagnetic switch based on the electronic properties of nickel (II) which could potentially lead to information storage at the molecular level. The presentation of this new artificial molecular machine appears in the final section of the introduction.

1.1 Biological Molecular Machinery [1]

1.1.1 ATP synthases

ATP synthases are biological molecular rotary motors made of various proteins that are omnipresent in the mammalian cells. This device synthesizes adenosine triphosphate (ATP) molecules through its rotary motion [2-7]. It is made of two distinctive parts, F_0 and F_1 (figure I.1), whose crystal structures have both been solved [8]. The F_0 component—in the case of mithochondrial ATP synthase—is immobilized in a lipidic membrane and acts as a stator, whereas F_1 has a spherical structure and bears catalytic sites in the β-unit for the synthesis of ATP. The process is triggered by proton-motive force in the rotor that translates its rotary motion through the γ shaft.

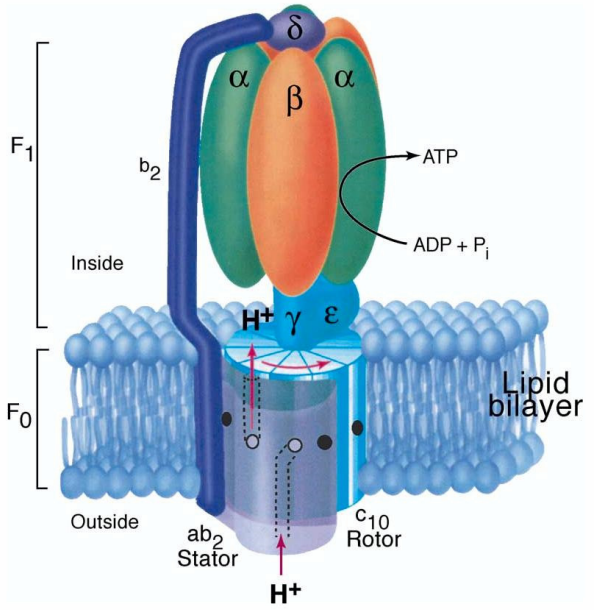

Figure I.1: Schematic representation of ATP-synthase, a biological molecular motor that provides fuel to the cell by synthesizing ATP [9].

It then activates the reaction of adenosine diphosphate (ADP) and phosphate (P_i) into ATP. The motor also operates in the opposite direction generating a proton flow which travels to the outside of the membrane. ATP synthase is thought to revolve at more than 100 Hz (revolutions/sec), which is sufficient to potentially produce a turnover in ATP equivalent to the weight of a human body each day [10].

1.1.2. Bacterial flagella

Many kinds of bacteria use rotational motors, located at the cell's outermembrane, in order to swim in their environment [11,12]. Such motors are highly sophisticated and composed of different elements made of various proteins (figure I.2). Fixed in the membrane, the motor is driven by a proton channel and transmits its rotation to the hook and filament through the rod. The flagellum, which acts as a propeller, is a huge protein conjugate (10-15 μm) composed of more than 10'000 elements of flagelin (FliC). Namba and coworkers have determined that the filament is built up with protofilaments that can adopt either clockwise or anticlockwise configurations depending on their twisting direction [13]. Judicious arrangements of the two protofilaments allow many different helical shapes of the filament and therefore a large variety of motions. The motor has a frequency of more than 16 000 revolutions per minutes which is faster than a formula 1 engine. Even more impressively, the energy from the hydrolysis of ATP is almost entirely converted into rotational energy. Bacteria were also found to attach and propel 10 μm beads of polydimethylsiloxane [14]. It suggests the future of nanotechnologies which will certainly profit from the synergy between synthetic and natural molecular devices.

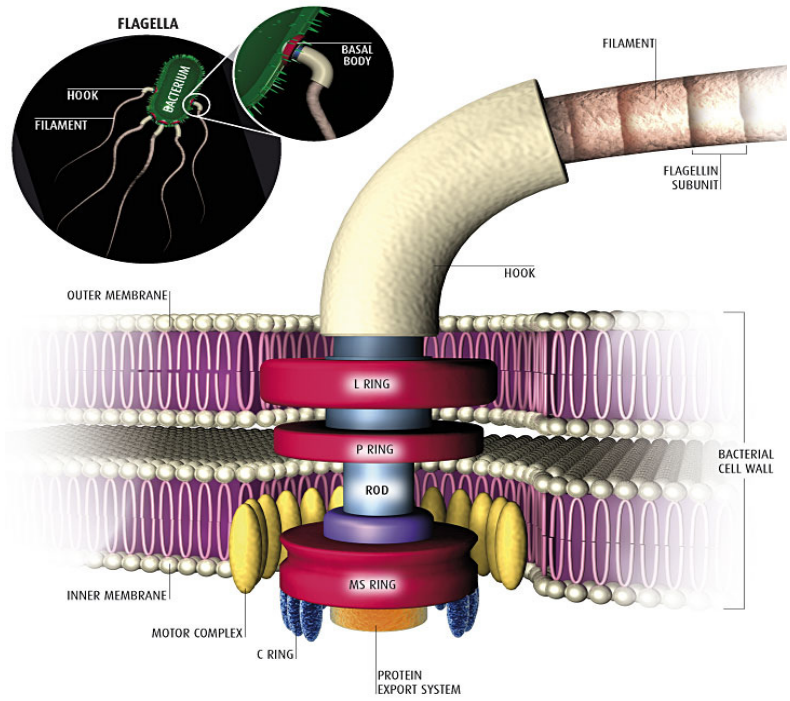

Figure I.2: Schematic representation of a bacterial flagellar motor [15].

1.1.3. Myosins

Myosins are cytoplasmic proteins that literally walk unidirectionally along actin filaments in the cell [11]. These actin tracks are made of two helical strands, winded up around each other, composed of g-actin protein monomers [16, 17]. The motion along the filament is fueled by the hydrolysis of ATP into ADP. Myosins participate in many processes of cellular activities such as vesicle transport, cell locomotion, membrane trafficking, cytoplasmic streaming and signal transduction [18-21]. For instance, myosin II is a protein composite that was already discovered in 1865 [22]. It contains one heavy and two light chains and plays an active role in the contraction of muscles. Indeed, the muscle cells (myofibrils) of a skeletal muscle contain large cylinders of sarcomeres, composed of actin filaments and intercalated with immobilized myosins II, as presented in figure I.3. The simultaneous motion of myosins pushes the actin

filaments away creating a “piston like” shortening of the sarcomeres at the cellular level, which is translated in a macroscopic contraction of the muscle.

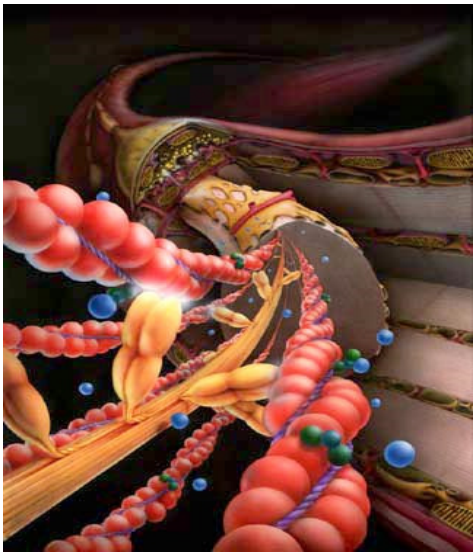

Figure I.3: Schematic illustration of muscle cells, which are mainly built up with arrays of sarcomeres bearing myosins II [23].

1.1.4. Kinesins

Kinesins are other kind of molecular motors that move along microtubules [24] and are involved in the transport of vesicules, organelles and messenger RNAs, as illustrated in figure I.4. Conventional kinesins are made of several heavy and light chains proteins that serve as cargo binding on one end and as a motor on the other end. The motor head part moves unidirectionaly, using the energy produced by ATP hydrolysis, on the microtubules [11]. Those microtubules are composed of an assembly of α and β-tubulin dimers that form large hollow tubes [25,26]. Kinesins are also involved in chromosomal and spindle movements during mitosis and meiosis. In this process, tubulin grows from the two centrosomes towards the center of the cell and permits the transport of chromosomes by kinesins to the equator.

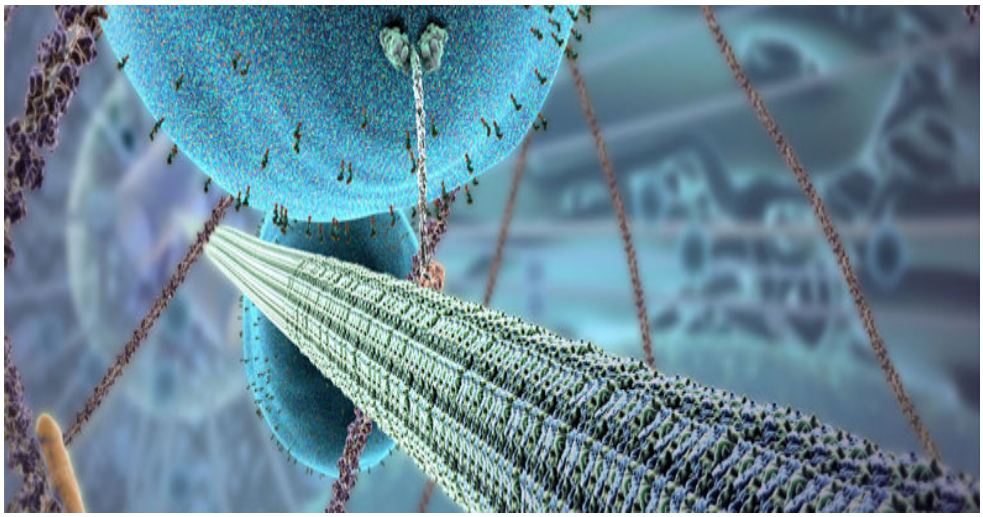

Figure I.4: Artistic view of a kinesin transporting a cargo along a microtubule in a cell [27].

1.1.5. Vision mechanism

The retina of all vertebrate is composed of a lipidic membrane which covers the back of the eye and is linked to the brain through the optical nerve. This membrane is embedded with photoreceptive cells called rods and cones that have similar functions. Rods are much more sensitive than cones but cannot distinguish colors. They are especially requested at night, because they can absorb bigger amounts of light, but are only able to provide a black and white image to the brain. On the other hand, the three primary colors cones supply a colorful vision to vertebrates during the day. The external segment of a rod is composed of a plasmic membrane in which opsine proteins are contained. The hollow centers of opsines have an adequate shape for *cis*-retinal molecule and this conjugate is called rhodopsine. When *cis*-retinal is irradiated with light, it undergoes photoisomerization and forms *trans*-retinal as sketched in figure I.5.

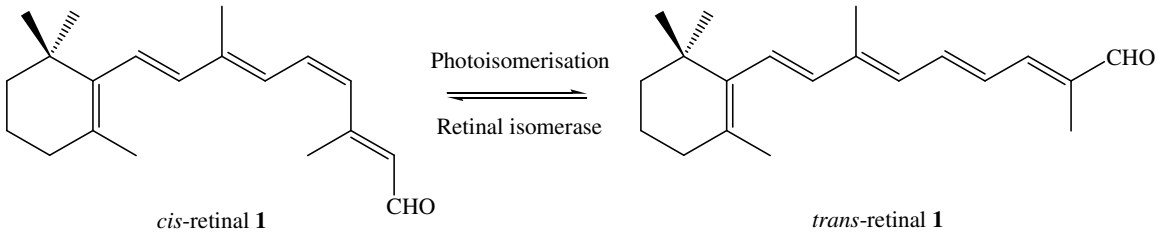

Figure I.5: Schematic representation for the photoisomerization of *cis*-retinal into *trans*-retinal.

As depicted in figure I.6, configurational changes due to isomerization generates a rise in volume of the guest molecule that spaces out the tubes forming the opsine protein.

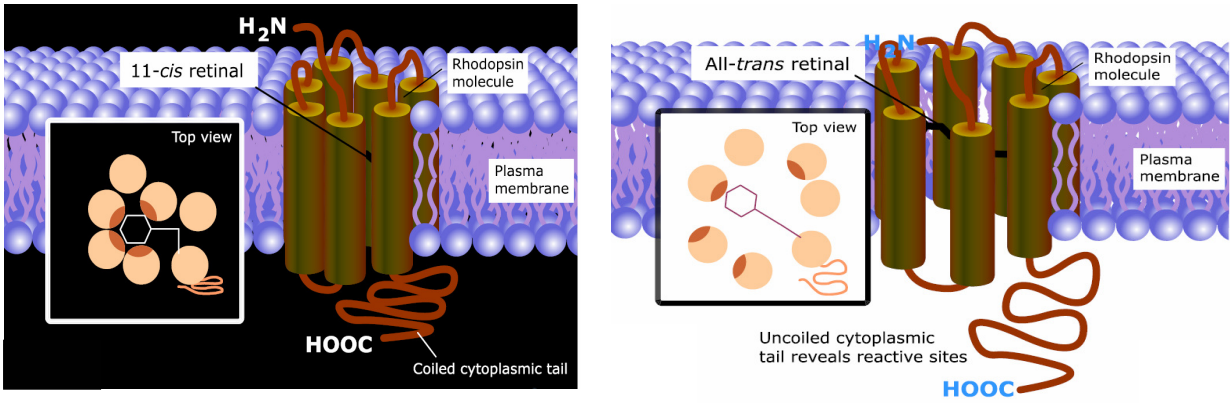

Figure I.6: Illustration of the mechanism that leads to a reactive tail through photoisomerization of a *cis*-retinal molecule [28]; left image, in the absence of light; right image, in the presence of light.

When this rise in volume occurs, the cytoplasmic tail uncoils and reveals a carboxylic acid reactive site. Such activated rhodopsine provokes an enzymatic cascade which ends with the hydrolysis of cyclic guanosine monophosphate (cGMP) protein by phosphodiesterase. The scarcity of cGMP around the membrane induces a closing of cationic gates as displayed in figure I.7. The membrane becomes thus hyperpolarized and electrical impulses are sent to the brain. Interpretation of these signals by the vision cortex translates them into images.

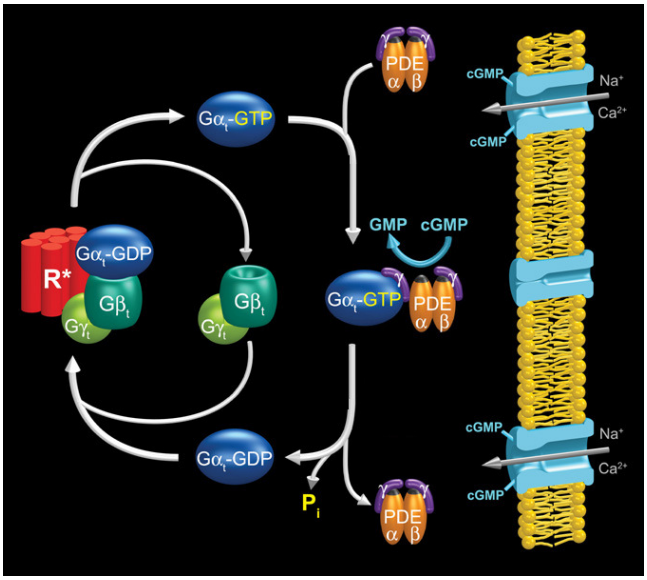

Figure I.7: Phototransduction cascade in which an activated rhodopsine triggers the shutting of the cationic channels [29].

1.1.6 Chaperonins

Another kind of biological molecular machines are chaperonins which amongst others help the folding process of unfolded proteins [30]. GroEL, one of the most common chaperonins, ressembles a large tube built by two layers of seven circularly arranged proteins. ATP binding to one of the heptameric ring provokes a negative allosteric effect on the second ring which prevents ATP from binding [31]. The device becomes thus asymmetric and allows the cochaperonin GroES to cap the apical domain of GroES (dark blue in figure I.8). This GroEL-GroES combination then captures the unfolded proteins which travel inside the hollow center of the tube which is hydrophilic and thus folds the protein. Binding of ATP on the uncapped heptamer ring is now allowed and the whole conjugate undergoes dramatic conformational changes which releases the folded protein and the GroES cochaperonin.

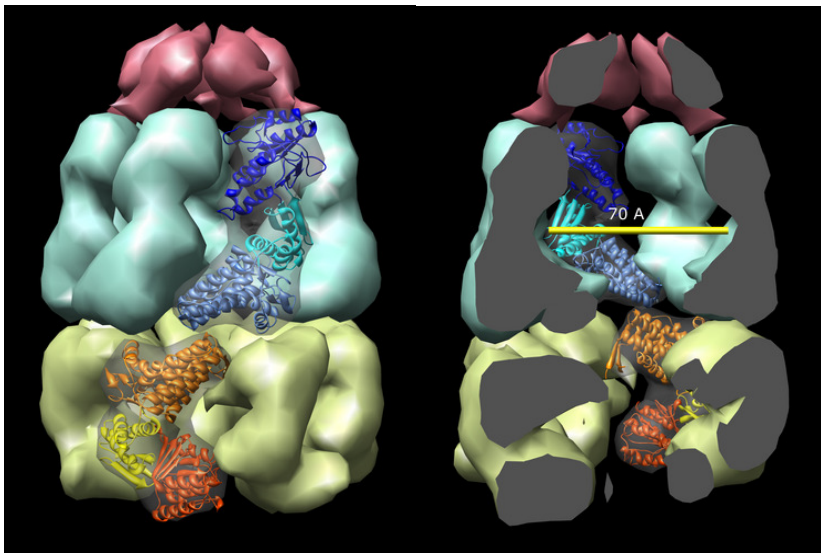

Figure I.8: Representation of a half GroEL chaperonin capped by cofactor GroES during the biological folding process of protein

Recently, Aida and coworkers have successfully captured cadmium sulphide nanoparticles in GroEL and HB8 chaperonins [32]. Amazingly, at 4°C, the nanocomposite preserves the light emitting properties of CdS for more than a year. Without this encapsulation, such nanoparticles rapidly undergo aggregation and lose their emission in only two hours. However, by addition of ATP under physiological conditions (Mg^{2+} and K^{+}), the nanoparticles are readily released from the chaperonins.

2. Artificial molecular machines

Biological molecular machineries described in section 1. have benefited from millions of years of evolution and are much more sophisticated than the present artificial molecular machineries. Understanding of the mechanism and the motion of these biological devices at a molecular level is therefore crucial for bridging the gap between the two fields and could lead

to new useful hybrid devices. As information technology has revolutionized our daily lives in the last decades, the quest for miniaturization is expanding rapidly. One of the goals of these researches in nanotechnology is to find switching and memory elements as small as a single molecule. They could lead to smaller and faster computer chips as well as bigger storage capacities on very small surfaces. Using molecular switches in biosensors or drug delivery systems is expected to revolutionize biomedicine. The construction of basic elements such as muscles, motors, brakes, turnstile, rotational modules and scissors have already been achieved by chemists around the globe and are the premises of nanotechnology. In the following section, we will focus on molecular switches which are essential for controlling motion at the molecular level.

2.1. First generation of molecular switches

The concept of artificial molecular machines was already introduced by Feynman in 1960 [33] in a lecture in which he highlighted the enormous potential of molecular devices. Among these first synthetic molecular machines are molecules synthesized by Shinkai and coworkers bearing crown, azacrown ethers and azo groups. Thanks to the azo group's capability to photoisomerize, such compounds are able to switch reversibly and induce a conformational change. For instance, molecule **2** contains two crown ether linked to one another by an azobenzene hinge as displayed in figure I.9. This device undergoes butterfly-like motion when irradiated by UV and visible light repeatedly [34,35]. The result is that *trans*-**2** preferably binds two Na^+ cations whereas *cis*-**2** preferably encapsulates one Rb^+ ion. Furthermore, the presence of Rb^+ ions in solution increases the proportion of *cis*-**2** at the photostationary state and decreases the rate of the thermal *cis-trans* transformation.

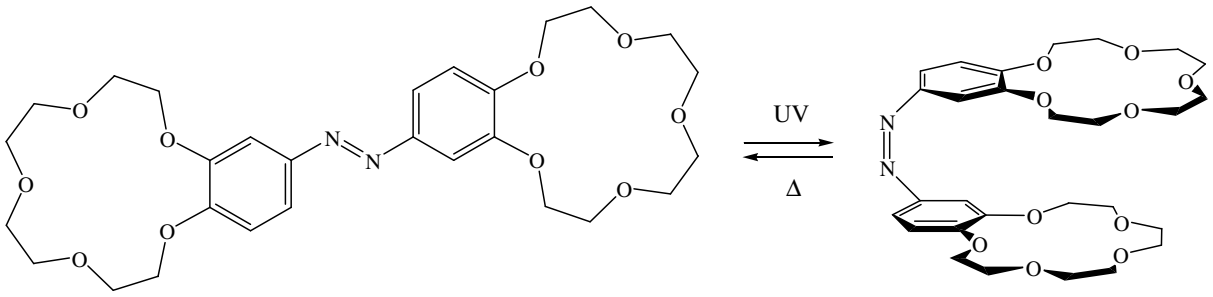

trans-**2** *cis*-**2**

Figure I.9: One of the first examples of a molecular switch.

The same research group developed the "tailbiting"crown ether switchable receptor **3** (figure I.10) [36]. In the positively charged *cis*-**3** form, intramolecular binding of the ammonium ion to the crown ether prevents recognition of other cations. Thermal isomerization to give *trans*-**3** restores the original properties of the crown ether towards alkali metal ion. As expected, the power of complexation is much higher in the *trans*-form than in the *cis*-form.

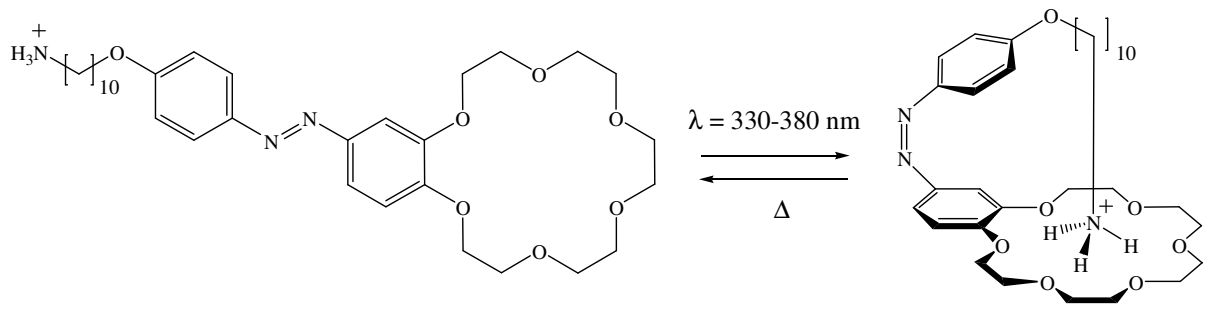

trans-**3** *cis*-**3**

Figure I.10: Molecular switch that bites its own tail upon UV irradiation and comes back to its original configuration when heated.

When Azacrown ether **4** is isomerized upon irradiation, changes in the affinity towards alkali metal ions are observed [37]. Shinkai and coworkers have also built devices containing two azobenzene unit bridged by azacrown ether unit (figure I.11). They discovered that

photoisomerization of the two azobenzene of molecule **5** is cooperative meaning that only *cis-cis* and *trans-trans* forms are observed [38].

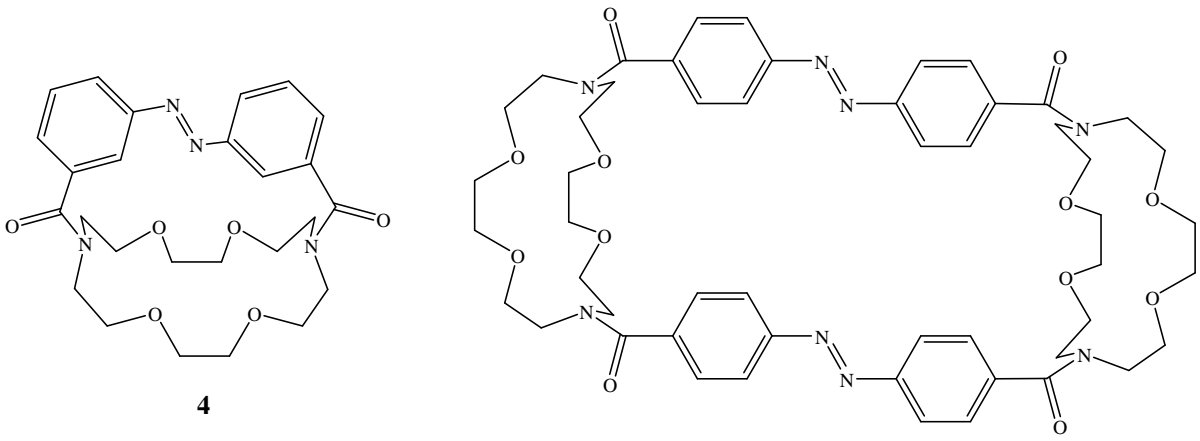

4 **5**

Figure I. 11: Isomerizable crown ether based molecular cages.

2.2. Photochromic switches

The term "photochromism" is defined as a reversible light-driven transformation between two isomers which results in different geometries as well as chemical and physical properties [39]. Alterations in absorption spectra are one of such property changes. Phototochromism itself has therefore the nature of a switch inherent to it. There are two types of photochromic switches. The first type, designated as the T-type (thermally reversible) is of no big interest as these types of chromophores revert thermodynamically to their original isomers in the dark. Most chromophores belong to this category and cannot be used as molecular systems as they undergo reverse isomerization automatically due to one unstable state. For applications, thermal irreversibility at room temperature between the two isomers is indispensable. Such particularity is rare and only a few derivatives containing diarylethenes, azo and furylfulgides

functions can boast about such performances. They are called P-type (photochemically reversible). The principal aspect that distinguishes these different thermally stable chromophores is the fatigue-resistance which is crucial for applications in need of long lasting molecular switches. Diarylethenes have proven to be the most resistant to fatigue and are therefore particularly suitable for applications [41].

2.2.1. Diarylethenes

Most of diarylethenes undergo photoisomerization and cyclization upon UV irradiation and turn back to their original form upon visible light irradiation. Examples include a colorless hexane solution of **6a** (figure I.12), which changes to blue (**6b**) when irradiated with light at 313 nm [42].

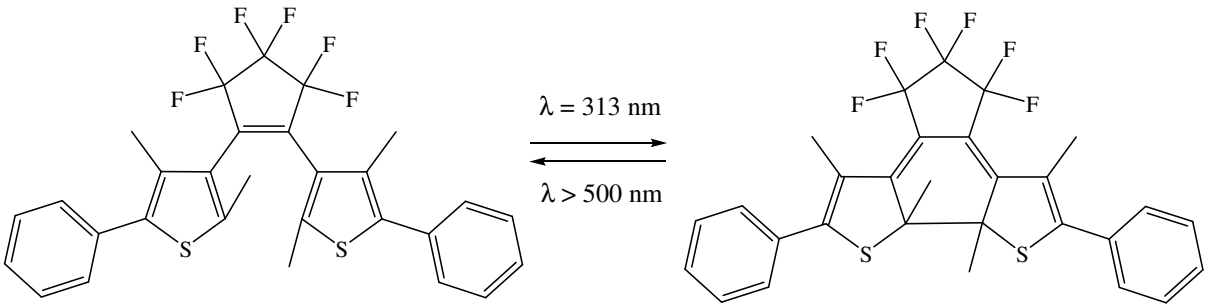

Opened-ring isomer **6a**
colorless

Closed-ring isomer **6b**
blue

Figure I.12: Concept of the isomerization of diarylethenes switching from opened-ring to closed-ring that leads to a color change of **6a**.

The closed-ring isomers of a diarylethenes are in most cases thermally stable and don't revert to the opened-ring isomer. Irie and Nakamura have determined that this thermal stability is due to the low aromatic stabilization energy when the aryl groups are furanes, thiophenes or

thiazole rings [43]. On the contrary, the closed-ring isomers of diarylethenes bearing pyrrole, indole or phenyl rings have high aromatic stabilization energy and are therefore thermally unstable [44]. As depicted in figure I.13, the photogenerated pyrrole diarylethene **7b** reverts back to its original form **7a** in 37 s at 25°C.

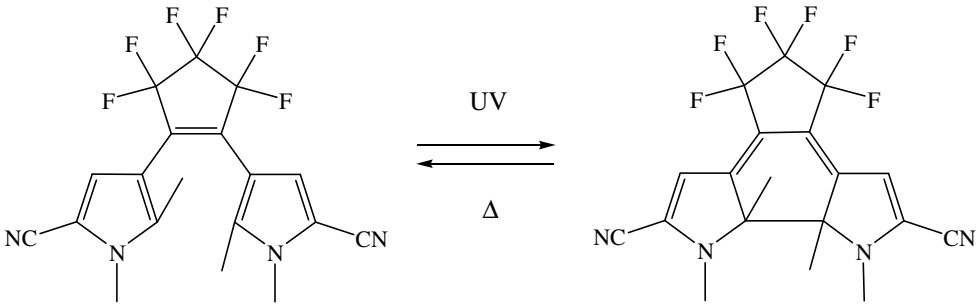

Opened-ring isomer **7a** Closed-ring isomer **7b**

Figure I.13: Thermally unstable diarylethene **7**.

Indeed, this thermal behavior ascertains the theoretical prediction that thermal stability is linked to the aromatic stabilization energy of the aryl groups.

2.2.1.1. Diarylethene molecular switches

Crown ether with diarylethene units participates in host-guest guest interactions and works as switches. Takeshita and Irie have demonstrated that the opened-ring form of such compounds form a “sandwich” complex with large metal ions [45,46]. After photoisomerization, the closed-form ring becomes too rigid and releases the cation. Two-phase extractions of alkali metal picrates were carried out and the variation of the concentration in the aqueous phase was used to determine the power of extraction of such systems. An example of this phenomenon is displayed in figure I.14, where a solution of the opened-ring isomer **8a**

extracted up to 50 % potassium and rubidium picrates in the organic phase. Upon ultraviolet (UV) exposure with a 313 nm light, the extraction capability dropped to 10 %. This system acts as molecular tweezers which are able to readily catch and release metal ions through action of light. They could potentially find applications in the active transport of molecules and metal ions.

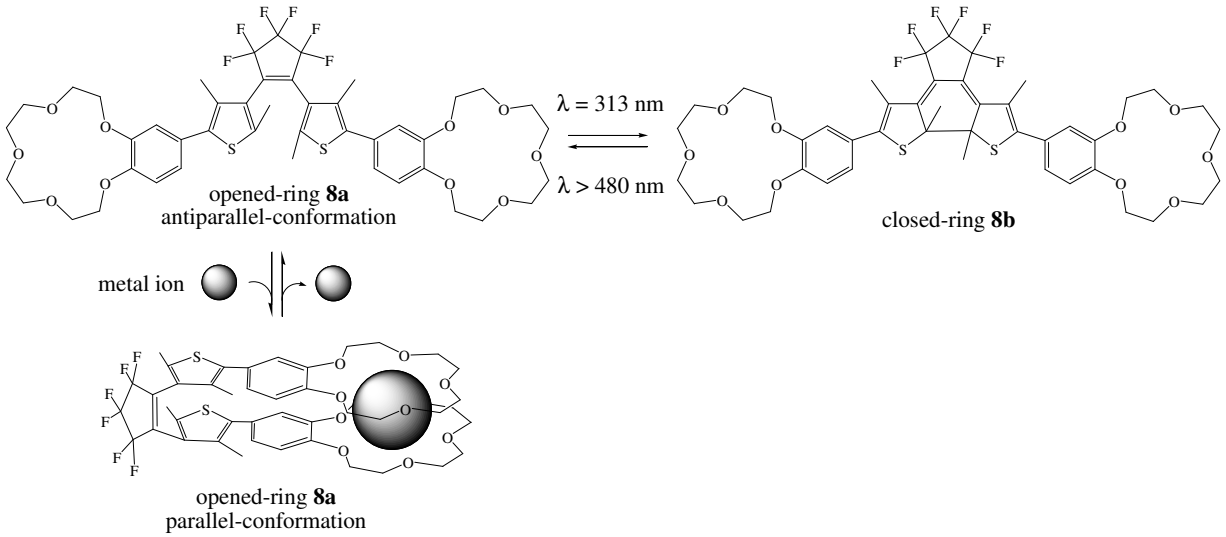

Figure I.14: Crown ether functionalized diarylethenes **8** that act like tweezers by light controlled releasing of metal ions.

In the same spirit, glucose molecules can be captured and released by modified diarylethene bearing boronic acid moieties by photoirradiation [47]. Saccharides are composed of many hydroxyl groups and form esters with the boronic acid part of the opened-ring form of the diarylethene. When irradiated to the closed-ring form, the two boronic acids are too far from each other and cannot form esters with the sugars.

2.2.1.2. Photoelectrochemical switches containing diarylethenes

The control of reversible switching of electrochemical properties through light irradiation is crucial for the elaboration of electronic molecular devices.

For this purpose, Uchida and Irie have studied the electronic behavior of both closed and opened-ring upon photoisomerization [48]. As presented in figure I.15, the position of the sulfur atom in the thiophene rings influences the π-electron delocalization. Indeed, the electrons are delocalized in the entire closed-ring isomer **9b**. On the other hand, in the opened-ring isomer **9a**, π-electrons are localized in the thiophene rings. Thus, in the closed-ring isomer **9b**, X and Y constituents are able to interact with each other trough the π-conjugation. As this is not the case in **9a** and no interactions are possible between X and Y, the system can be switched between the two states by photoirradiation.

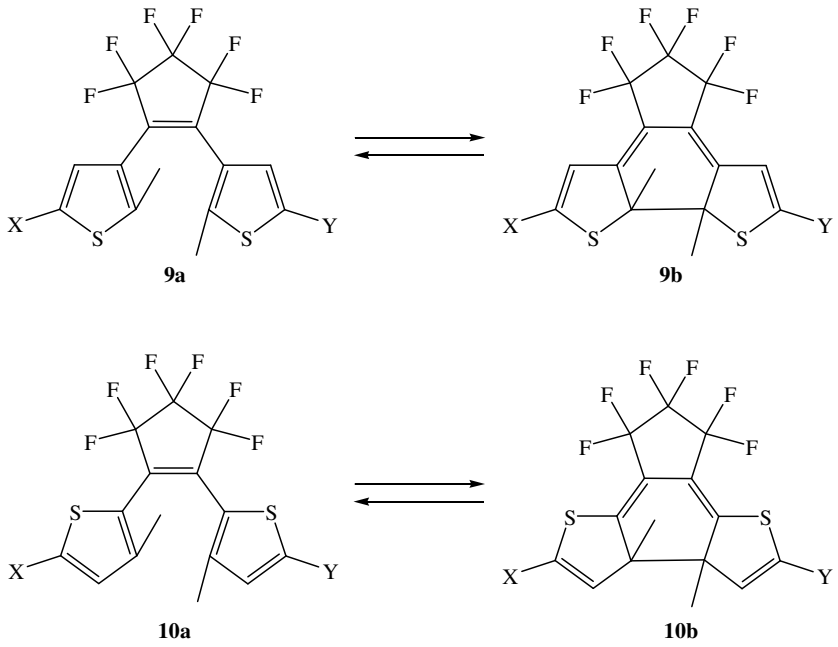

Figure I.15: Interactions between X and Y substituents depending on the position of the sulfur atom in the thiophene ring.

On the contrary, when the two thiophene rings are attached through their 2-positions as in **10a**, π-electrons are delocalized in the entire molecule and X and Y can interact with one another. The electrons in **10b** being localized in the central cyclohexadienyl ring, X and Y are unable to interact strongly.

A concrete example of such a phenomenon has been reported by Lehn and coworkers and is described in figure I.16 [49,50]. The two positively charged pyridinium ion moieties interact only weakly in **11a**. The opened-ring isomer is therefore in the "off" state. On the other hand, the two pyridinium ion groups in the closed-ring form **11b** can interact through delocalization of π-electrons and give rise to the "on" state.

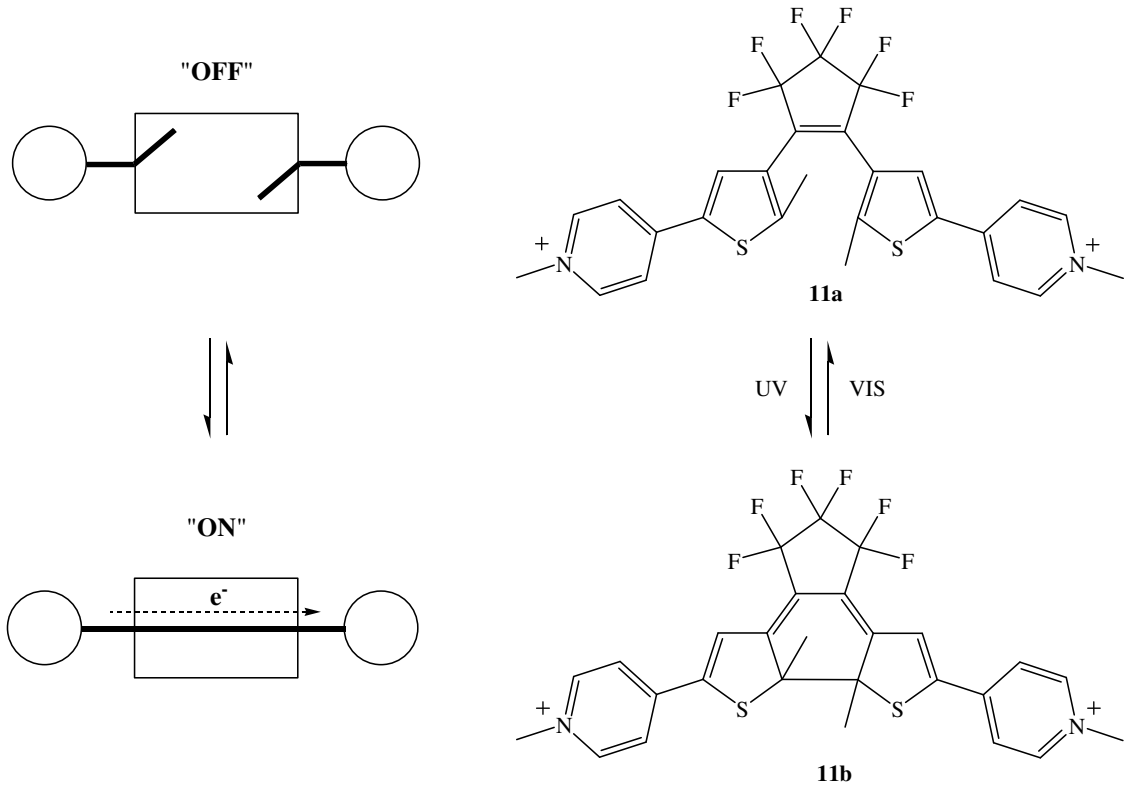

Figure I.16: Control of the electron flow through photisomerization of diarylethene **11**.

Cyclic voltametry showed that electrochemical processes occurred only in the closed-ring isomer **11b**. This system can be used as a switchable molecular wires in which electron flow is controlled by light irradiation.

2.2.2. Fulgides

Bismethylenesuccinic anhydrides containing a phenyl ring on the methylene carbon atom are usually known as fulgides, they were first synthesized and studied early in the 20th century by Stobbe [51]. As depicted in figure I.17, the fainted colored E-isomer of molecule **12** undergoes cyclization upon UV irradiation and turns into the deeply colored isomer **12C**. Concomitantly, the E-form is also transformed into the colorless **12Z** form through simple E-Z isomerization. While all forms absorb UV light, interconvertions between them occur until a photostationary state is reached. Since **12C** is the only form to absorb visible light, it disappears completely upon visible light irradiation.

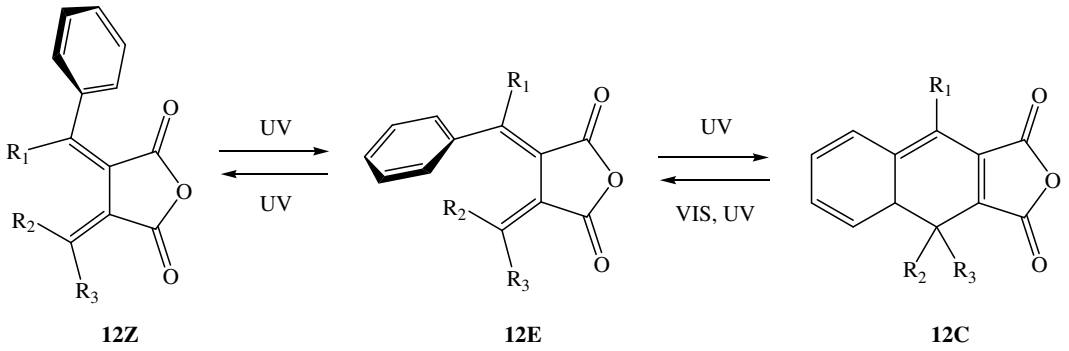

Figure I.17: Different possible forms of fulgides **12**.

As variation in absorption spectras is one of the requirement to exploit photochromism, the interconversions between the E and C-forms is commonly called fulgide photochromism. The

anhydride function of fulgides is easily derivatized and allows the creation of a wide variety of photochromic compounds. Nevertheless until 1981, fulgides were all thermally reversible and therefore not particularly interesting for application purposes. By introduction of furane derivatives instead of the phenyl group, Heller and coworkers have obtained thermally irreversible compounds for the first time [52]. For example, furylfulgide **13** displayed in figure I.18.

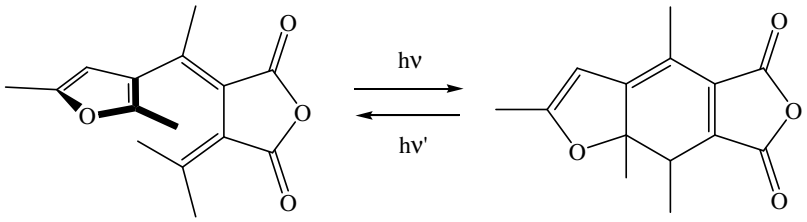

13E **13C**

Figure I.18: Schematic representation of a thermally irreversible furylfulgide **13**.

2.2.2.1. Fluorescence switching in fulgides

E-form furylfulgides rarely emit fluorescence unless they contain a fluorescent moiety. On the other hand, cyclized C forms often generate fluorescence at low temperatures. With this in mind, Port and coworkers introduced a system in which fluorescence is controlled by photoisomerization [53,54]. A fulgimide bearing an anthracene function that serves as an antenna (energy donor) on the thiophene ring (figure I.19). An aminocoumarin, used as a luminescent moiety (energy acceptor), is introduced on fulgimide nitrogen. When **14E** is irradiated with 400 nm light, the anthracene group is excited to a higher energy level. This energy is transferred through the E-form core on to the coumarin which emits fluorescence. On the other hand, this fluorescence decreased after photocyclization to **14C** with 520 nm light. Indeed, the excited state of the C-form part is lower in energy than that of the aminocoumarin acceptor and deactivates radiationless to the ground state. The C-form core

thus acts as an energy trap which lowers luminescence. Hence, the system is able to switch from low to high fluorescence thanks to photochromism.

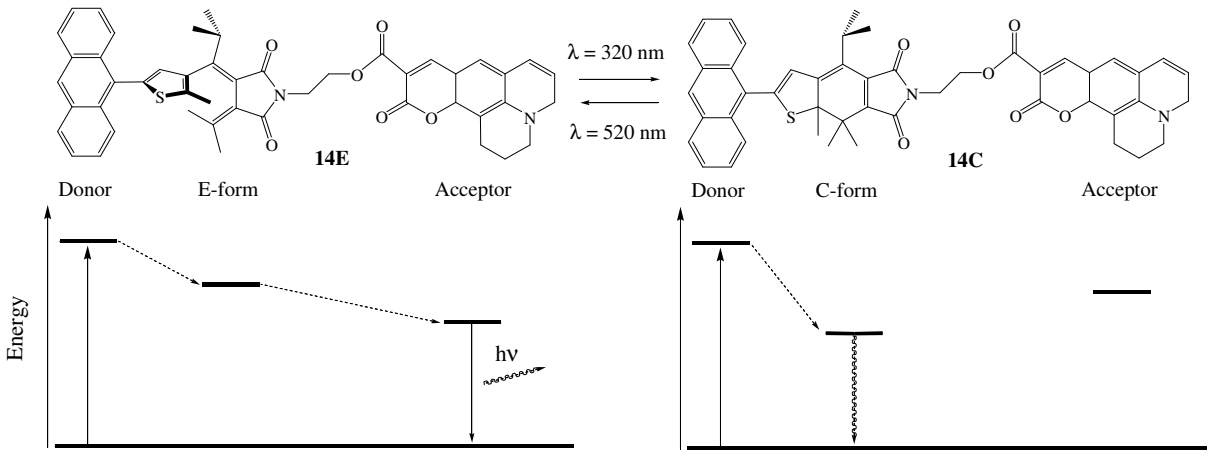

Figure I.19: Switching of luminescence of compound **14** upon illumination through energy trapping.

2.2.3. Molecular motors

Unidirectional chiral molecular motors that mimic the rotational motion of ATP synthase and flagelar motors have been reported by Feringa and coworkers in 2003. A prototype of such motor is sketched in figure I.20. Molecule **15a** contains a tetrasubstituted photoisomerizable alkene bearing two phenanthrene derivatives. Steric hindrance of the phenanthrene substituents of the alkene introduces helical chirality in the system. Initially, the alkene adopts a *trans*-conformation which is isomerized into a highly strained *cis*-isomer **15b** upon irradiation at a wavelength longer than 280 nm at -55°C. Concomitantly, the methyl substituents of the cyclohexane ring move from axial to equatorial position. When heated at 20°C, **15b** undergoes a flipping motion of the aromatic rings around the alkene to give an oppositely twisted helical isomer **15c**.

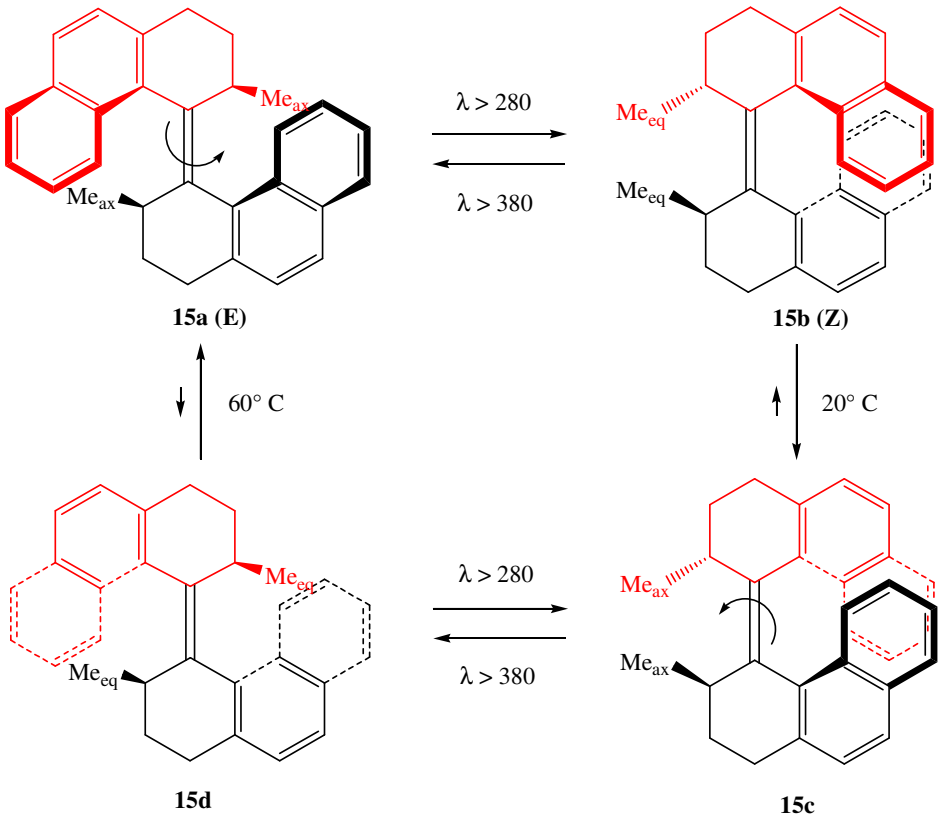

Figure I.20: Unidirectional molecular **15** motor driven by light and heat.

Upon photoirradiation at a wavelength longer that 380 nm, **15c** undergoes a conformational change into a highly strained *trans*-isomer **15d**. At 60°C, the molecule flips back to its original form and ends the rotation cycle. The unidirectionality of this motor is made possible thanks to the chiral properties of the molecule. Improved forms of this molecular motor have later been described in literature [56-58].

2.3. Supramolecular switches based on rotaxanes and catenanes

Rotaxanes are molecular systems in which a string is threaded through one or more rings. Bulky substituents at both ends are used as stoppers and avoid an unthreading of the

molecular necklace [59]. Molecular machines composed of two interlocked rings, varying in size, are called catenanes [59]. Typical schemes of such systems are presented in figure I.21.

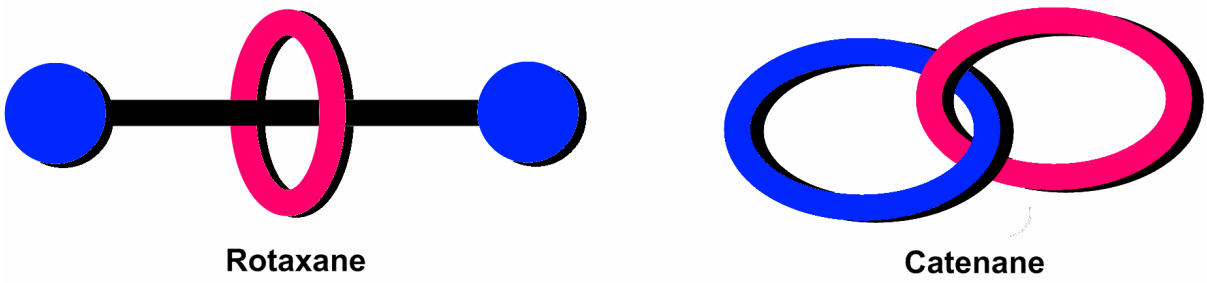

Figure I.21: Schematic representation of rotaxanes and catenanes.

2.3.1. Photoinduced intramolecular electron transfer in porphyrinic rotaxanes

Photoinduced electron transfer plays an important role in the primary events occurring in bacterial photosyntheic reaction center complexes, and is a well known phenomenon. For instance, association of cofactors SP and BPH form photosensitive protein complexes in the reaction center [61-66] of bacterium. SP is a bacteriochlorophyll dimer called “special pair” and BPH a bacteriopheophytin of the bacteria *Rhodopseudomonas viridis*. In this natural system, light excitation of SP induces fast electron transfer to BPH within 3 ps.

In order to mimic this biological system structurally and functionally, Sauvage and coworkers have elaborated bis-porphyrin **16** displayed in figure I.22 [67,68]. This V shaped molecule is composed of zinc (II) and gold (III) mesotetraaryl porphyrins bridged by a 2, 9-diphenyl 1,10-phenanthroline (dpp) spacer.

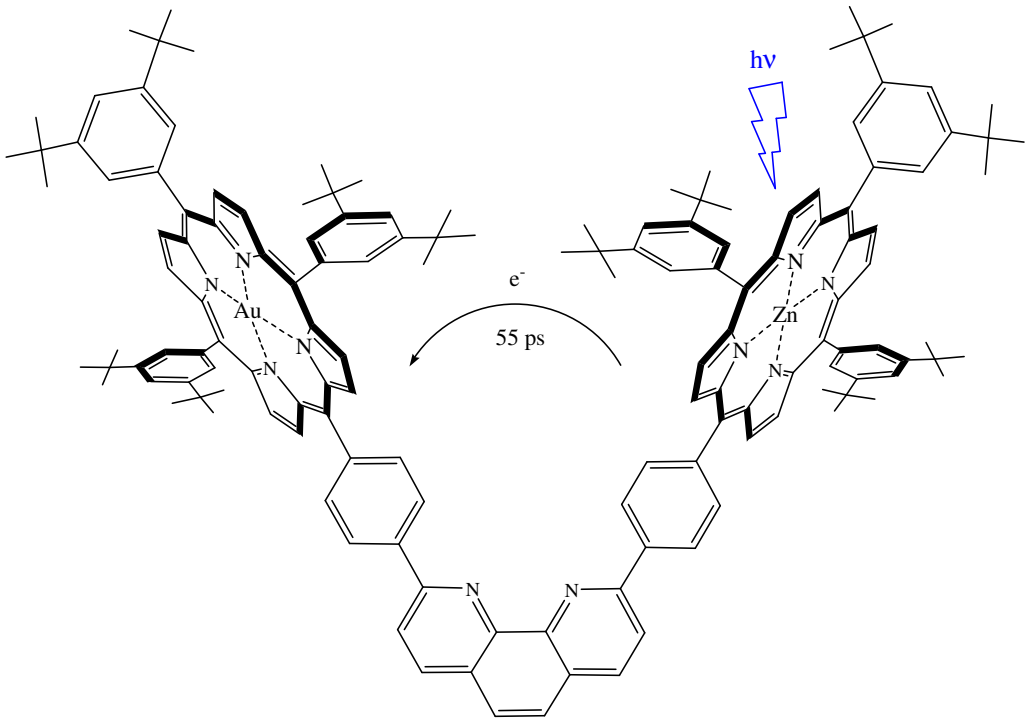

16

Figure I.22: Synthetic model **16** of the natural system Sp and BPh, mimicked by zinc (II) and gold (III) porphyrins respectively.

Zinc (II) porphyrin are powerful reductant (electron donor) in their excited state, whereas the gold (III) porphyrin are easily reduced (electron acceptor). Photoinduced electron transfer is detected and determined to occur within 55 ps [69].

Two ligands **16** intertwined around copper (I) ion connected by the diphenyl phenanthroline unit afford complex **17** [69] as sketched in figure I.23. Nuclear magnetic resonance (NMR) as well as crystallographic analysis show that the dpp core of one ligand is inside the cleft of the other. In this device, photoinduced electron transfer rate diminishes 16 times down to 3 ps which is equivalent to the speed of the biological Sp and BPh cofactor system.

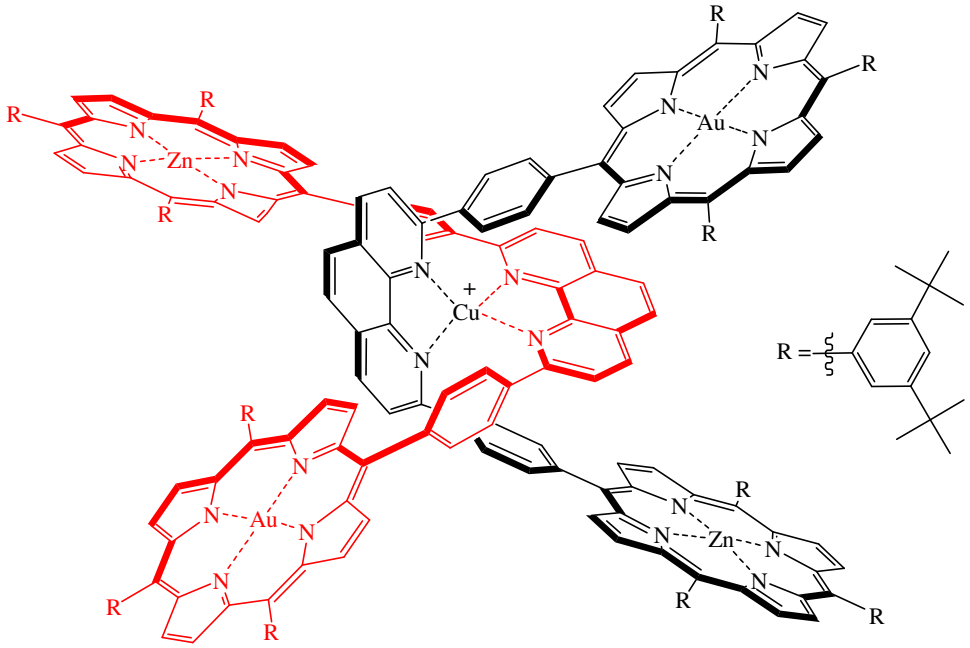

17

Figure I.23: Copper complex **17.**

To explain this decrease in electron transfer rate and to determine whether the electron travels inter or intra-ligandly a similar 4-coordinate copper (I) complex has been synthesized [70,71]. Complex **18** is formed of a dpp unit included in a crown ether ring connected to a V shaped ligand bearing acceptor and donor porphyrins. When complex **18** is demetallated (figure I.24), the phenanthroline of the loop is swung outside of the cleft and leads to free rotaxane **19**. A 1.7 ps photoinduced electron transfer rate has been measured for complex **18**, whereas free rotaxane **19** give a rate of 36 ps. These results suggest that the electron transfer occurs between the porphyrins of the same ligand. Contributing to this theory is the fact that the rate of the free rotaxane is similar to that of compound **16** mentioned above.

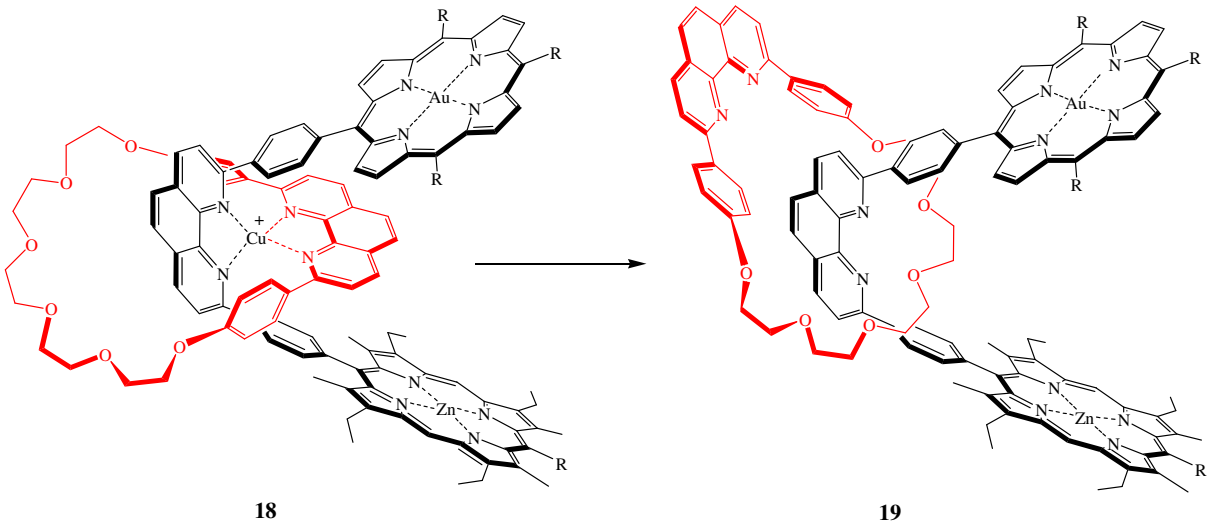

Figure I.24: Complex **18** and its rotaxane counterpart **19** after removal of copper (II).

2.3.2. Catenane switch

Following these findings, Sauvage and coworkers have synthesized a catenane where two different rings are interlocked [72,73]. One of the loops includes two coordinating units: a bidentate dpp and a tridentate terpyridine. On the other hand, the second loop has only one dpp complexation site. In the beginning, catenane **20a** is immobilized on a copper (I) metal ion and adopts a 4-coordinate tetrahedral geometry as described in figure I.25. Upon oxidation of the copper to the divalent state, **20a** turns into intense green **20b** species revealing a d-d absorption band at 670 nm in acetonitrile. This process can be triggered either by chemical (Br_2 or $NOBF_4$) or electrochemical oxidation. Rotational rearrangement of **20b** into pale olive-green **20c** is observed. This step includes decomplexation followed by rotation and recomplexation at the terpyridine (terpy) binding site. The 5-coordinate copper (II) shows an absorbtion band at 636 nm (ε = 125) which corresponds to 5-coordinated complex [Cu (II)(terpy)(bipy)$(ClO_4)_2$] described in literature (640 nm and ε = 120). It has been demonstrated that complex **20b** has a slightly distorted tetrahedral geometry whereas **20c** is

square pyramidal. After reduction of **20c** into **20d**, rotation of the terpy group leads to the starting catenane **20a**. This gliding of the ring takes place in a few seconds at room temperature regardless of the solvent. On the contrary, the speed of rearrangement after oxidation from **20b** to **20c** depends greatly on the solvent and the counteranion. This device can be regarded as a molecular motor as the loop effectuates a complete 360° rotary motion around the copper ions.

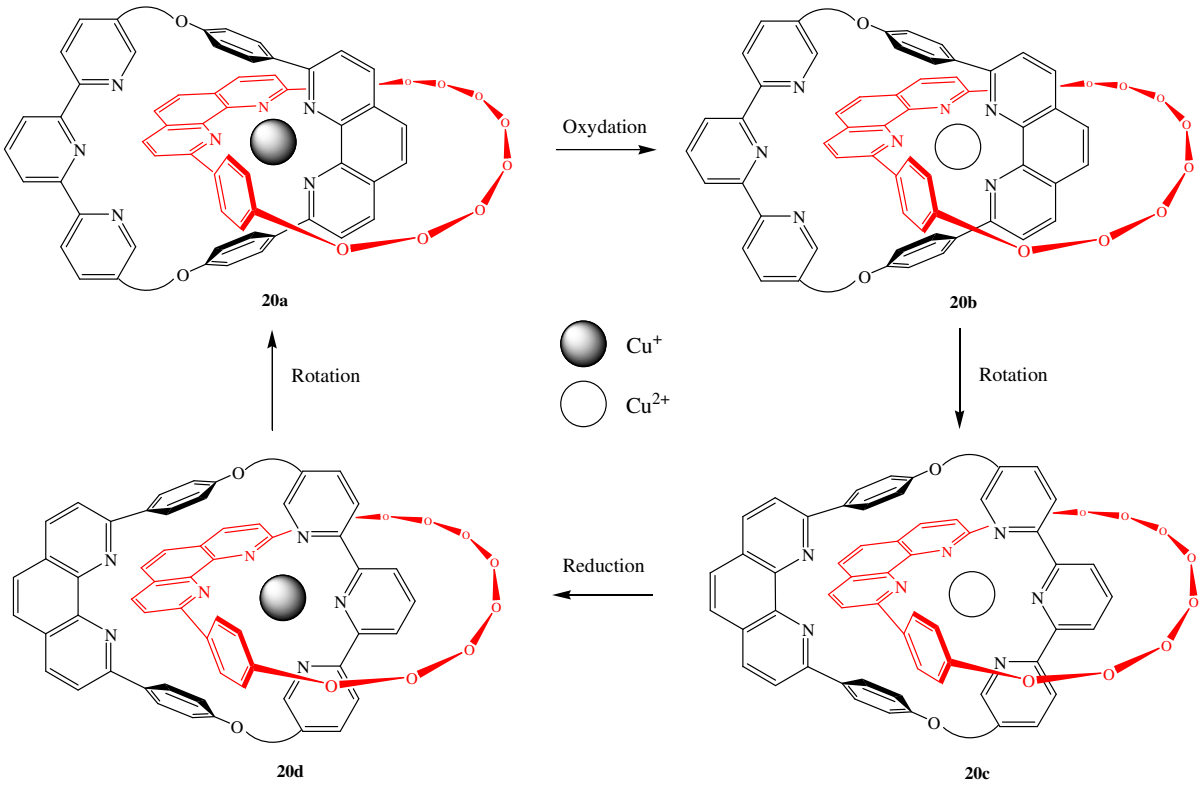

Figure I.25: Electrochemically driven rearrangements undergone by catenane **20**.

2.3.3. Artificial molecular muscles

Sauvage and coworkers have also built a molecular device that actually mimics the motion of sarcomers in the contraction of muscles described above in section 1.1.3.

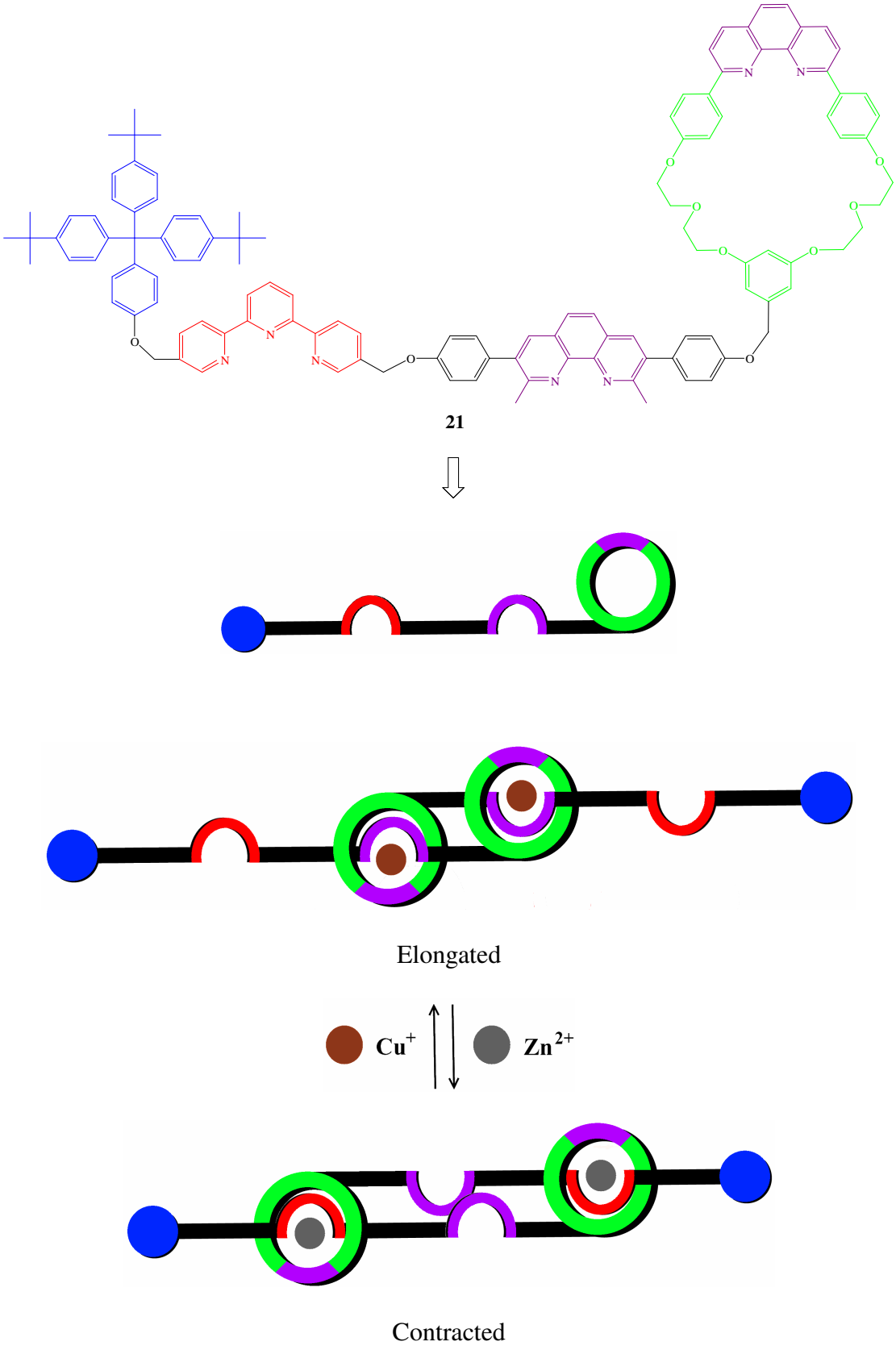

Figure I.26: Schematic representation of the elongated and contracted form of a synthetic molecular muscle.

This system, a pseudorotaxane, is a combination of two intercalated supracromolecules **21**, as presented in figure I.26, which elongates and contracts through replacement of metallic cations [74-77]. When two copper (I) ions are added, 4-coordinates complexes are obtained through the diphenylphenanthrolines moieties of both units. Decomplexation, followed by attachment of zinc (II) cations at the terpy sites, forms a 5-coordinate complex. This reversible process provokes piston-like motion switching from 83 Å in the elongated state to 65 Å in the contracted form.

2.4. Iron translocation in a polydentate tripodal ligand

In 1996, Lutz and Ward have synthesized a tripodal ligand **22**, sketched in figure I.27, bearing polydentate complexation sites [78,79]. The three branches of the tripodal ligand, linked together by a nitrogen atom, include hexadentate salicylamide and bipyridine moieties in their scaffold. Because iron (II) preferably binds to soft donors such as nitrogens, it first coordinates to bypiridine to form an octahedral complex. Upon oxidation to iron (III), the affinity towards bipyridine is lowered and the cation liberated. Thus the ferric ion, which preferentially coordinates to hard donors like oxygen, is translocated to the salicylamide complexation site. The process is reversible, as the initial state is recovered upon reduction to the ferrous iron (II) cation [80].

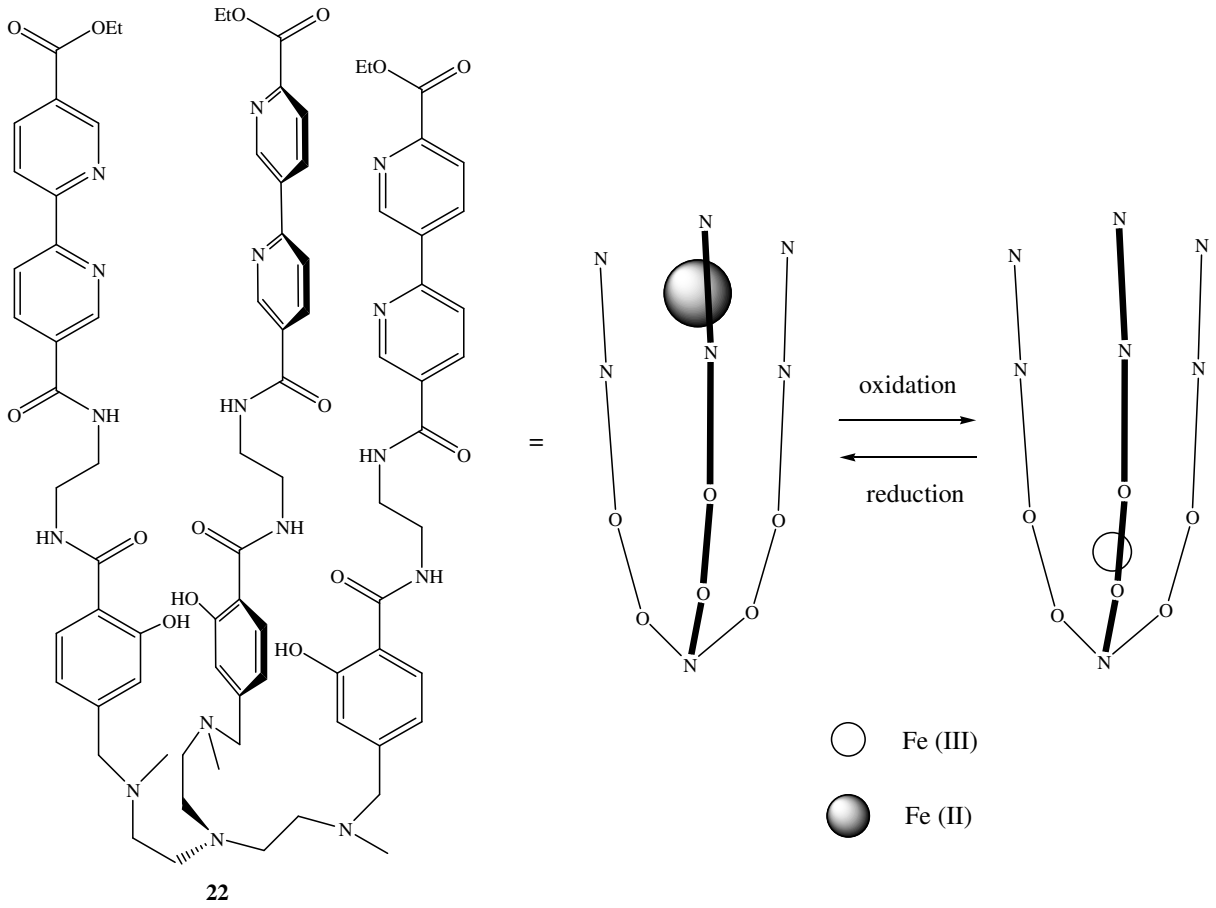

Figure I.27: Reversible iron translocation in tripodal polydentate ligand **22**.

2.5. Molecular electronics

Recently, De Silva and McClenaghan have reported a wide variety of molecular systems that act as logic gates [81]. An appropriate design and the clever choice of outputs and inputs allow the molecular diodes to translate chemical or physical phenomenon into binary codes.

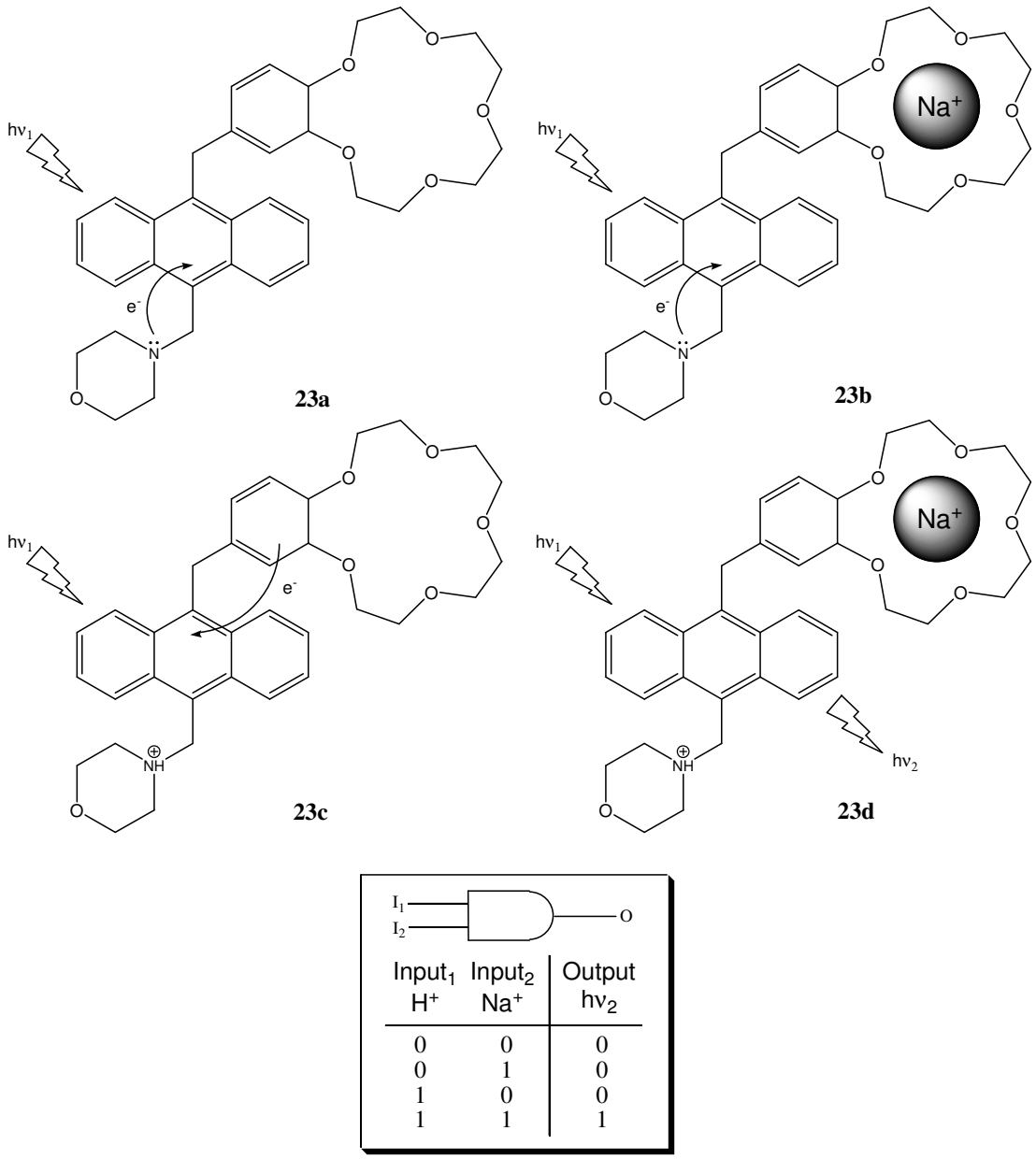

Input$_1$ H^+	Input$_2$ Na^+	Output $h\nu_2$
0	0	0
0	1	0
1	0	0
1	1	1

Figure I.28: AND molecular logic gate.

In this example, described in figure I.28, the fluorophore anthracene is separated from the two oxidizable receptors through inert methylene spacers and is constantly excited with light [82]. Input 1 is determined by the absence 0 or presence 1 of protons. Similarly, input 2 is governed by the absence or presence of Na^+ cation. The output is determined by the absence or presence of fluorescence. In the initial state, with no inputs, photoinduced electron transfer (PET)

occurs in **23a** through the non-protonated tertiary amine and quenches the fluorescence. The ouput gives therefore 0. When the crown ether complexes a sodium cation **23b** (input 2 = 1) and in the absence of H^+, similar fluorescence quenching occurs, as in the initial state, and the output is still 0. For **23c** the presence of H^+ (input 1 = 1) protonates the amine but PET is still occurring through the phenyl ring adjacent to the crown ether and the output remains 0. Finally, when both inputs are 1 like in **23d**, no quenching occurs and the presence of fluorescence indicates an output equal to 1. This particular type of logic gate is defined as an AND gate.

2.6. Molecular scissors

In 2003 Takahiro Muraoka, Kazushi Kinbara and Takuzo Aida have designed a new type of molecular machinery that resembles and imitates the movements of scissors [83]. Such molecular "scissors" **24** include, like their macroscopic counterpart, a pivot surrounded by handles and blades as illustrated in figure I.29. A ferrocene unit is chosen to play the role of the pivot as the cyclopentadienyl rings can rotate freely around the central iron (II) core. The two handles, linked together by a photoisomerizable azobenzene moiety, form a strap while the blades are made of phenyl rings bonded to the Cp rings. Open-close motion of the blades is induced upon successive UV and visible light irradiations of the azobenzene function which undergoes *cis*/*trans* isomerization.

a

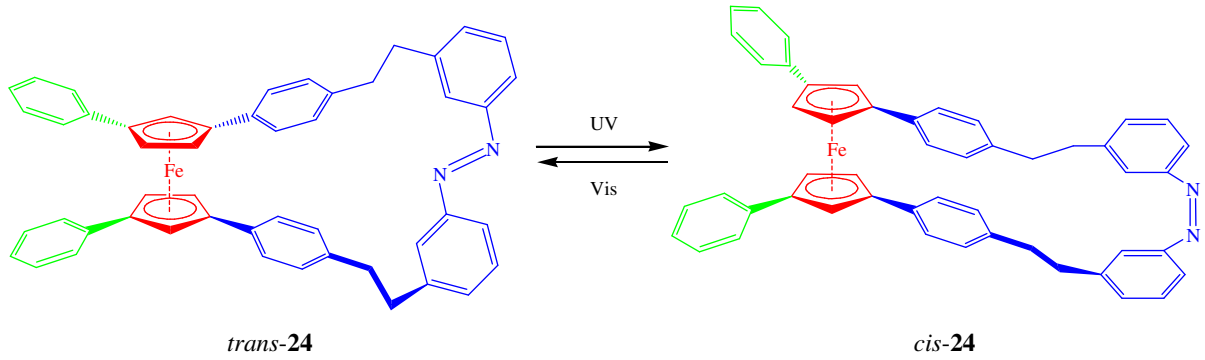

trans-**24** *cis*-**24**

b

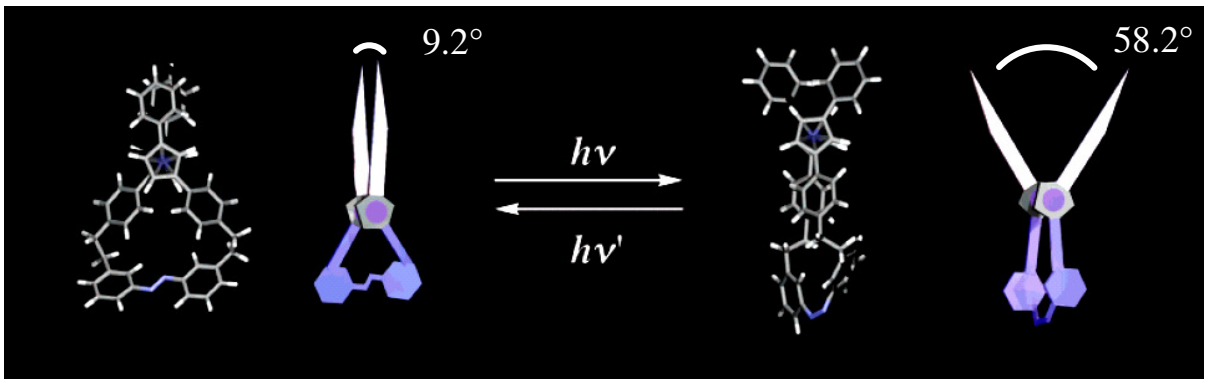

Figure I.29: **a** Aida and coworker's light driven molecular scissors. Green, blades; red, ferrocene pivot; blue handles. **b** schematic representation of the isomers of **24** optimized by DFT calculation and behavior upon illuminations [83].

Thus, a twisting motion is transmitted from the azobenzene strap through the cyclopentadiene rings on to the blades which forced apart from one another. In *trans*-**24**, the phenyl rings of the blades are almost parallel with a bite angle of 9.2° whereas after UV irradiation, the blades of *cis*-**24** move away from each other with a bite angle of 58.2°.

The 1,1',3,3'-tetrasubstituded ferrocene introduces planar chirality into **24**, which allows circular dichroism (CD) spectroscopy studies of the ferrocene's angular motion upon

irradiation. UV-Visible (VIS) spectroscopy and ^{1}H NMR spectroscopy were also conducted to support the motion of the blades of the scissors. For instance, the NMR peaks due to the aromatic protons on the azobenzene shifted upfield upon *trans* to *cis* isomerization, in accordance with the upfield shifts exhibited by numerous azobenzene derivatives [83]. In the same manner, the NMR aromatic protons signals of the blades are shifted upon photoisomerization. These differences in chemical shifts are due to the proximity of the blades in the *trans*-**24** isomer; this allows the aromatic protons of both blades to interact with each other. On the contrary, in *cis*-**24**, separation of the blades lowers the magnetic shielding effect of the aromatic protons and leads to a downshift of the proton signals [83].

As presented in figure I.30, the crystallographic analysis shows the actual three dimensional structure of a crystal of *trans*-**24**.

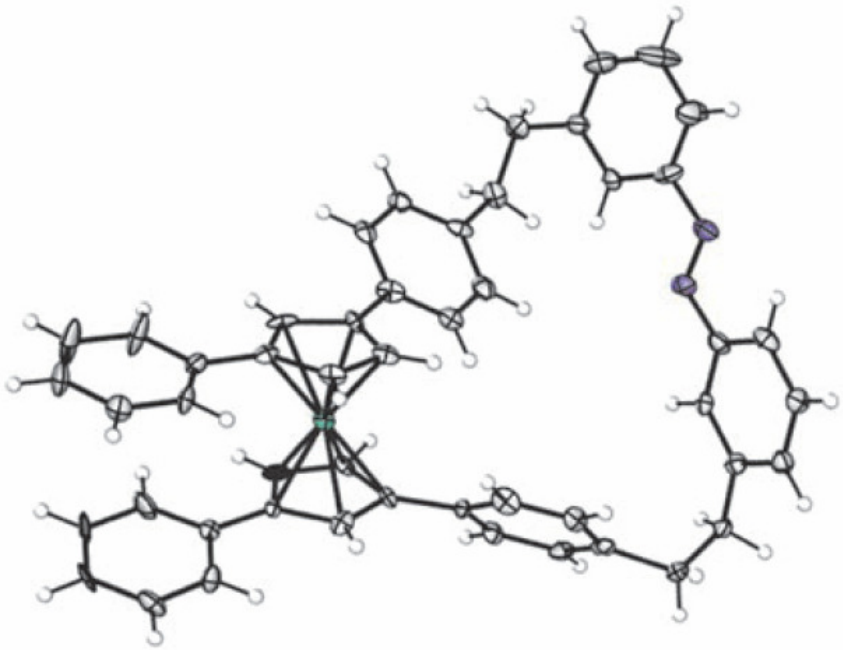

Figure I.30: Cristallographic structure of *trans*-**24**. Image provided by Takahiro Muraoka at the University of Tokyo [86].

2.7. Molecular pedal

Pursuing in this direction, Aida and coworkers have achieved a molecular device which mechanically manipulates another molecule in a controlled and reversible manner, a feat that had never been realized before [84]. The concept of this molecular system is presented in figure I.31. They have demonstrated that light induced scissors-like conformational changes of a host molecule can be transmitted to a non-covalently bound guest molecule.

In order to functionalize the phenyl blades of the previously described scissors, Aida and coworkers have introduced a zinc porphyrin function to create molecular pedals. This host molecule *trans*-**25** accommodates bidentate rotor guest **26**, 4,4'-biisoquinoline, by coordination of the imines bases with the zinc porphyrin to form a stable **26** ⊂ *trans*-**25** host-guest complex. Upon light exposure, the angular motion of the zinc porphyrin units (provoked by isomerization) separates the two porphyrin units in clockwise and anticlockwise directions and induces repeated twisting of the guest.

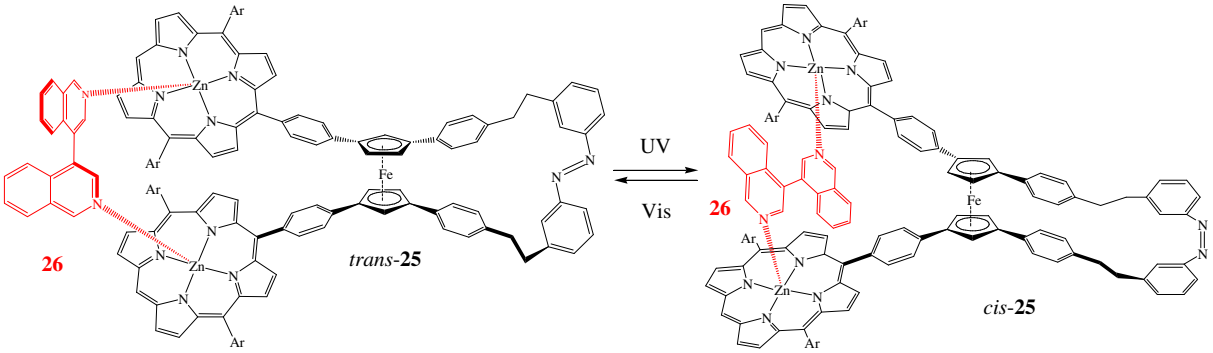

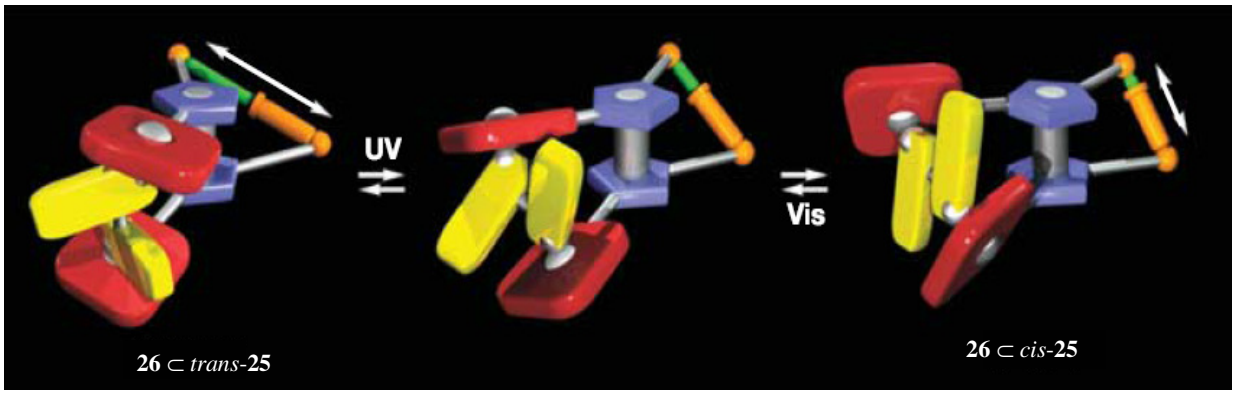

Figure I.31: Schematic representation of a molecular pedal that manipulates a guest molecule upon light illumination [84].

Furthermore, the (+) and (-)-enantiomers of *trans*-**25** selectively bind the (*R*) and (*S*) enantiomers of **26**. These results were confirmed by several CD, UV and NMR analysis [84]. Further ferrocene based devices were built and studied by Muraoka and coworkers [85-87].

3. Spin crossover

Cristal field theory explains that the five degenerate d orbitals of transition metals are driven apart when a ligand approaches the metal ion according to the geometry of the complex. Indeed, as electrons repel each other, the non binding electrons from the ligands will be in closer proximity of some d orbitals and further away from others creating a loss of degeneracy. Such splitting of the d orbitals for an octahedral complex is depicted in figure I. 32

Spin-crossover is a phenomenon in which certain compounds of transition metals demonstrate a reversible transition from low spin (LS) state to high spin (HS) state, or vice versa. This phenomenon being only possible when the two spin states are in close energy proximity. For instance, in iron (II) octahedral complexes, the transition occurs via an electron promotion

from t_{2g} non-bonding M-L orbitals to e_g M-L antibonding orbitals. This concept has first been discovered in 1931 by Cambi and coworkers [88] and can be triggered by means of variations in temperature, pressure and by light irradiation which lead to both an electronic (change in the d-electron orbital configuration) and structural changes. This often results in a colour and magnetic moment changes. Only octahedral 6-coordinate complexes with an outer electronic configuration of d^4 to d^7 can demonstrate spin-crossover transition. Figure I.32 shows a spin-crossover for iron (II) that has an electronic configuration of $3d^6$. The electrons can either occupy all the lower energy orbitals (LS with a high orbital splitting energy) or both set of orbitals (HS with a low orbital splitting energy). The spin state on the iron (II) ion switches from diamagnetic (S=0) in the LS state to S=2 paramagnetic HS state with four unpaired electrons. This spin transition results in colour changes from purple in the LS state to yellow in the HS state.

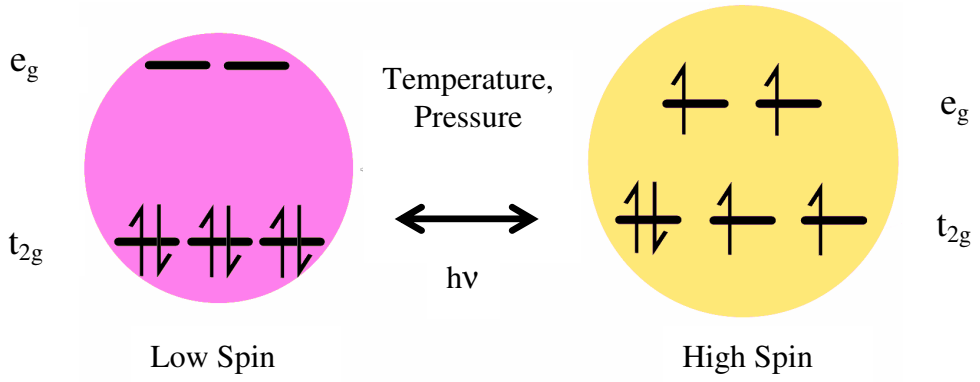

Figure I.32: General example of a spin-crossover from LS to HS in a $3d^6$ system.

Such compounds possess remarkable physical properties that could potentially lead to industrial applications in the field of information storage, display devices or temperature sensors. A first step in this direction has been achieved by Kahn and coworkers in 1998 that have opened the gates of information storage at the molecular level [89] and inspired our

project. As some iron (II) complexes exhibit thermal hysteresis during the LS→HS conversion, Kahn and coworkers have synthesized polymer chains in which iron (II) cations are linked by substituted triazole ligands. For these thermochromic polymers, room temperature falls in the center of the hysteresis loop produced by spin transitions, a particularity that could be of great use for the applications mentioned above [89].

Another study by Soyer and coworkers achieved to carry out spin-crossover in d_4 to d_7 transition metal complexes by ligand-driven light-driven spin changes [90]. In their concept, alteration of the ligands by means of light irradiation provokes a variation of the ligand field which is sufficient, in some cases, to change the ground state.

3.1. Light-induced excited spin state trapping (LIESST)

In 1984, Descurtins, Hauser and Güthlich have discovered a spin transition in iron (II) complexes induced by light that they called "light-induced excited spin state trapping" (LIESST) [91]. When irradiated with green light (~540 nm) at low temperature, the compounds undergo a quantitative transition from the thermodynamically stable LS state to the metastable HS state. The system then remains trapped in HS state at low temperature with a quasi infinite lifetime and reverts to its initial LS stable state thermally. It has also been discovered that irradiation with red light at 840 nm provokes the same relaxation to the LS state [92].

Before the work of Hayami and Sato, it was thought that iron (III) HS states are transient and rapidly revert to their original LS state through tunnelling effects. They have found out that such a rapid relaxation can be prevented by strong intermolecular interactions in molecular

compounds. It is thought that the cooperativity resulting from the intermolecular interaction works to increase the activation energy for the relaxation processes, enabling the observation of a “long-life” metastable state after irradiation [93].

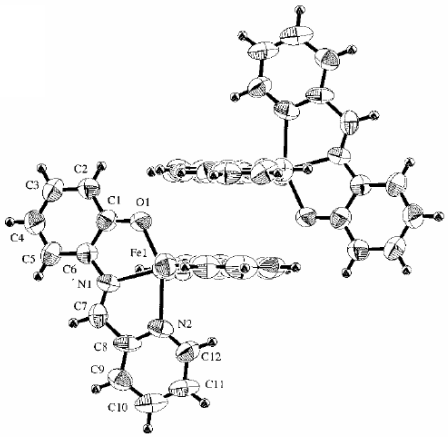

27

Figure I.33: Cristallographic structure of ligand **27** showing inter-ligand π-π interactions.

In this perspective, Sato and coworkers have synthesized $[Fe(pap)_2]ClO_4 \cdot H_2O$ **28** which planar phenylazopyridine (pap) ligands **27** can take part in π-π interactions with its surrounding homologues (figure I.33). At room temperature, this complex **28** exhibits a magnetic properties value $\chi_m T$ = 3.9 cm^3 K mol^{-1} that corresponds to what is expected for the high spin state in iron (III) compounds. When cooled down, the $\chi_m T$ value of the complex drops suddenly around a temperature T = 175° K like displayed in figure I.34.

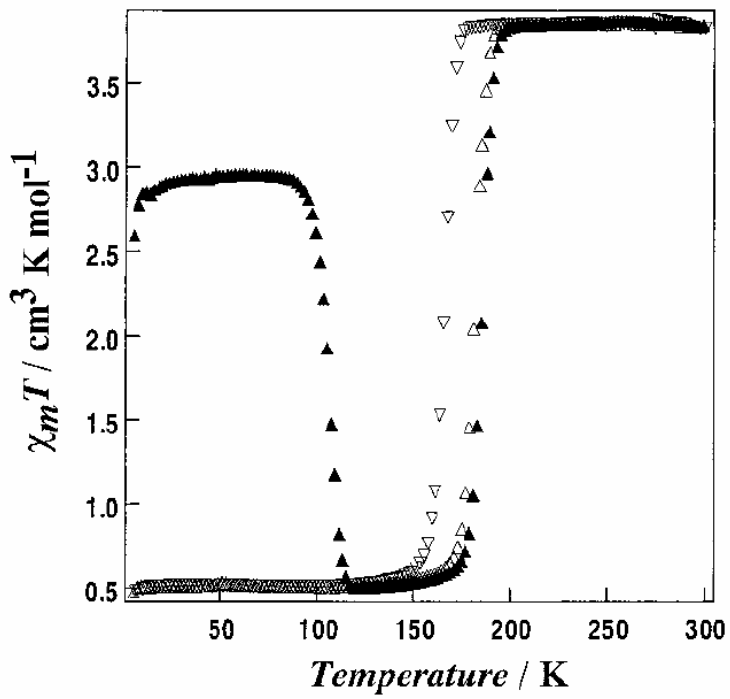

Figure I.34: $\chi_m T$ versus T plots for complex **28**. Sample was cooled down from 300° to 5° K (∇) and then warmed from 5 to 300 K (Δ) at a rate of 2° K min^{-1}. Sample was warmed at a rate of 2° K min^{-1} after it was irradiated at 5° K (▲) [93].

The $\chi_m T$ value at 100° K is equal to 0.51 cm^3 K mol^{-1}, in accord with a low spin state and confirms the spin transition. Illumination with a section of visible light ranging from 400 to 600 nm is directly carried out in the SQUID magnetometer at 5° K. An increase of magnetic susceptibility of **28** is observed and clearly shows that LS to HS transition is induced by light irradiation. Further Mössbauer analysis at 13° K displays that complex **28** exhibits the same behaviour upon irradiation and switches back to LS state upon thermal treatment at 130° K [93].

Such behaviour upon light exposure could find applications in a near future. Nevertheless, up to now none have been possible because the lifetimes of the photomagnetic states are often only stable at low temperatures.

4. Purpose of this thesis

In a number of transition metal complexes like nickel (II), the energy between HS and LS is almost similar. A small perturbation is therefore sufficient to perform spin transition. Our goal in the area of artificial molecular machines is to build a molecular device bearing a nickel (II) metal ion that could switch its magnetic susceptibility upon repeated light irradiations.

4.1. Diphosphine dihalide nickel (II) complexes as potential photomagnetic switches

In 1962, Browning and Venanzi studied various $[(R_3P)_2Ni(II)X_2]$ (X=halide) type complexes in order to determine if the change of phosphine is responsible for the differences in magnetic susceptibilities. They concluded that the formations of diamagnetic species are more dependent on the π-acceptor than on the σ-donor capacity of the phosphorus atom. Triarylphosphines ligands are therefore more susceptible to generate paramagnetic complexes with nickel (II) whereas trialkylphosphines ligands tend to afford diamagnetic complexes [94]. They also proposed another model for the formation of paramagnetic and diamagnetic species in solution which suggests that the changes in magnetic susceptibility are due to changes in the P-Ni-X bond angles.

4.2. Brief presentation of our system

In the present work, we set out to exploit the latter hypothesis of Venanzi to create a molecular switch relying on the change in magnetic properties of nickel (II) ions. Our molecular switch **29**, composed of a tetrasubstituted ferrocene, bears phosphine blades in order to coordinate a nickel (II) cation as sketched in figure I.35. Photoisomerization of the azobenzene group provokes a rotation of the pivot which induces a separation of the blades bearing the phosphines. This physical constraint on the metal could provoke a change in geometry and thus the magnetization of the nickel (II) complex. Our aim is to synthesize a nickel (II) complex coordinated to a phosphinated "scissor like" ligand.

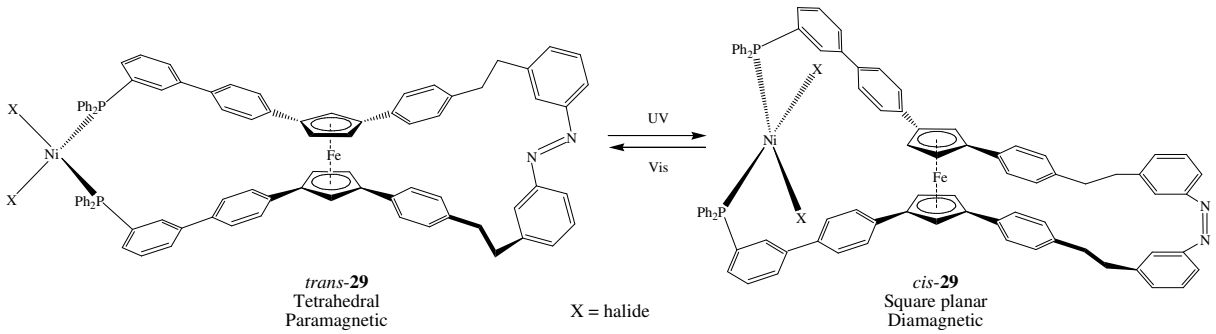

Figure I.35: Representation of our molecular switch **29** that opens and closes through UV and visible light irradiations.

- Chapter II -

Results and discussion

1. Structural correlation

As suggested by Venanzi and coworkers variation of the phosphine cone angle [94] may have an impact on the geometry and thus the magnetic properties of $[NiCl_2(PR_3)_2]$ complexes. Transferring this observation to *cis*-diphosphine complexes, we analyzed whether the (P-Ni-P) bite angle could be correlated to the geometry around the nickel. For this purpose, a structure correlation was performed on all $[NiCl_2(PR_3)_2]$ complexes reported in the Cambridge Structural Database (CSD, august 2008). The bite angle of each complex was plotted as a function of the dihedral angle between the plane of the chlorides and the plane of the phosphines (figure II.1). We found out that at a certain phosphine bite angle (around 101°) a limit was reached where the square planar complexes were forced to adopt tetrahedral geometry. So the geometry of the complex was dependant on the phosphine bite angle as depicted in figure II.1. The general trend showed that small bite angles favour square planar geometry whereas bigger bite angles afford tetrahedral complexes.

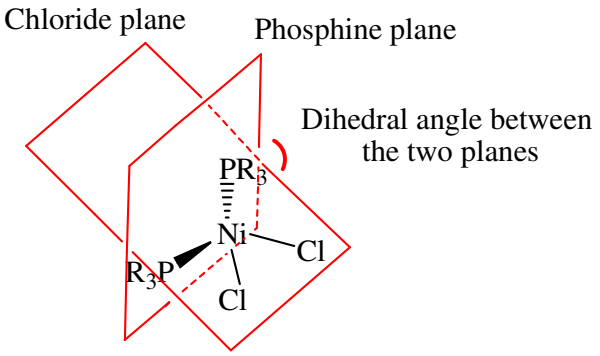

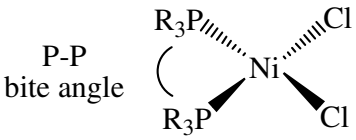

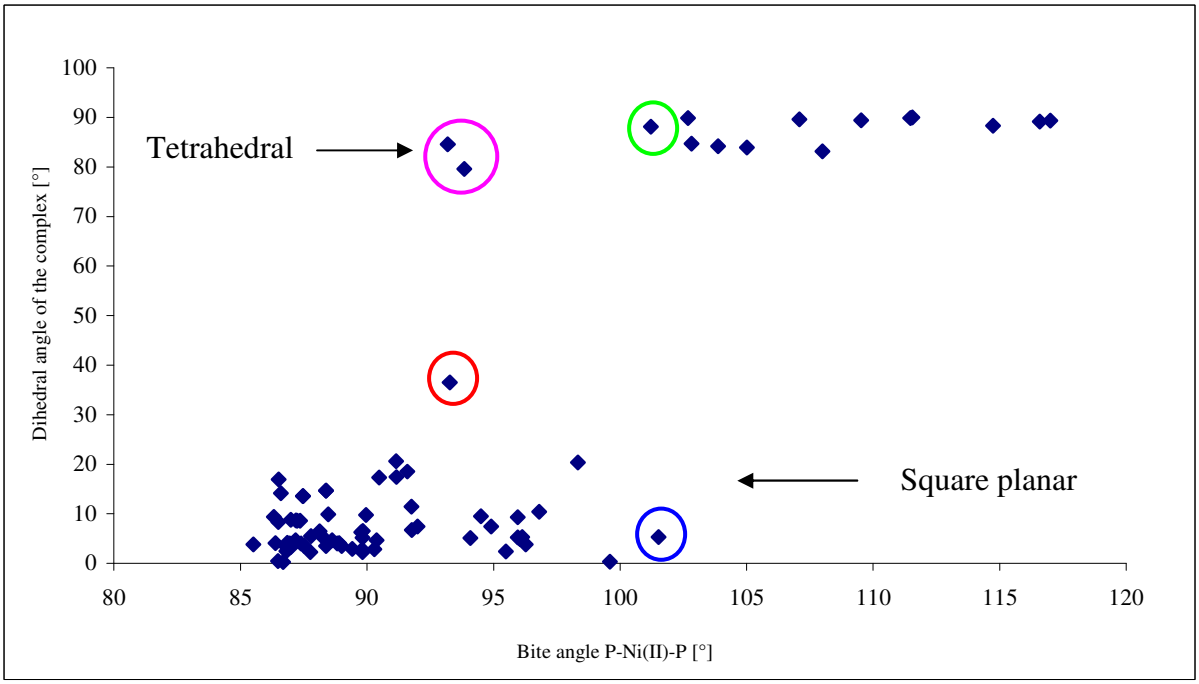

Figure II.1: Plot of the dihedral angle as a function of the bite angle of the diphosphine in $[R_3P^{\frown}PR_3NiCl_2]$ deposited in the Cambridge Structural Database (August 2008).

Exceptions deviating from this trend were found for a nickel (II) BINAP complex **30** (figure II.2), circled in red on the graphic [95]. Despite a small bite angle (93.27°) this complex exhibited an unusual dihedral angle of 36.5°. We speculated that the rigidity of the bidentate ligand forced the complex to adopt such geometry, poised between tetrahedral (90°) and square planar (0°). Circled in pink, a nickel (II) diferrocene diphosphine complex **31** [96]

diverged even more from the trend (figure II.3) and adopted a tetrahedral geometry despite the small phosphine bite angle (93°).

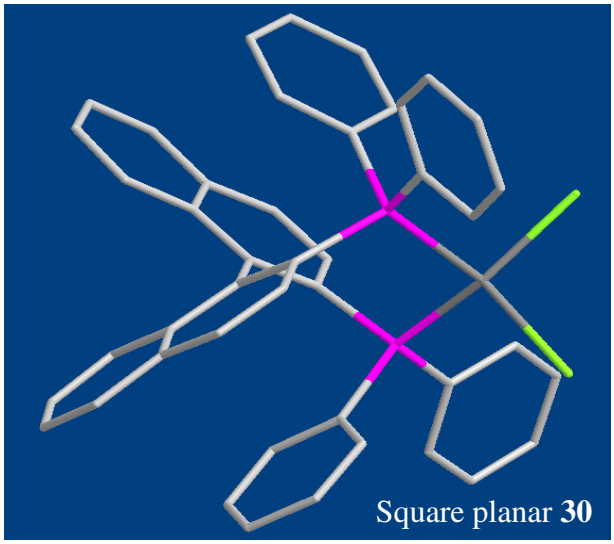

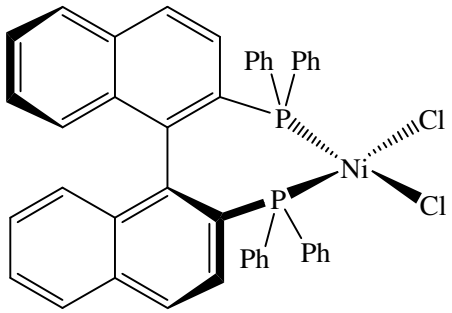

Figure II.2: Cristallographic structure of [$NiCl_2$(BINAP)] **30**, an example deviating from the trend; pink, phosphorus; green, chloride, dark grey, nickel [95].

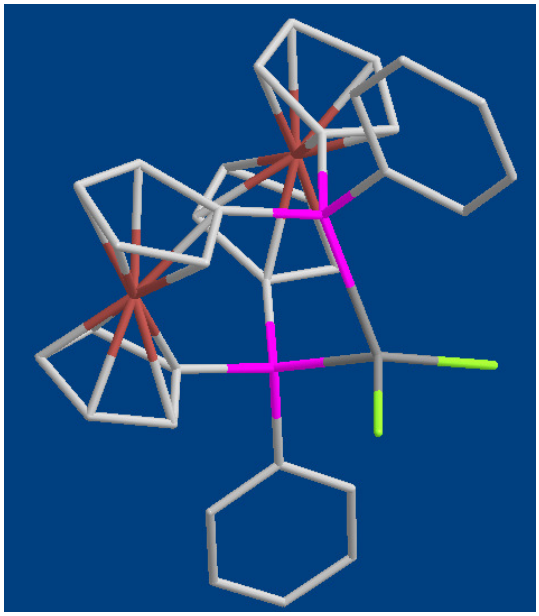

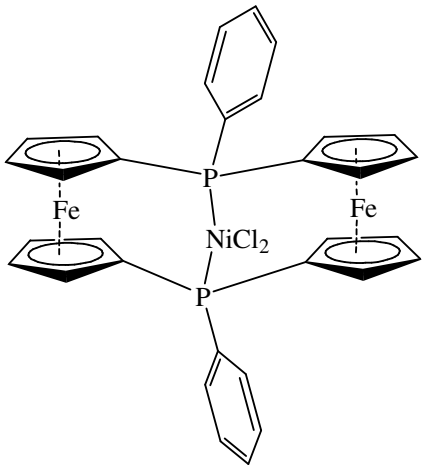

Figure II.3: Cristallographic structure of diferrocene diphosphine **31** [96] exhibiting a divergence from the general trend; pink, phosphorus; green, chloride, dark grey, nickel; red, iron.

Again, we suggest that the highly constrained geometry of the ligand is responsible for this unusual geometry of the nickel (II) complex. Two different crystal structures were deposited for complex **31** in CSD which are represented by two points circled in pink in figure II.1. Circled in blue and green respectively on figure II.1, tetrahedral complex **32** [97] and square planar complex **33** [98] (figure II.4) are poised at the limit of the gap between square planar and tetrahedral geometry. They are of particular interest because they adopt different geometries despite very similar phosphine bite angles (around 102°).

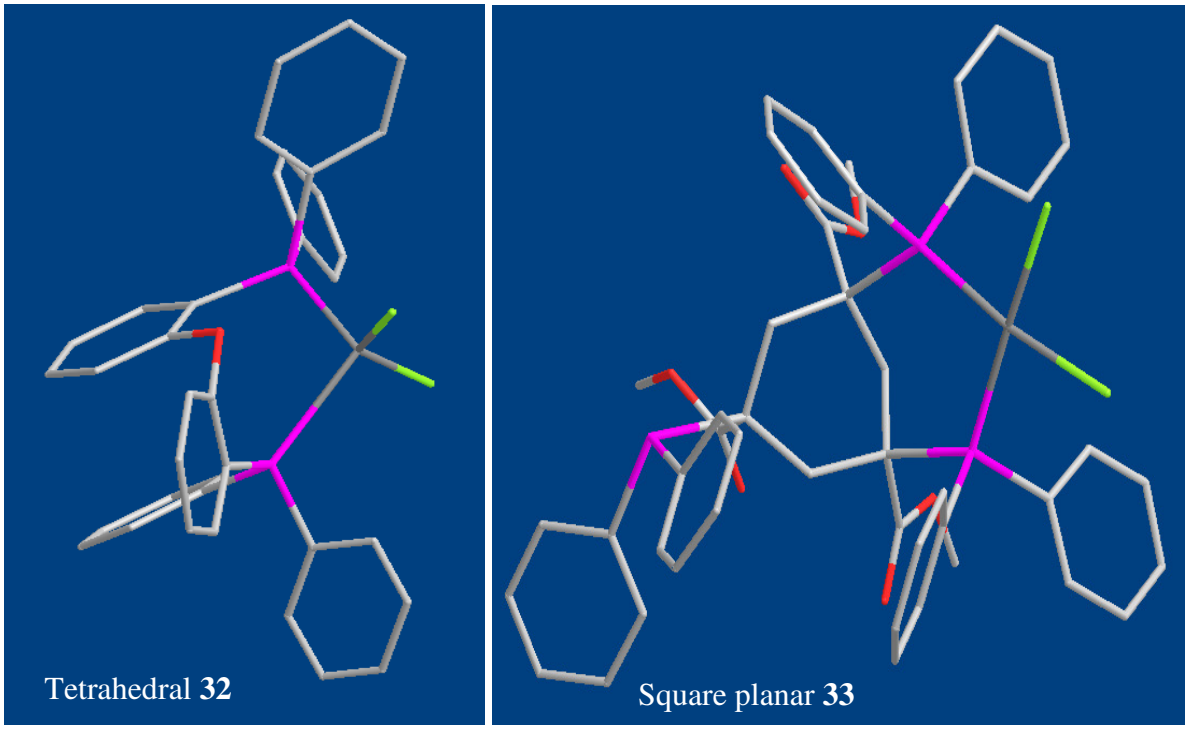

Figure II.4: Cristallographic structures of tetrahedral complex **32** [97] and square planar complex **33** [98] with phosphine bite angles of 101.22° and 101.51° respectively poised at the limit between tetrahedral and square planar geometries.

We found out that the arylphosphines always favour tetrahedral complexes, a suggestion that had already been made by Goursot and coworkers [99].

1.1. Nickel based photomagnetic switch

This project was based on the work of Aida and coworkers on light driven molecular scissors [83] described in section 2.6 of chapter I. We learned from the structural correlation that a small variation of the phosphine bite angle is sufficient to switch the geometry of a $[NiCl_2(PR_3)_2]$ complex. This variation of phosphine bite angle could therefore be accomplished by rotational separation of scissor blades. Thus, in order to build photomagnetic switch **29** presented in section 4 of the introduction, insertion of metal-coordinating phosphine moieties in the blades of Aida's molecular scissors **24** was envisaged. Tetracoordinated d^8 nickel (II) complexes are bistable and can exist in two configurations either as square planar diamagnetic or tetrahedral paramagnetic. The difference of magnetism is due to the two unpaired electrons found in a tetrahedral d^8 ML_4 complex. We expected that the isomerization of the azobenzene handles, transmitted to the blades by mechanical twisting of the ferrocene pivot, could provoke a change in geometry and thus a variation of the magnetic susceptibility. For the first time, spin transition could be achieved by the action of mechanical energy. The ultimate goal of such a switch could be information storage on a single molecule where the writing-erase process (light exposure) would be independent from the reading process (magnetism). Various assets such as magnetic and temperature stability could ensue from this new device whereas information storage based on spin crossover are, in most cases, only switchable at low temperatures. In 1976, Hoffman and coworkers reported a study on ML_4 complexes that can adopt either square planar or tetrahedral geometry [100].

With the help of Hückel parametrization, they discovered that a d^8 ML_4 complex prefers the low spin square planar geometry whereas a d^{10} complex clearly favours tetrahedral geometry. A d^9 complex is in conflict between the two geometries because it has to choose between adding an electron in the high energy $2b_{1g}$ orbital for a square planar complex or pairing

another electron in t_2. Based on these studies, an energy diagram was established for d^8 ML_4 complexes as depicted in figure II.5. For example, the decrease in energy from $2b_{1g}$ to t_2 in a square planar to tetrahedral transition is due to the decrease of hybridization among the orbitals of the ligand and the metal. The electrons in the highest occupied molecular orbital (HOMO) $2a_{1g}$ of a d^8 square planar complex are paired, and therefore diamagnetic with a μ_{eff} = 0 BM (S = 0).

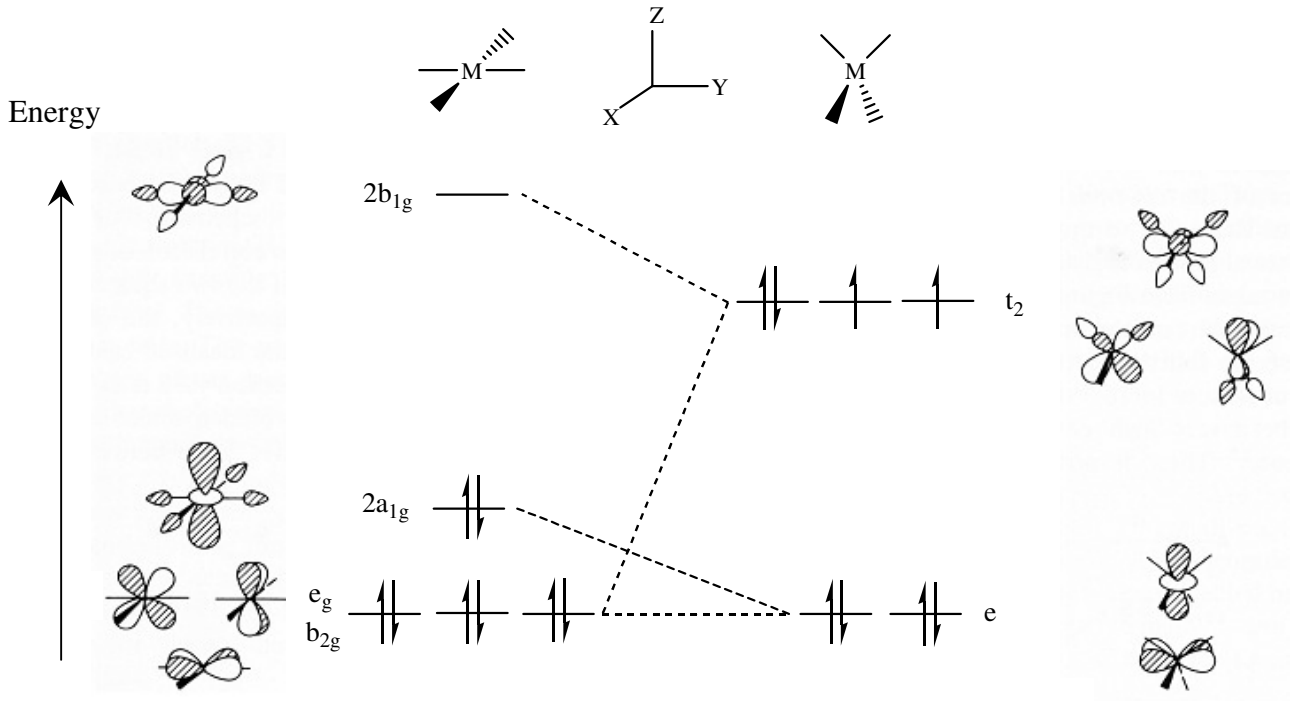

Figure II.5: Evolution of the frontier molecular orbitals during the distortion for a d^8 square planar ML_4 complex into a d^8 tetrahedral complex.

On the other hand electrons in the HOMO t_2 for the tetrahedral d^8 complex are unpaired according to Hund's rule and show paramagnetism with a $\mu_{eff} \approx 3$ BM (S = 1). Furthermore, this spin transition is almost thermoneutral [98].

2. First synthetic route

Our first strategy consisted in introducing the phosphine groups at the very beginning of the synthesis, using phosphine oxobutanoate **38** for the construction of the cyclopentadiene moiety. As displayed in figure II.6, this compound was similar to the starting material of the synthesis of the molecular scissors **24**, described in chapter I under section 2.5.

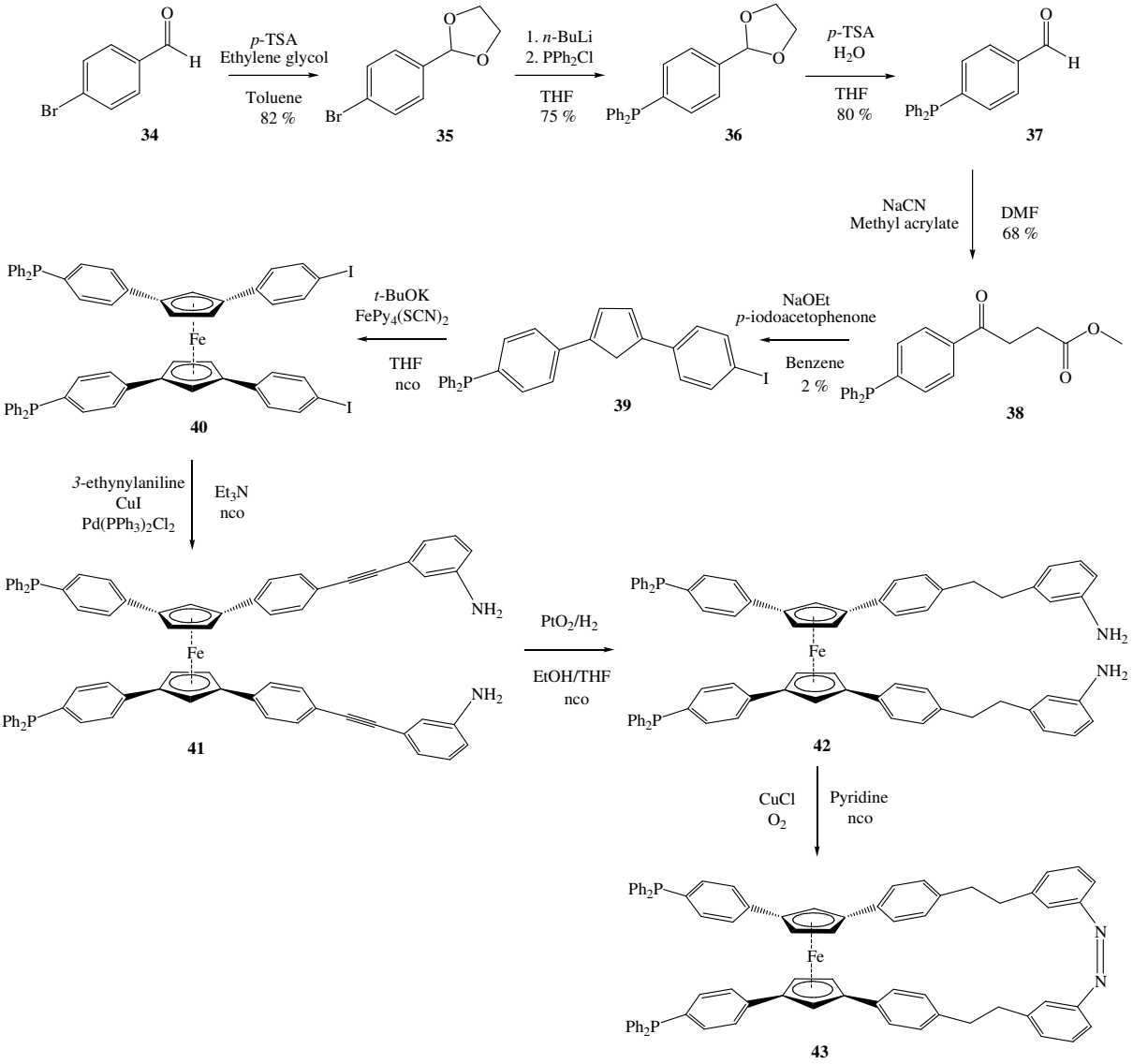

Figure II.6: Proposed synthesis of the photoresponsive ferrocenyl diphosphine ligand **43**; nco = not carried out.

Introduction of a diphenylphosphine unit on *p*-bromobenzaldehyde **34** after acetal protection gave *p*-diphenylphosphinebenzaldehyde **37** [101]. It was followed by addition of methylacrylate to aldehyde **37**, according to Stetter‘s “umpolung” reaction [102]. This reaction catalyzed by sodium cyanide, yields *p*-diphenylphosphine oxobutanoate **38**. Unfortunately, the formation of the cyclopentadiene **39** catalyzed by sodium ethoxyde [103] produced only very poor yields and was accompanied by oxidation of the phosphine. As the reaction leading to the cyclopentadiene dates back one century, we tested numerous different conditions and varied the bases. We later found that replacing the sodium ethoxyde base by potassium *tert*-butoxyde afforded higher yields. Still the yields were too low (2%) to pursue this route. We thus opted for the introduction of the phosphine moieties at a later step.

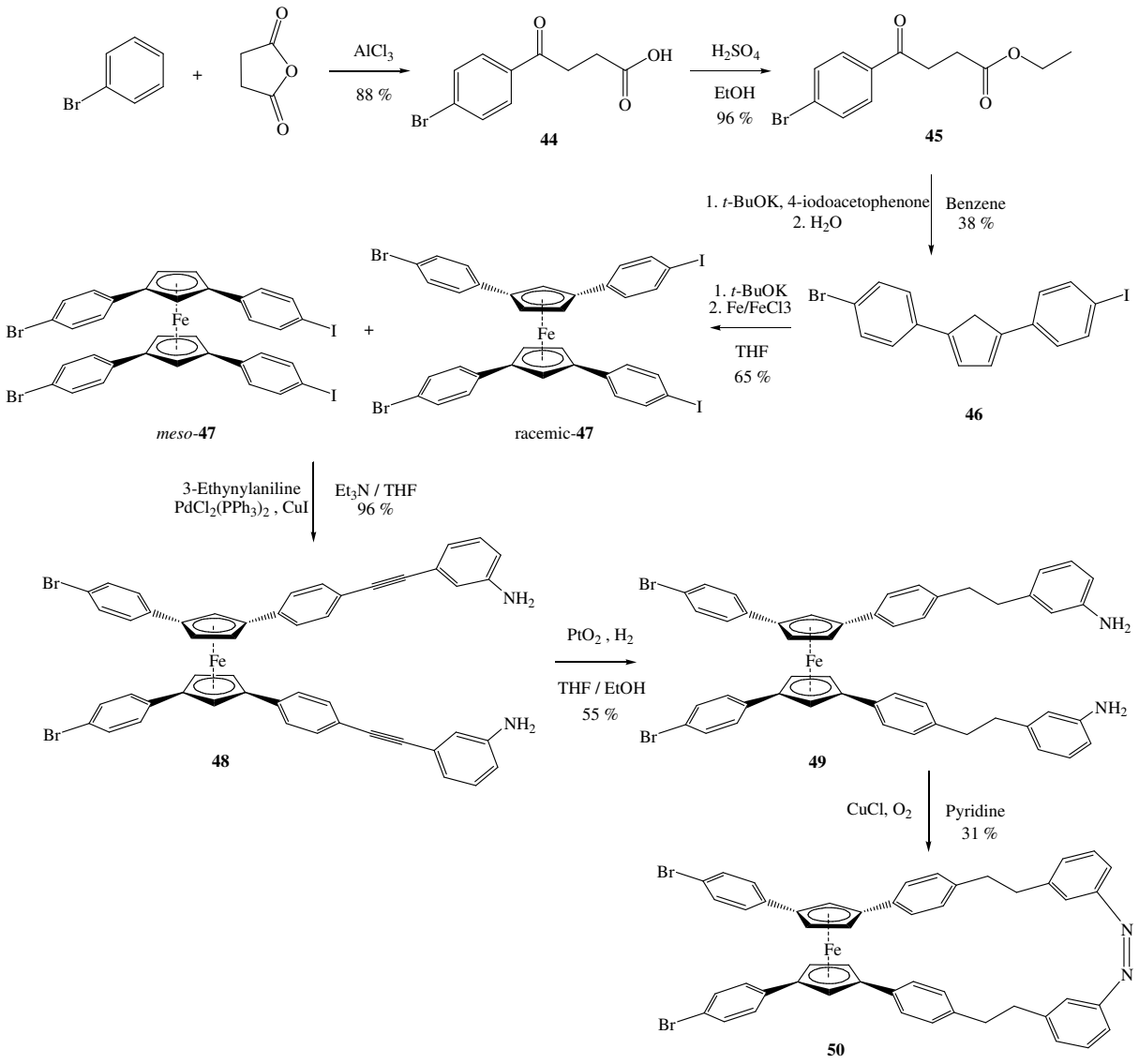

Figure II.7: Multi-step syntheses of bromo scissors **50**.

3. Phosphination and synthesis of bromo scissors 50

In another attempt, we set out to replace the bromine atoms in bromo scissors **50**, originally reported by Aida, by diphenylphosphine entities moieties. The synthesis of ferrocenyl bromo scissor **50** was published in 2006 by Aida and coworkers [84] and is sketched in figure II.7.

Different phosphination attempts were carried out on model compound **52** (figure II.8) because of the scarcity of **50**. Ferrocene **52** was synthesized following a similar protocol as presented in the latter figure II.7 replacing iodoacetophenone by acetophenone. These attempts were unfruitful. At best, we recovered mono phosphinated **54** in very small amounts (less than 1 % yields) after preparative gel permeation chromatography (GPC). These results corroborated with similar failed phosphination attempts towards **51**, carried out in Aida laboratory directly on the bromo scissors **50**. It encouraged us to change our synthetic strategy.

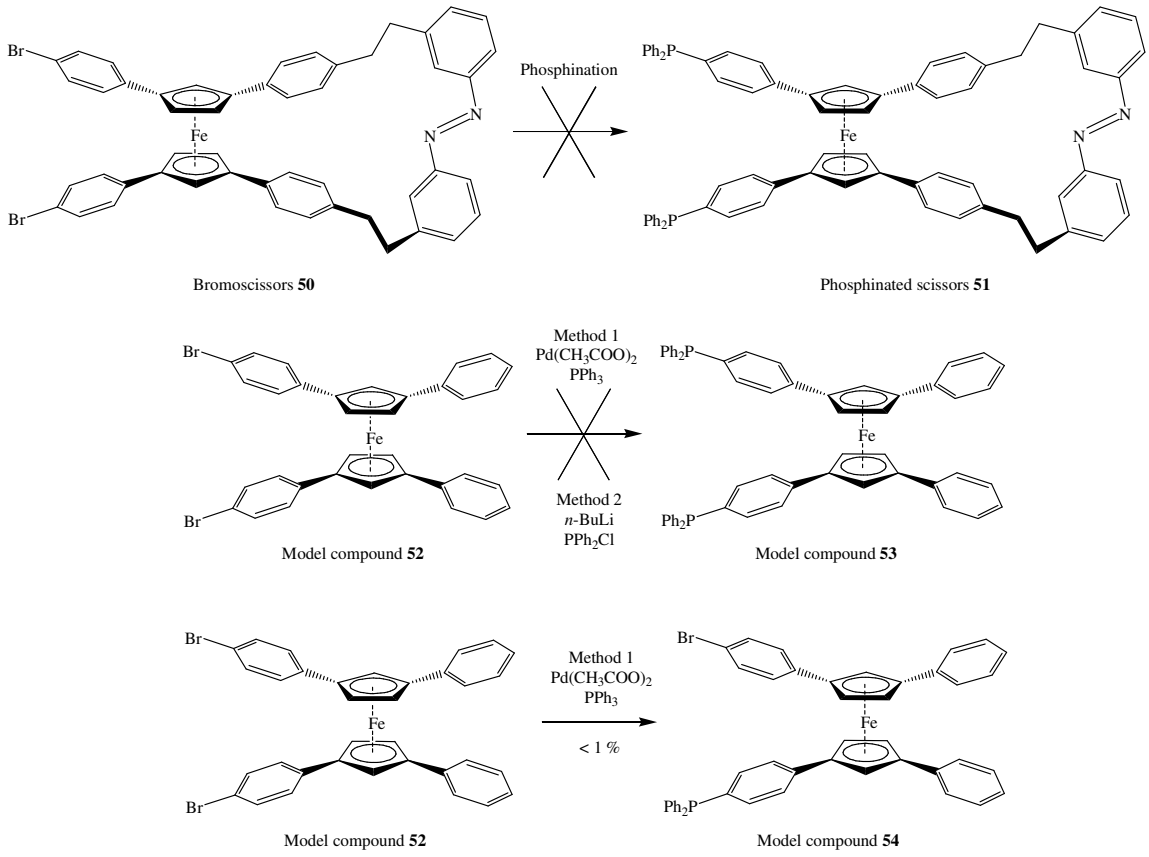

Figure II.8: Failed phosphination attempts on bromo scissors **50** and on model compound **52**.

4. Synthesis of the phosphine containing photoresponsive ligand

Having failed to insert a diphosphine moiety in the molecular scissors by the two approaches outlined above, we chose a route via bromo scissors **50** in collaboration with Prof. Aida (University of Tokyo). Indeed, Suzuki cross-coupling of **50** with boronate **54** produced the diphosphine oxide scissor ligand **55**, as presented in figure II.9. Reduction of the phosphine oxide afforded the desired diphosphine scissor ligand **56**.

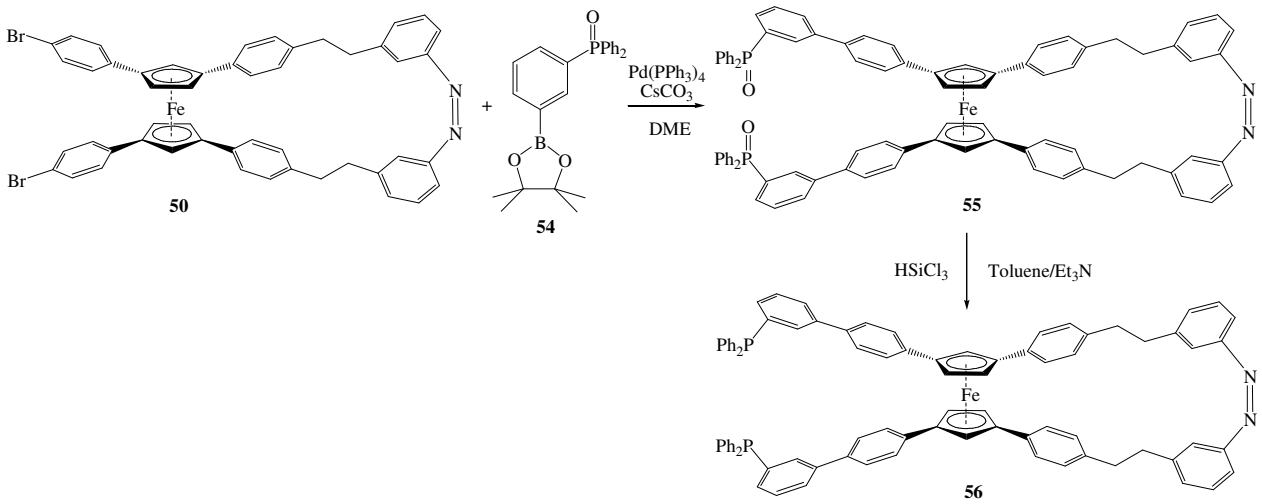

Figure II.9: Synthesis of diphosphine scissor ligand **56** from bromo scissors **50**.

5. Synthesis of scissor ligand 56

The synthesis of photoresponsive ferrocenyl bromo scissors **50** was carried out according to Aida's protocol [84] and is sketched in figure II.7. In the following sections, we treat each step of this synthesis individually and present the modifications, carried out in some of the cases, which led to significant improvements of the overall yield.

5.1. Formation of oxobutanoate

The synthesis began with a Friedel-Crafts reaction between succinic anhydride and bromobenzene catalyzed by aluminium chloride [104] which yielded oxobutanoic acid **44** after 4 days at room temperature. It was followed by esterification of **44** with ethanol, catalyzed by sulphuric acid, which afforded oxobutanoate **45** almost quantitatively as illustrated in figure II.10.

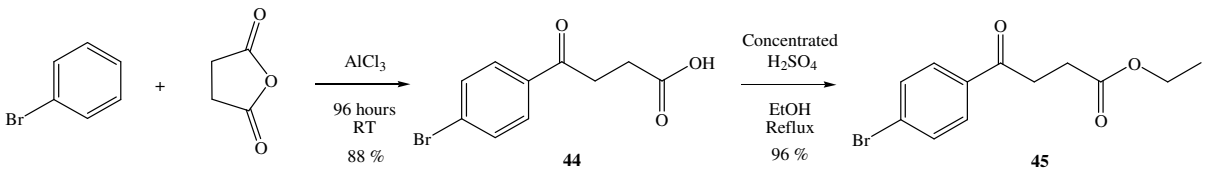

Figure II.10: Friedel-Crafts reaction leading to γ-keto acid **44** [104] and esterification yielding oxobutanoate **45**.

5.2. Cyclopentadiene formation

This synthetic step leading to a bisubstitued cyclopentadiene **46** was in fact a multi step reaction that starts with a ring condensation and ends with decarboxylation. It has caused us multiple problems, one of which forced us to abandon our first synthetic strategy. Indeed, the only synthesis of disubstituted cyclopentadienes, published in the 1930's, used sodium ethoxide as a base [103]. This outdated method produced **46** sporadically and only in very low yields that never exceeded 5%. After trying several methods using diverse conditions, we found out that using potassium *tert*-butoxyde rather than sodium ethoxide improved the yield dramatically up to 40 % for this reaction (figure II.11).

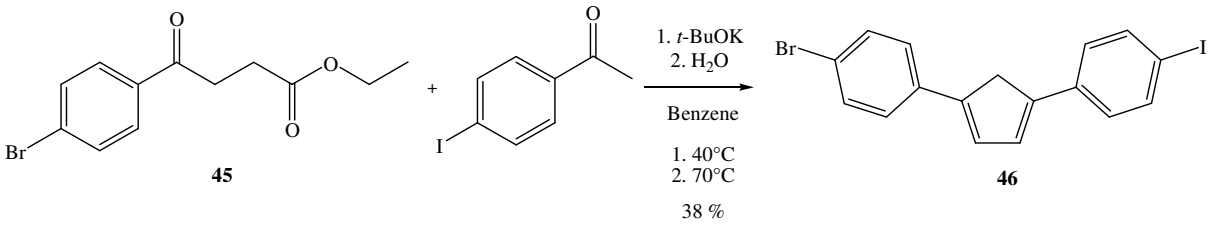

Figure II.11: Improved reaction of disubstituted cyclopentadiene **46** using potassium *tert*-butoxyde.

The proposed mechanism for this reaction is sketched in figure II.12.

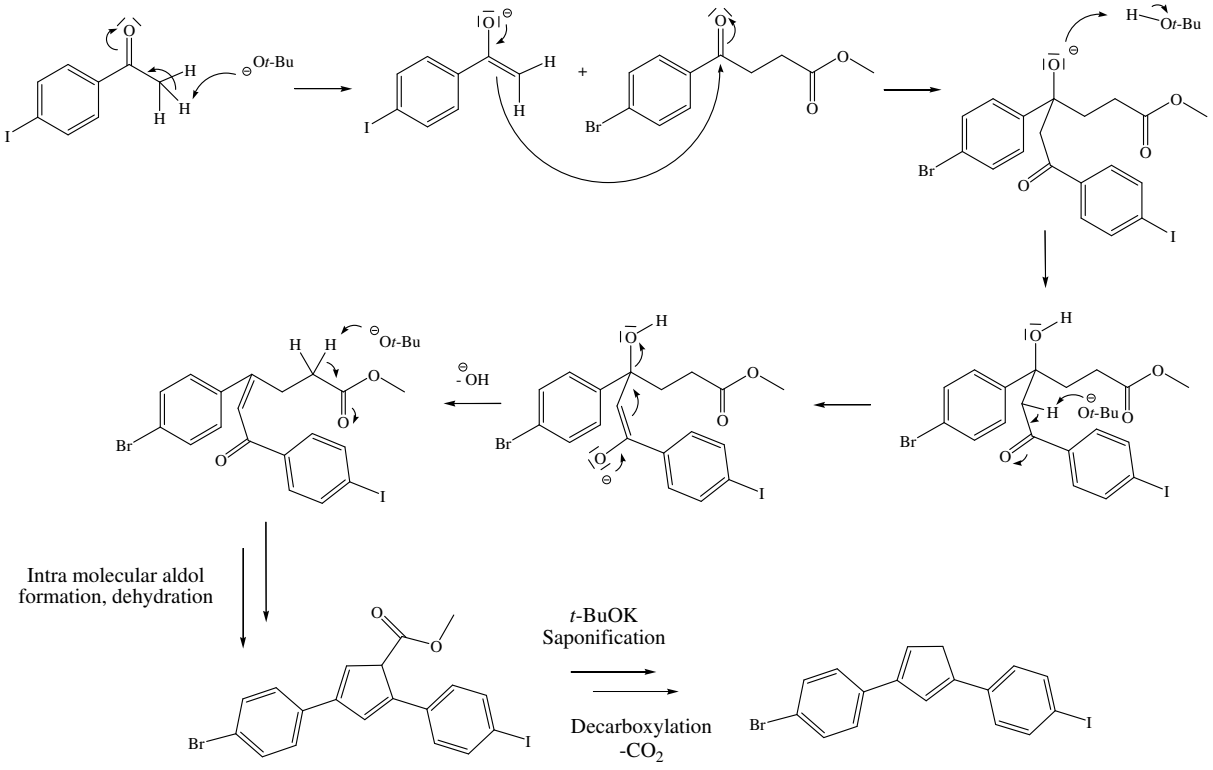

Figure II.12: Proposed mechanism for the formation of disubstitued cyclopentadiene **46**.

Liberated from this limiting step, we were able to synthesize enough material in order to finish the synthesis of the ligand. This new method offers great perspectives for the synthesis of disubstituted cyclopentadienes and therefore for 1,1',3,3'-tetrasubstituted ferrocenes.

Furthermore, both halides are easily and sequentially replaceable, an asset that could lead to new ferrocene designs.

Two characteristic set of peaks for cyclopentadiene aromatic and aliphatic protons were found at 6.53 and 3.01 ppm respectively. Furthermore, Matrix Assisted Laser Desorption/Ionization (MALDI) Time-Of-Flight (TOF) Mass Spectroscopy (MS) confirmed the NMR analysis with a dominant peak at m/z = 423 which attested for the formation of **46**.

5.3 Tetrasubstituted ferrocene synthesis

After deprotonation of cyclopentadiene **46**, the cyclopentadienyl anion coordinates to iron (II) affording 1,1',3,3'-tetrasubstituted-ferrocene **47** (figure II.13). Iron (II) was obtained through reaction of iron metallic powder and iron trichloride [105].

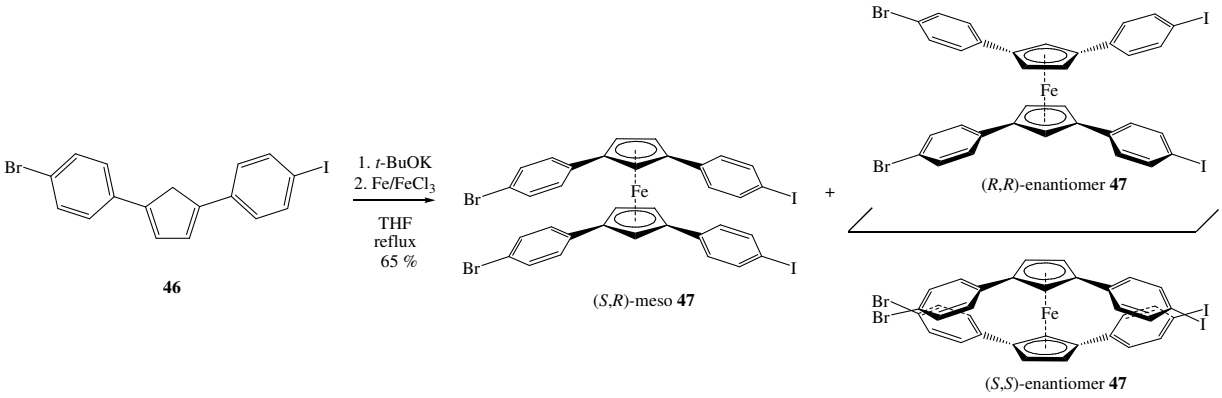

Figure II.13: Formation of 1,1',3,3'-tetrasubstituted ferrocene **47** in a diastereomeric mixture [105].

During this reaction, the two prochiral planar cyclopentadienyls can coordinate the iron from different faces introducing planar chirality to the system. Thereby, the cyclopentadienyl phenyl substituents can lie either in parallel or anti-parallel position to each other, generating (*R*,*R*), (S,S) and (*R*,*S*) diastereomers (figure II.13). For better understanding, figure II.14

explains the planar chirality in tetrasubstituted ferrocenes. These isomers were not isolated at this stage because the large amounts of product obtained would have taken too much time to be separated by chiral preparative HPLC. In the next sections, the representation of all three isomers was omitted for the sake of clarity.

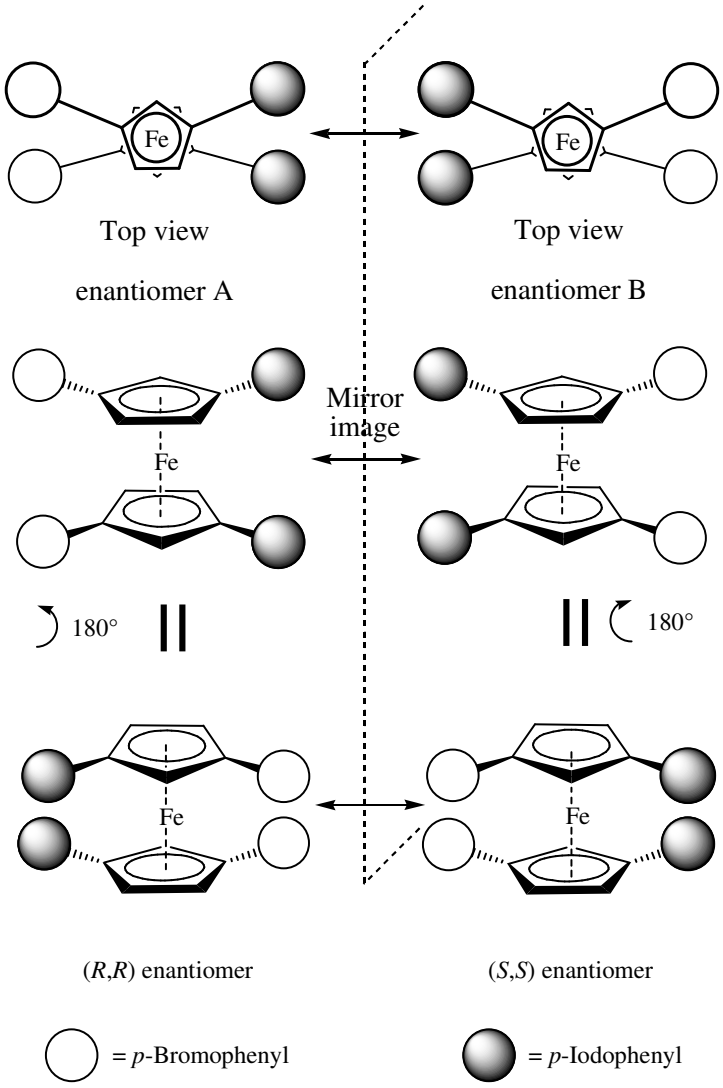

Figure II.14: Planar chirality in tetrasubstituted ferrocene.

Proton NMR with typical singlets at 4.52 ppm and 4.82 for the cyclopentadienyl protons (figure II.15) as well as MALDI-TOF MS spectrum (figure II.16) confirmed the ferrocene formation.

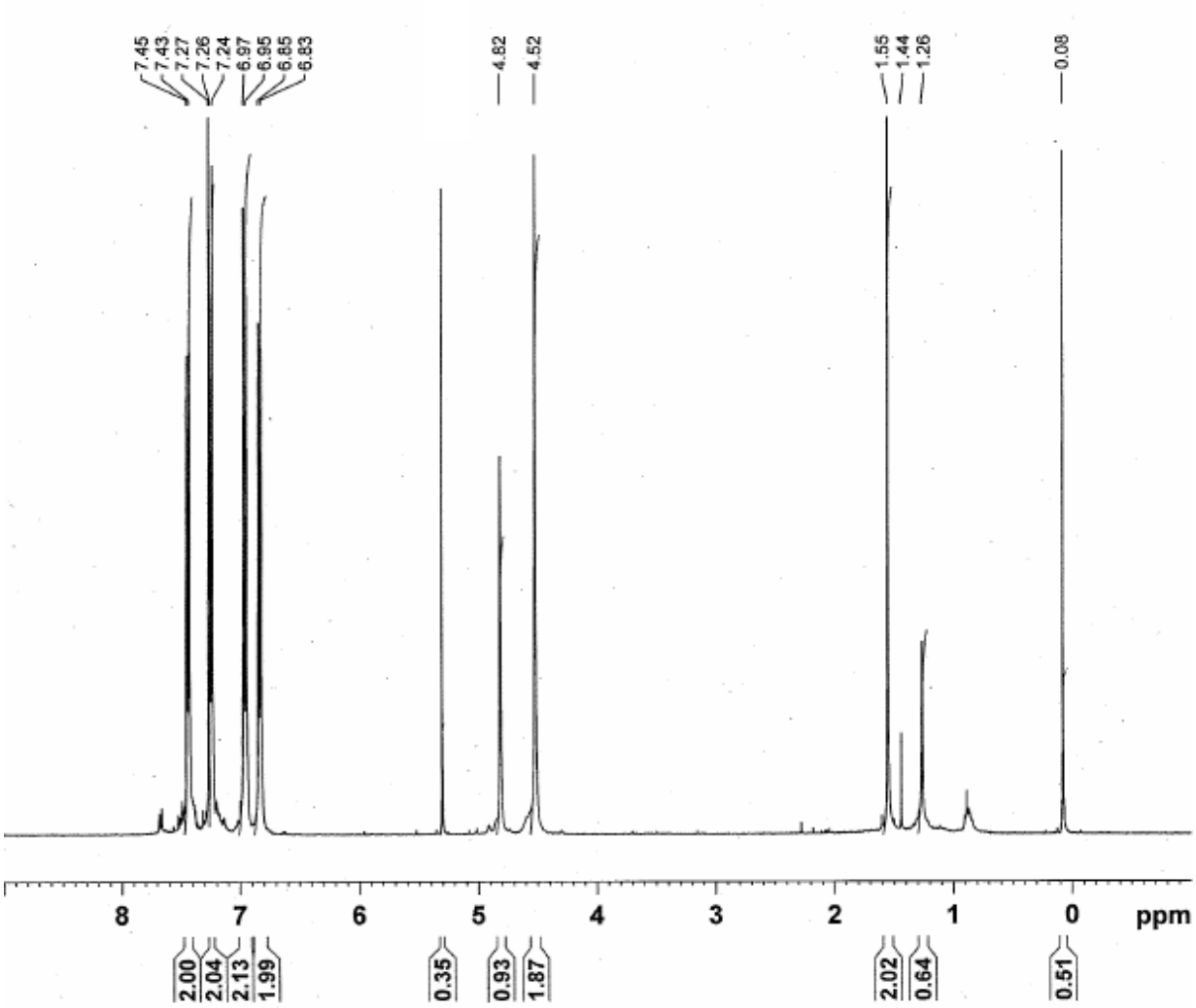

Figure II.15: Proton NMR spectrum of ferrocene **47** in CD_2Cl_2 with characteristic peaks for cyclopentadienyl protons at 4.52 and 4.82 ppm.

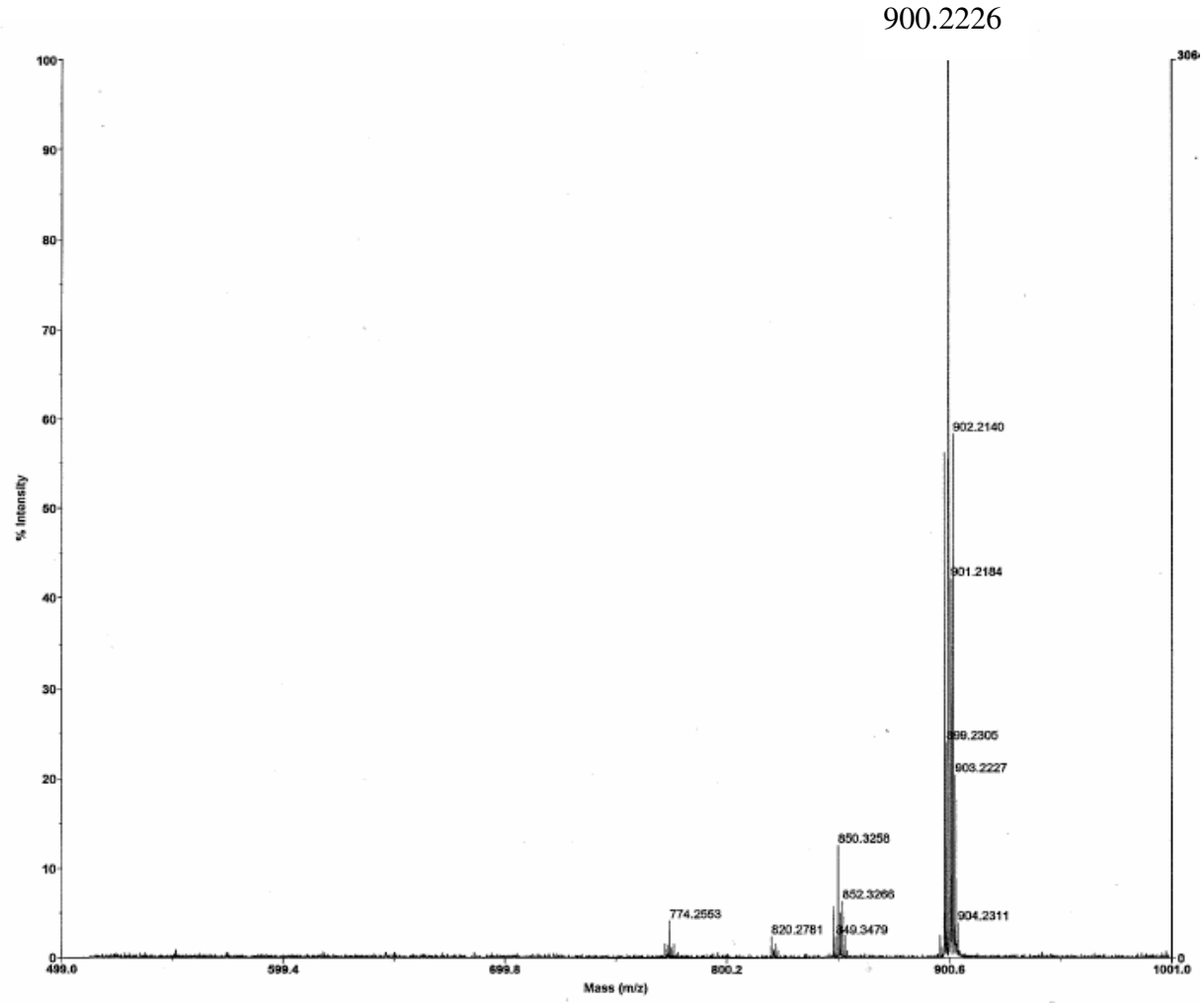

Figure II.16: MALDI-TOF mass spectrum of ferrocene **47** in dithranol matrix with a main peak at m/Z = 900.22, [M^+] calculated: 900.00 ($C_{34}H_{22}Br_2FeI_2$).

5.4. Sonogashira coupling

In order to introduce the azobenzene moiety, a Sonogashira coupling of **47** with 3-ethynylaniline catalyzed by palladium (II) in the presence of copper (I) iodide, produced the desired dialkyne ferrocene **48** almost quantitatively and selectively leaving the aryl bromide moiety untouched. The synthesis is presented in figure II.14 [106].

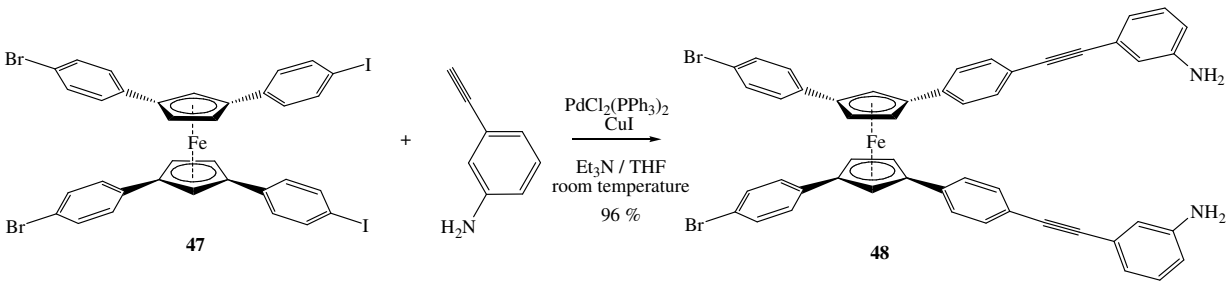

Figure II.17: Sonogahira reaction of ferrocene **47** and 3-ethynylaniline yielding ferrocene **48** [106].

MALDI-TOF mass spectrum, with a unique peak at m/z = 878, as well as NMR analyses proved that the product of the reaction is mainly composed of dialkyne **48** (figures II.18 and II.19).

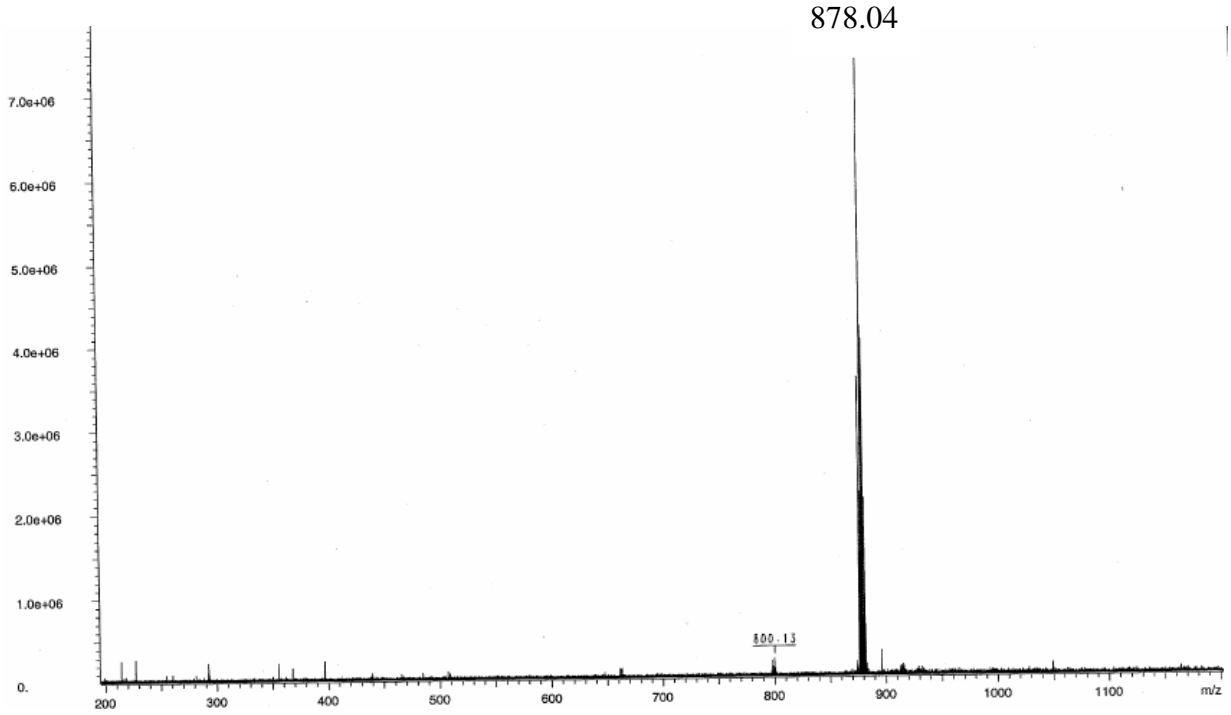

Figure II.18: MALDI-TOF MS spectrum of dialkyne ferrocene **48** displaying a pure compound with a peak at m/z = 878.04, [M^+] calculated: 878.47 ($C_{50}H_{34}Br_2FeN_2$).

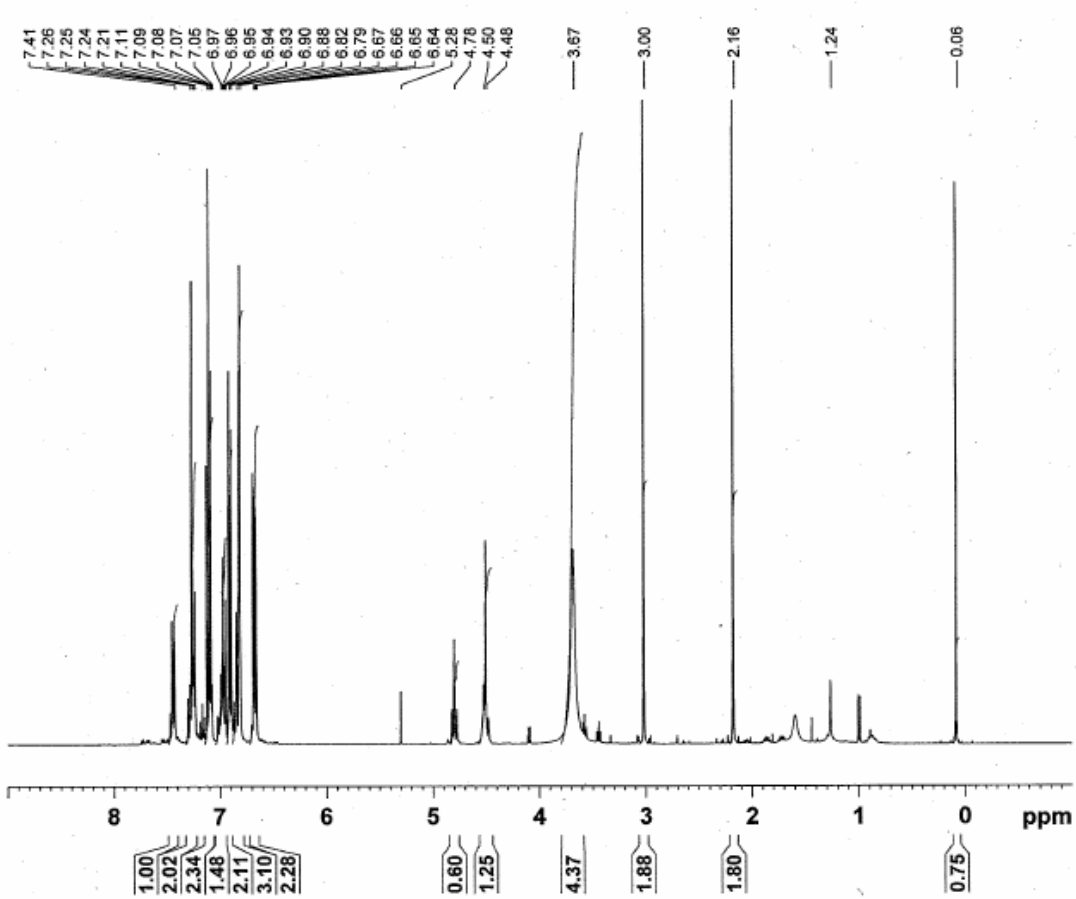

Figure II.19: Proton NMR spectrum of dialkyne ferrocene **48** exhibiting a broad singlet at 3.67 ppm, attesting for an insertion of 3-ethynylaniline in the ferrocene scaffold.

5.5. Reduction of alkynes

Mild hydrogenation of the alkyne moieties in dialkyne ferrocene **48** at 1 atmosphere H_2 catalyzed by platinum oxide (PtO_2, Adam's catalyst) [107] afforded the hydrogenated compound **49**. A MALDI-TOF mass analysis indicated the presence of the desired product at m/z = 886. However, we identified a side product debrominated ferrocene **49a** with a molecular weight of 808 g/mol due to reductive debromination of the bromobenzene blade (figure II.20).

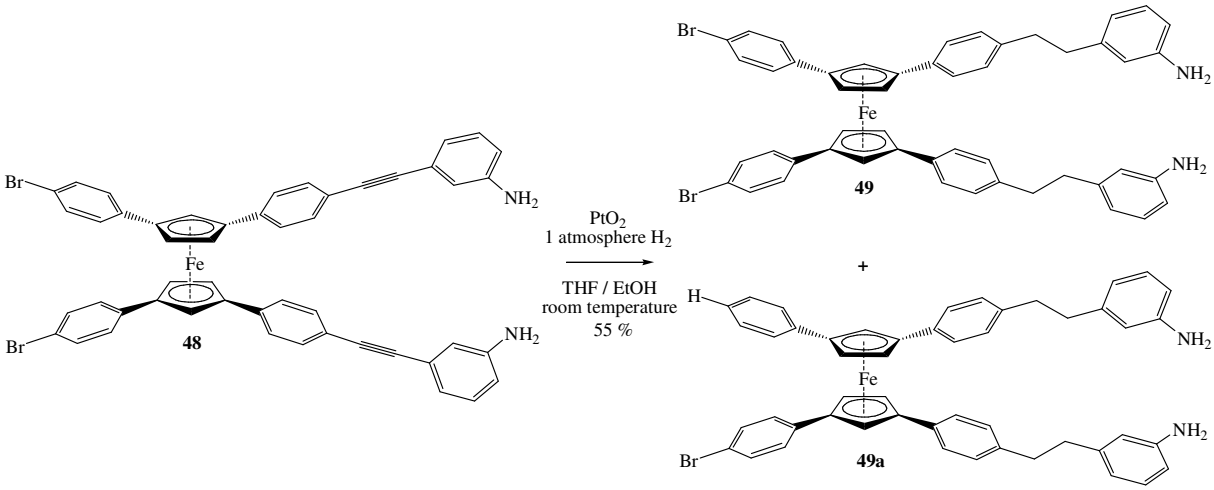

Figure II.20: Hydrogenenation of the alkyne moieties in **48** yielding ferrocene hexaaryl ferrocene **49** and side product debrominated ferrocene **49a**.

Because many factors intervene on this side reaction, we monitored the process by MALDI-TOF MS in an effort to minimize the debromation while allowing the completion of the hydrogenation (figure II.21).

The amount of side product formation of the debrominated ferrocene **49a** was governed by the mass percentage of PtO_2 used. The best compromise was obtained with a 10 % mass loading of Adam's catalyst. Under these conditions 20 % of mono bromo ferrocene **49a** were produced. All efforts to get rid of this side product by silica gel chromatography were unfruitful. We thus pursued the synthesis bearing side product **49a** that was separated at a later stage.

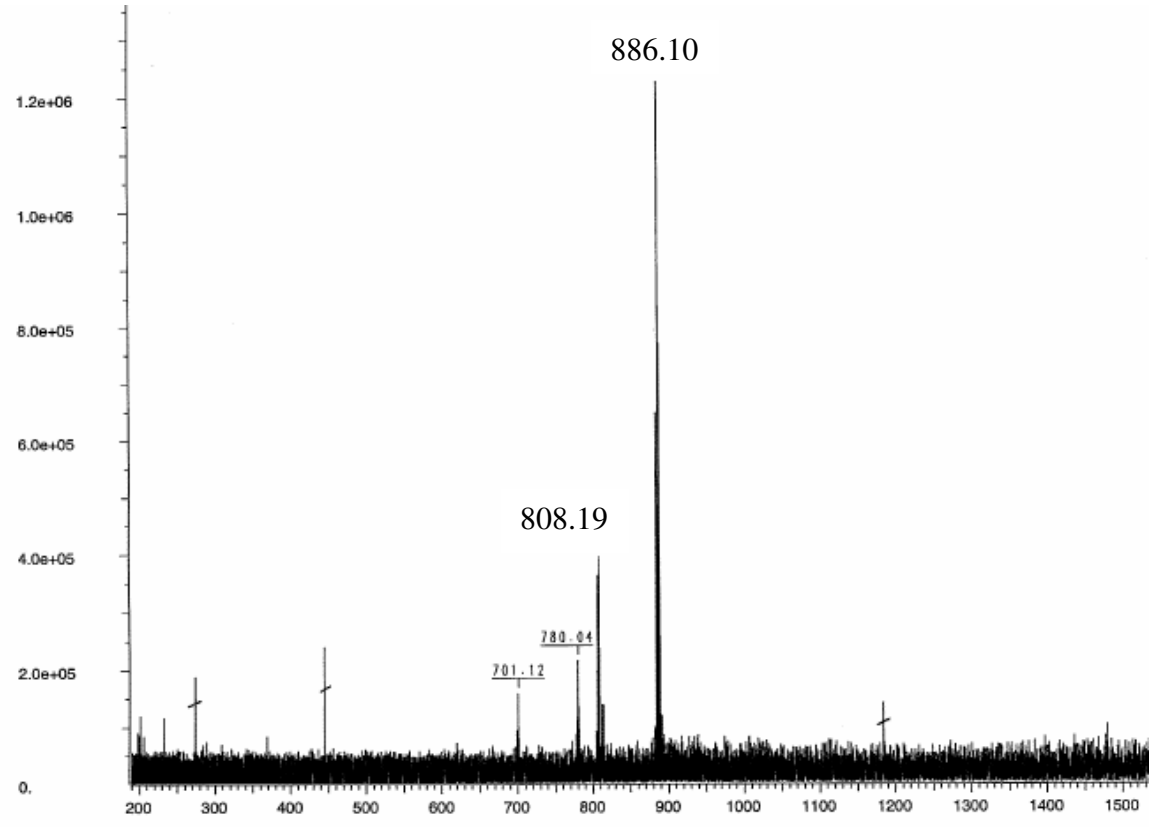

Figure II.21: MALDI-TOF MS of hexaaryl ferrocene **49** (m/z = 886.10) and its debrominated counterpart **49a** (m/z = 808.19). Major peak, [M^+] calculated: 886.53 ($C_{50}H_{42}Br_2FeN_2$).

5.6. Azobenzene formation

The final step towards bromo scissors consisted in linking the handles of the scissors with an azo moiety. It was achieved through oxidation of the primary amines in hexaaryl ferrocene **49** with air and copper (I) chloride in pyridine which yielded bromo scissors **50** [108] as presented in figure II.22. The reaction yields a mixture of *cis*- and *trans*- configurations of the azobenzene moiety as evidenced in the proton NMR spectrum with two different doublets for the aliphatic protons at 2.92 and 3.15 ppm. In the following sections, if not specified otherwise, the representations of both *cis* and *trans* azobenzene is omitted for the sake of clarity. In order to avoid the formation of diazo dimers, the reaction was usually carried out in

very dilute pyridine solutions [108]. As we were able to synthesize very large quantities of the hydrogenated hexaaryl ferrocene **49**, more than 50 liters of pyridine would have been necessary to carry out the reaction adequately. To prevent dimerization, we carried out the reaction at much higher concentration but added the pyridine solution containing hexaaryl ferrocene **49** dropwise (over 2 hours) to the CuCl solution. Although this method produced acceptable yields (31 %), the results were lower than those reported by Aida using low concentration (51 %) [84].

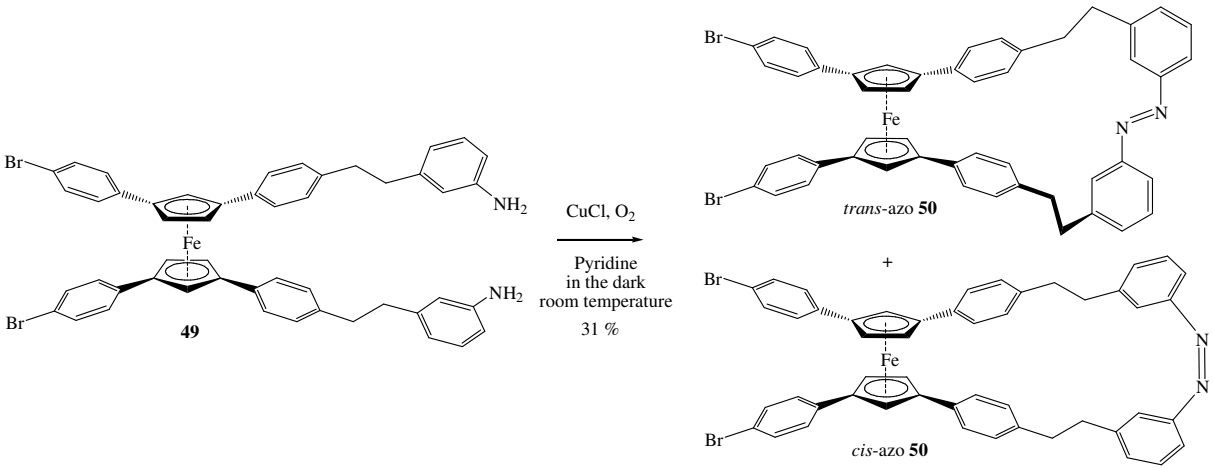

Figure II.22: Synthesis of bromo scissors **50** by oxidation yielding *trans* and *cis* diastereomers.

The MALDI-TOF MS spectrum (figure II.23) displayed a peak at m/z = 882.07, confirming the formation of the azobenzene link.

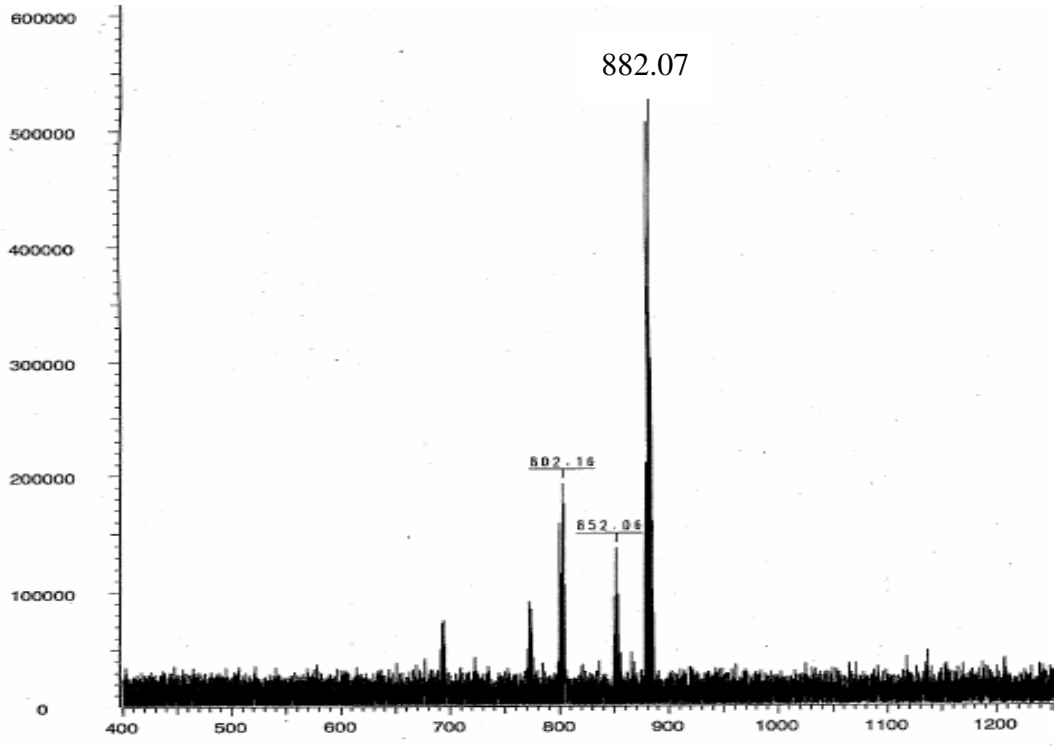

Figure II.23: MALDI-TOF MS spectrum of bromo scissors **50** with a major peak at m/z = 882.07, [M^+] calculated: 882.50 ($C_{50}H_{38}Br_2FeN_2$).

The disappearance of the broad signal due to the protons of the amines provided additional evidence for the formation of the azobenzene strap (figure II.24).

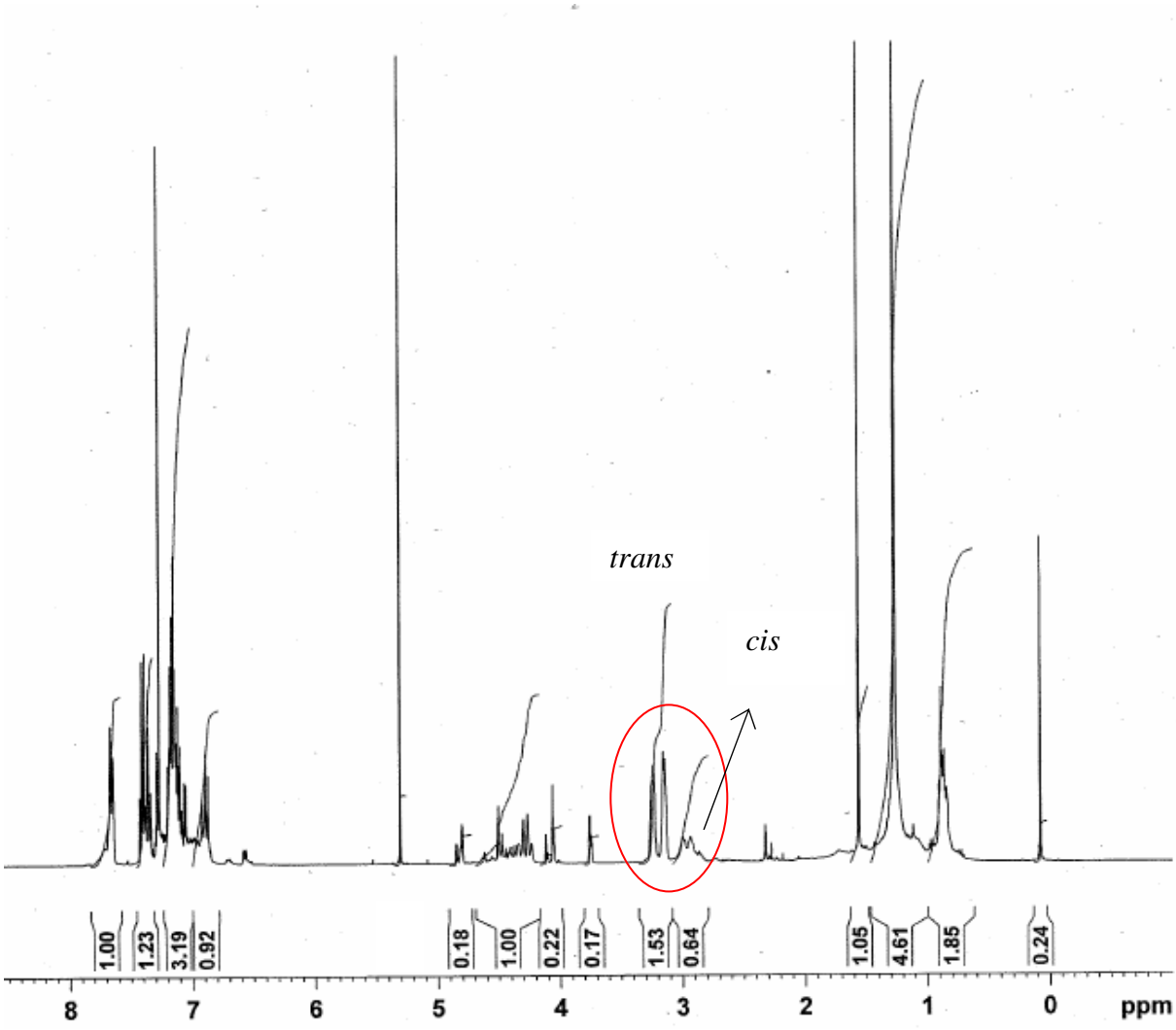

Figure II.24: Proton NMR spectrum of bromo scissor **50** displaying the disappearance of the broad amine's proton signal around 3.50 ppm and exhibiting two doublets for the aliphatic protons from both *cis* and *trans*-**50** at 2.92 and 3.15 respectively (circled in red on the spectrum).

We also noticed a change of color from light-orange to dark-orange which is in accord with the formation of the azobenzene link. Indeed, as a consequence of electron delocalisation, aryl azo compounds exhibit vivid colours and are often used as dyes.

5.7. Synthesis of phosphinated scissors blades

To introduce phosphine functionalities in the scissor scaffold, we carried out a Suzuki cross-coupling between the boronate **54** and the bromo scissors **50**. As this coupling is catalyzed by $[(PPh_3)_4Pd]$ complex, the phosphine group on boronate **58** had to be oxidised to prevent inhibition of the catalytic cycle. We selected the 1,3-substituted dibromobenzene with the ligand design in mind as depicted in figure II.25. Indeed, we speculated that a 1,4-substitution pattern may have imposed a greater distance between the coordinating units leading to greater difficulties in the complexation of the nickel.

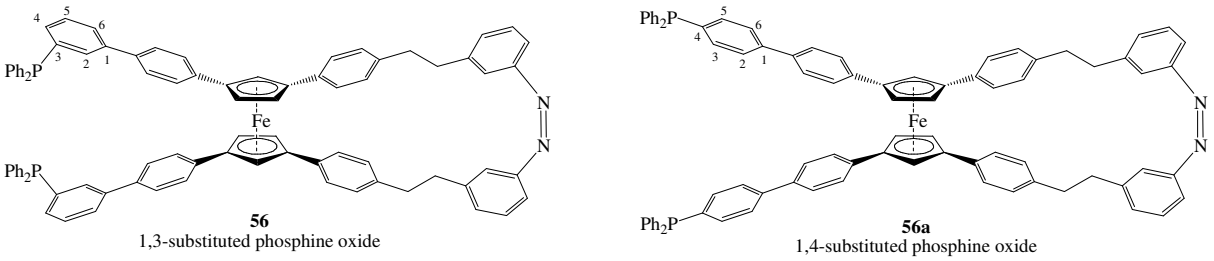

Figure II.25: Comparison between 1,3 and 1,4-substituted blades showing the arrangement of the coordinating phosphine moieties. In ligand **56**, the phosphines functions are in closer proximity than in **56a**.

The synthesis of protected boronate **54** was carried out according to the method reported by Diederich and coworkers [109] as presented in figure II.26.

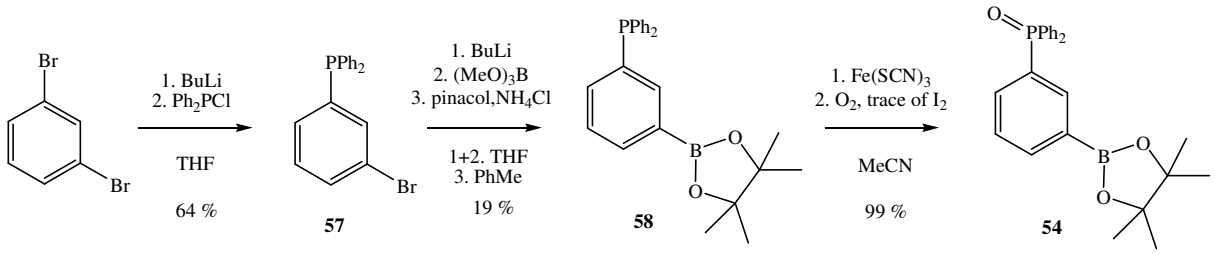

Figure II.26: Synthesis of the scissor's blades.

Mono-lithiation of 1,3-dibromobenzene and quenching with chlorodiphenylphosphine afforded bromophosphine **57**. Spetroscopic ^{31}P NMR analysis (figure II.27) showed a single peak at -4.06 ppm which corresponds to typical triarylphosphine chemical shifts.

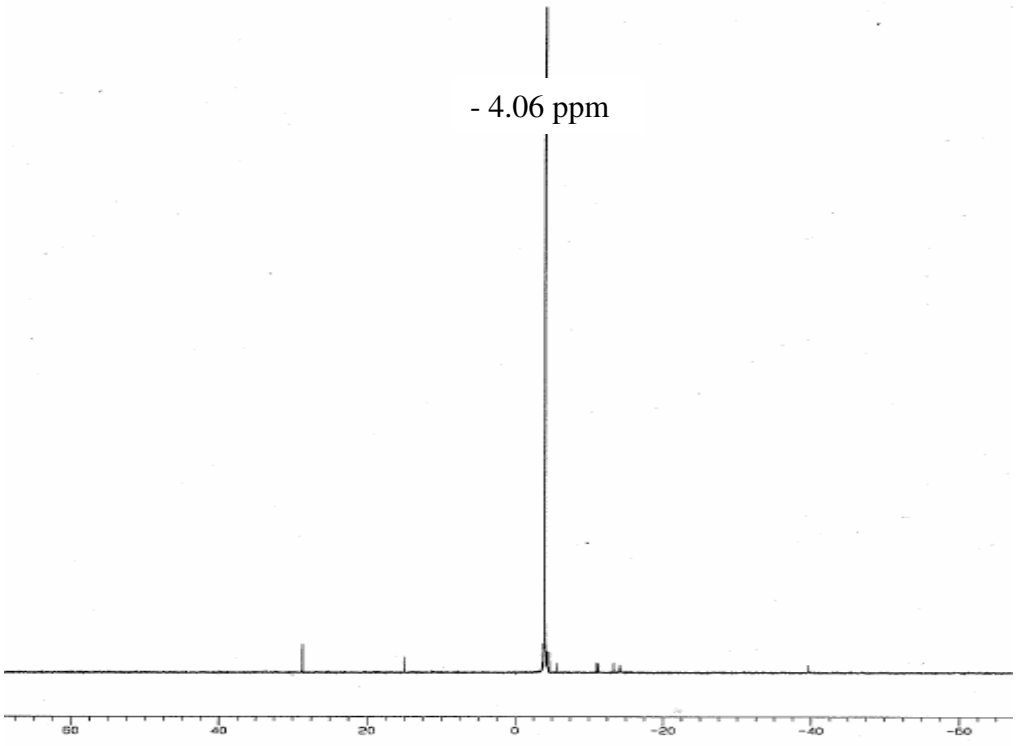

Figure II.27: Phosphorus NMR spectrum of **57** with a characteristic peak for triarylphosphine at -4.06 ppm.

A second lithiation followed by quenching with trimethyl borate and subsequent acid-promoted transesterification with pinacol yielded boronate phosphine **58**. Typical ^{1}H NMR singlet, specific for methyl protons, was found at 1.32 ppm and attested the presence of the desired product. Boronate phosphine **58** was then protected via oxidation according to an improved method reported by Ondrejovic and coworkers [110]. The oxidation was achieved within 15 minutes by bubbling O_2 gas through an acetonitrile solution of boronate phosphine **58,** at reflux in the presence of catalytic amounts of $Fe(SCN)_3$ and a trace of I_2, which provided phosphineoxide boronate **54** quantitatively. Phosphorus NMR peak for the free phosphine dramatically shifted downfield from -5.90 to 29.76 ppm confirming the oxidation of the phosphine (figure II.28).

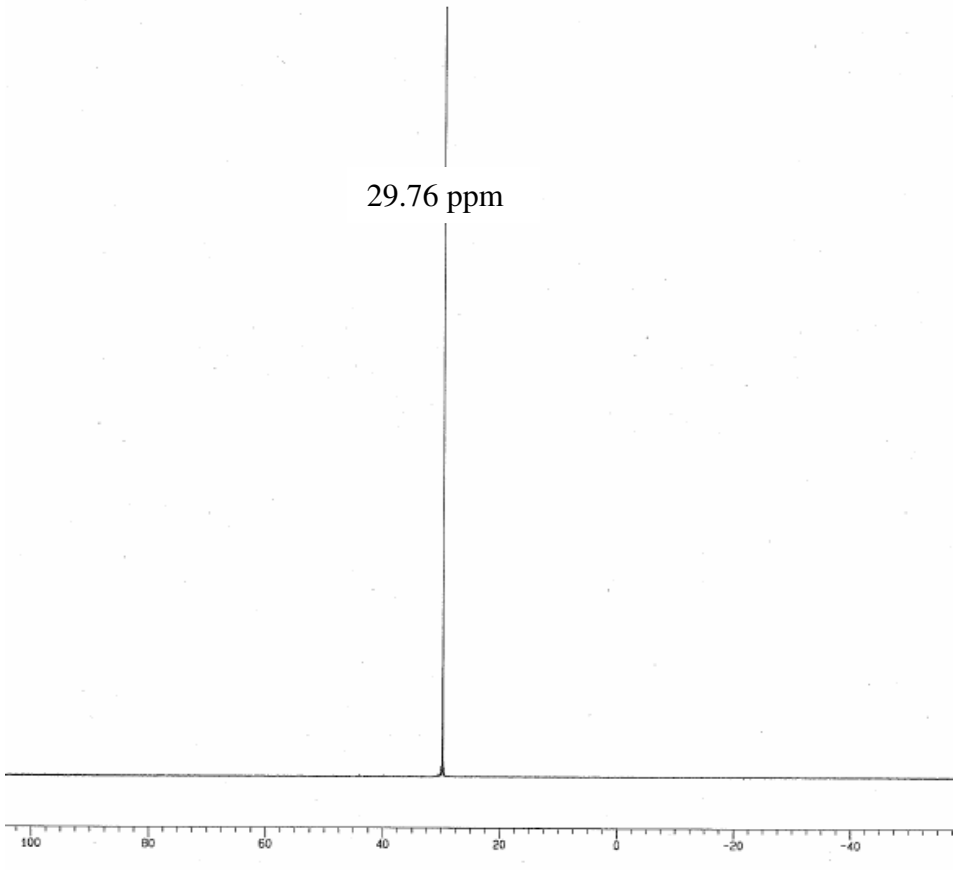

Figure II.28: ^{31}P NMR spectrum with a single peak at 29.76 ppm attesting for the oxidation of phosphine boronate **58** into phosphine oxide boronate **54**.

5.8. Suzuki cross-coupling reaction

The protected boronate **54** was coupled to the bromo scissors **50** via Suzuki cross-coupling reaction [111]. For this purpose tetrakistriphenylphosphine palladium (0) in the presence of Cs_2CO_3 was used as a catalyst to produce the protected diphosphine **55** in 35 % yield (figure II.29).

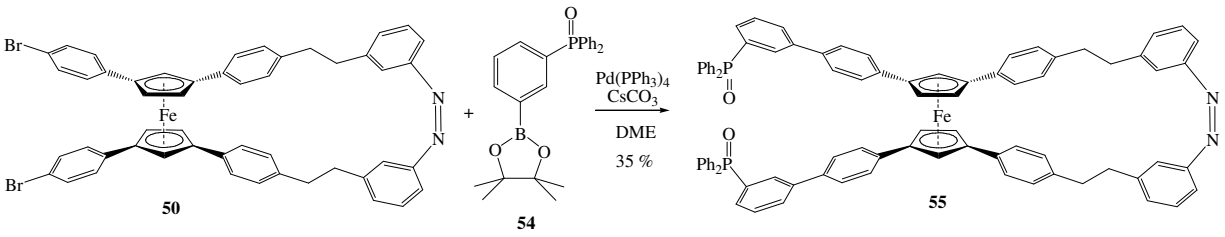

Figure II.29: Suzuki cross-coupling reaction between protected boronate **54** and bromo-scissors **50**.

A single set of peaks centered at m/z = 1277 in MALDI-TOF as well as the ^{1}H-NMR analysis attested that the majority of the product was in fact compound **55**.

5.8.1. Enantiomer and diastereomer separation

As the reduced diphosphine scissor ligand **56** was expected to be air-sensitive we set out to separate the diastereomers that were produced during the ferrocene formation (section 5.3) on the diphosphineoxide **55**. We thus carried out a recycling high pressure liquid chromatography (HPLC) with a chiral preparative column (Chiralpak IA) using a mixture of CH_2Cl_2:ethanol 97:3 as eluent which separated both enantiomers as well as the *meso* compound. The recycling system consisted in reinjecting the sample many times through the

column until a baseline separation of the stereoisomers was achieved. Multiple cycles were necessary in order to separate the three stereoisomers completely as displayed in the chromatogram (figure II.30). The spectrum also displayed further peaks due to impurities that were removed during the purification process.

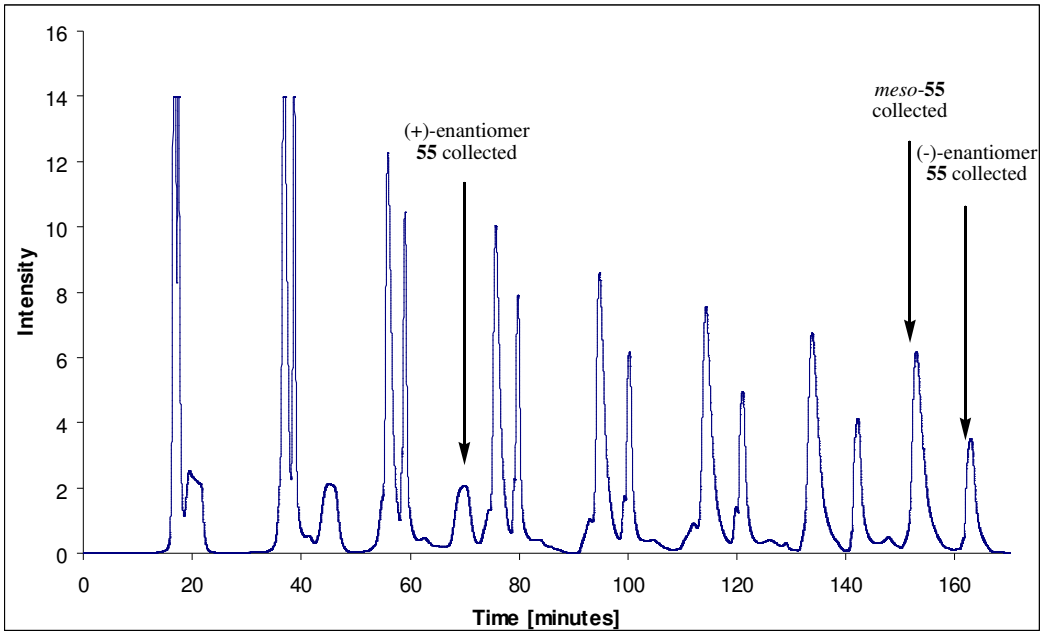

Figure II.30: Purification chromatogram for the stereoisomers of phosphineoxide **55** using a mixture of CH_2Cl_2:ethanol 97:3 as eluent. The sample was reinjected in the column numerous times which led to a base line separation of the stereoisomers of **55**.

Circular dichroism (CD) analysis (figure II.36) attested for the isolation of each stereoisomer. MALDI-TOF mass assays demonstrated that each stereoisomer was separated from the impurities, for instance *meso*-**55** was perfectly isolated (figure II.31).

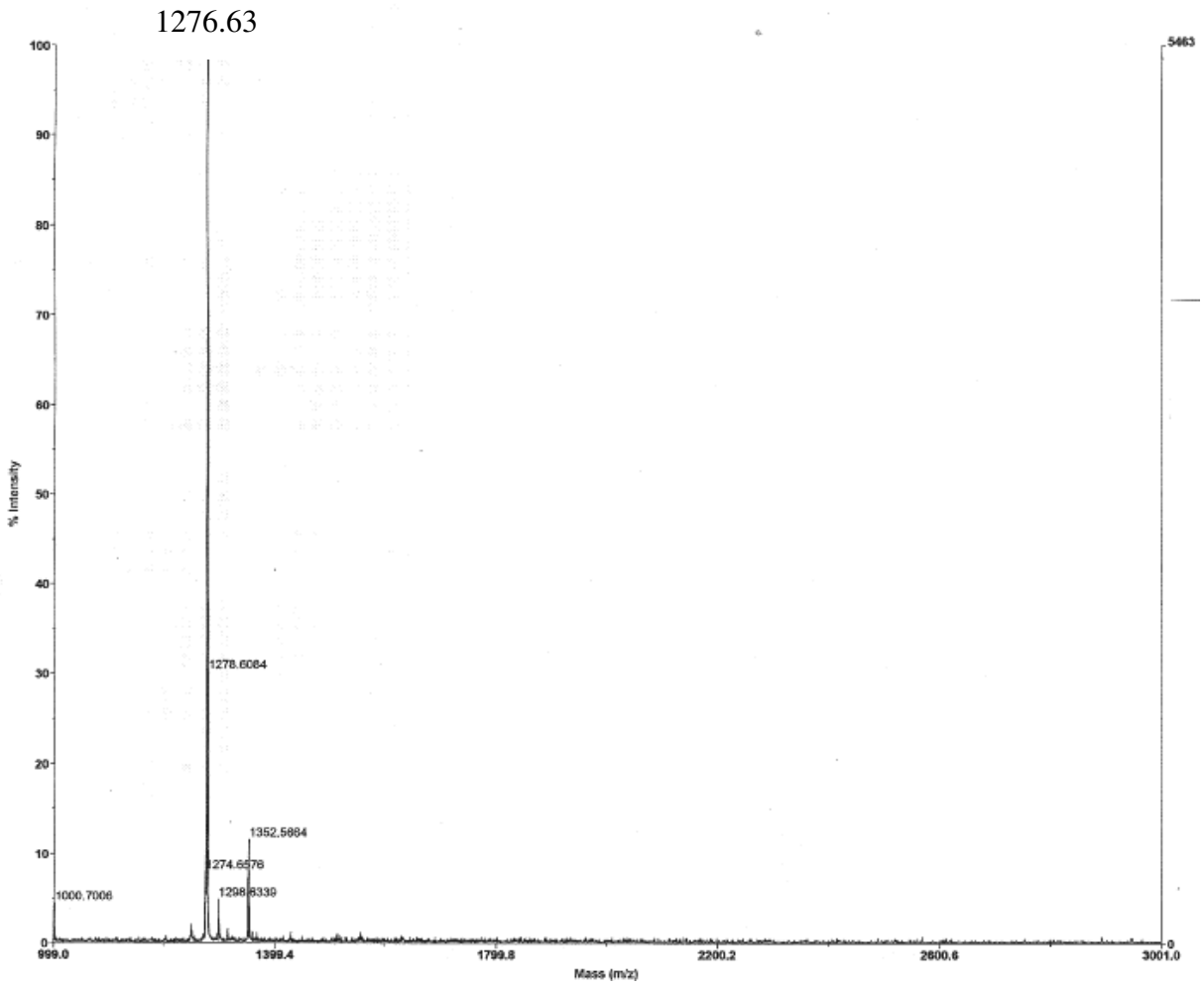

Figure II.31: MALDI-TOF MS spectrum of *meso*-**55** (with a major peak at m/z = 1276.63, $[M]^+$ calculated: 1277.25 ($C_{86}H_{66}FeN_2O_2P_2$)) after HPLC purification.

^1H and ^{31}P NMR analysis of diphosphineoxide scissors *meso*-**55** were also conducted as displayed in figures II.32 and II.33. The ^1H NMR spectrum displayed two sets of doublet centered at 2.93 and 3.19 ppm that represented the aliphatic protons in the handles of respectively *cis* and *trans*-azobenzene *meso*-**55.** We calculated the *cis*:*trans* ratio (15:85) according to the integrals of the doublets on the ^1H NMR spectrum, which corresponds to the ratio calculated by HPLC in a further section (figure II.40). Moreover, the ^{31}P NMR spectrum displayed two major signals at 29.67 and 29.57 ppm, confirming that the mixture is composed

of *trans-meso*-**55** and *cis-meso*-**55** isomers respectively. Indeed, the phosphorus and hydrogen atoms find themselves in different electronic environments due to the different configuration of the diastereoisomers and thus exhibit dissimilar chemical shifts.

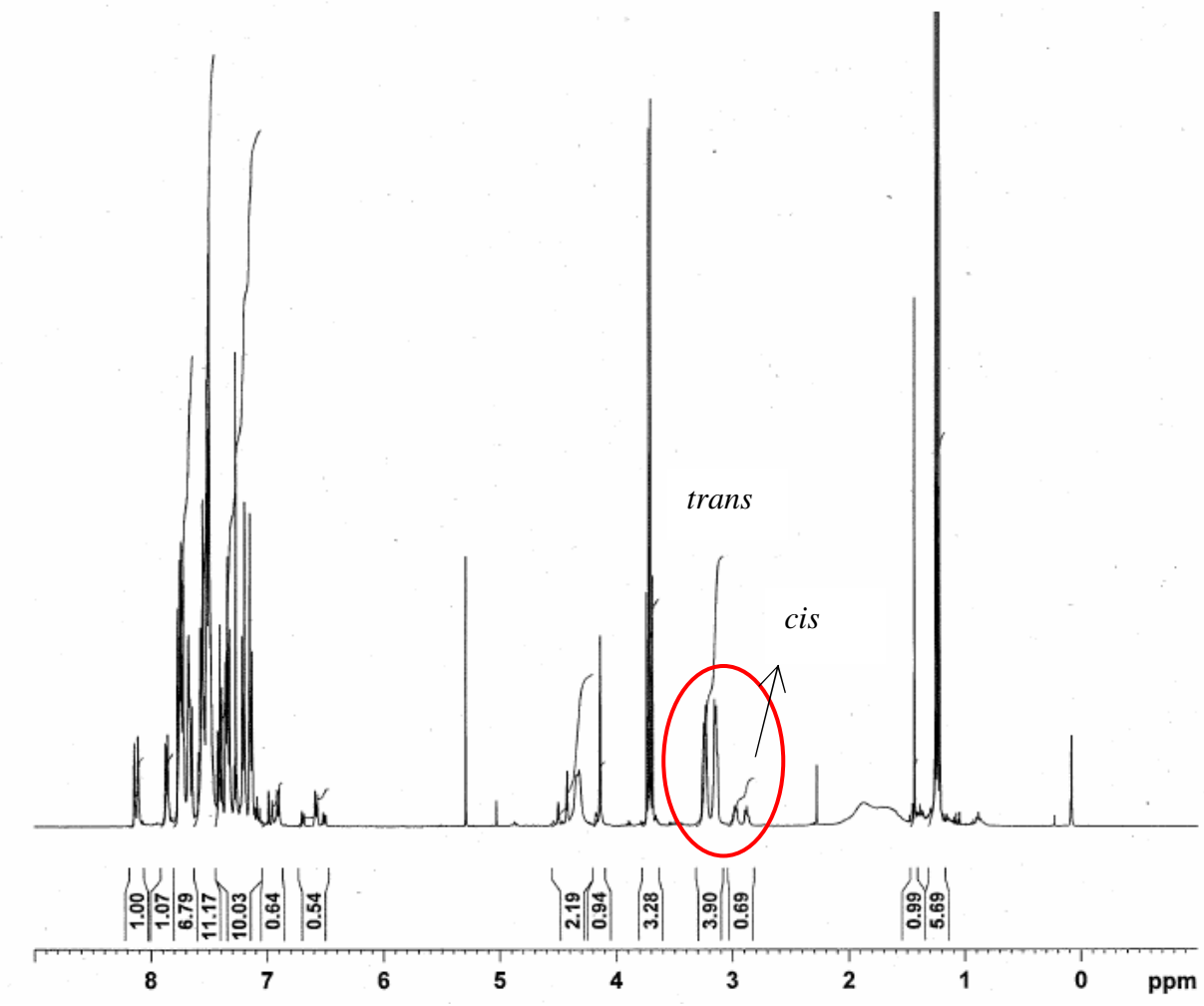

Figure II.32: Proton NMR spectrum of diphosphine oxide *meso*-**55** displaying both *cis* and *trans* diastereoisomers at 2.93 and 3.19 ppm respectively (circled in red on the spectrum).

a. **b.**

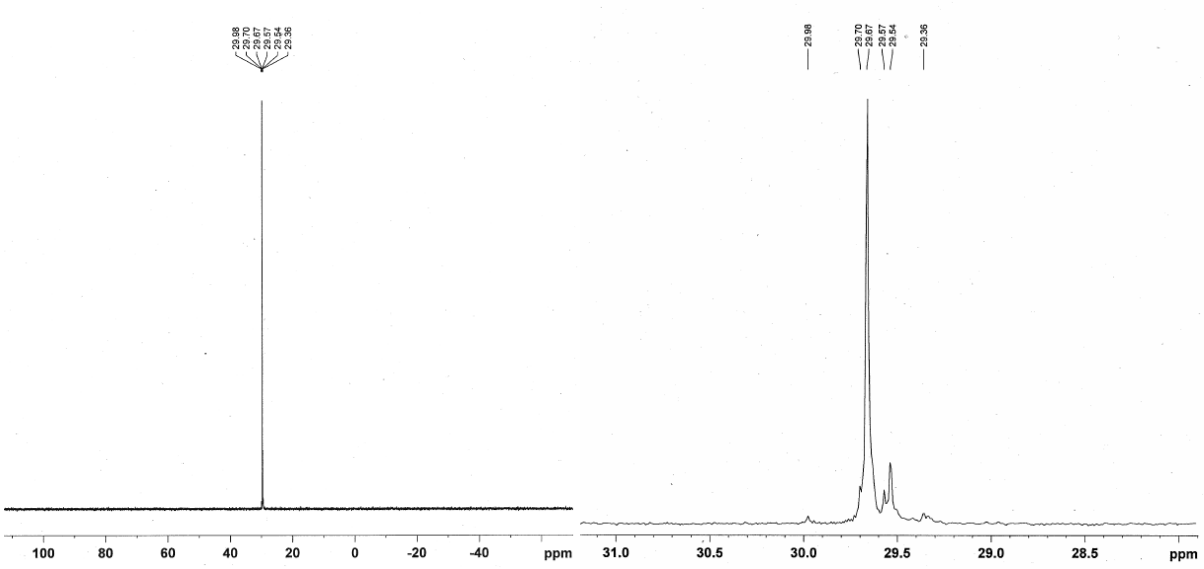

Figure II.33: **a**, phosphorus NMR spectrum of diphosphine oxide *meso*-**55** with a main signal at 29.67 ppm; **b**, enlargement of the region of interest.

5.8.2. Structural considerations

Based on the observation made by Aida and coworkers on the structure of molecular scissors **24** [85], we anticipated that the *meso* and *racemic*-**55** display different geometries. The main structural differences between *meso* and enantiomers forms of the scissors are presented in figure II.34 and II.35. Generaly, in the *trans*-configuration, the blades of *meso*-scissors are opened whereas the blades of the *trans*-enantiomers are closed. Consequently, the motion of the blades occurs in opposite directions.

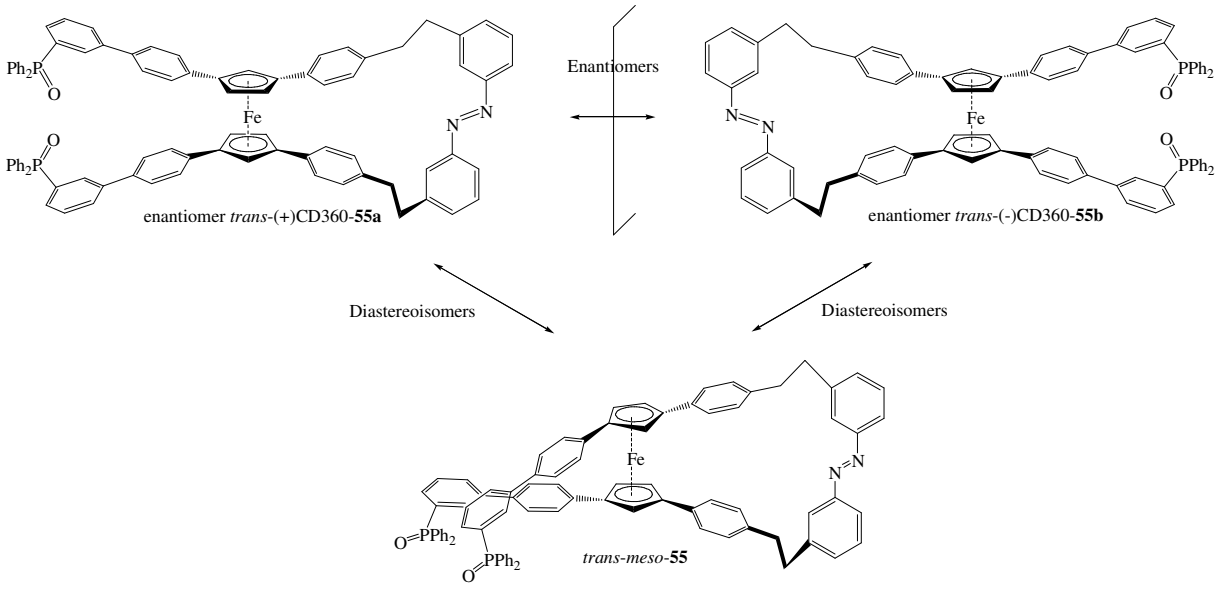

Figure II.34: Stereomers of diphosphineoxide scissors **55**; (+) or (-) denomination are determined from the sign of the CD signal at 360 nm (figure II.36).

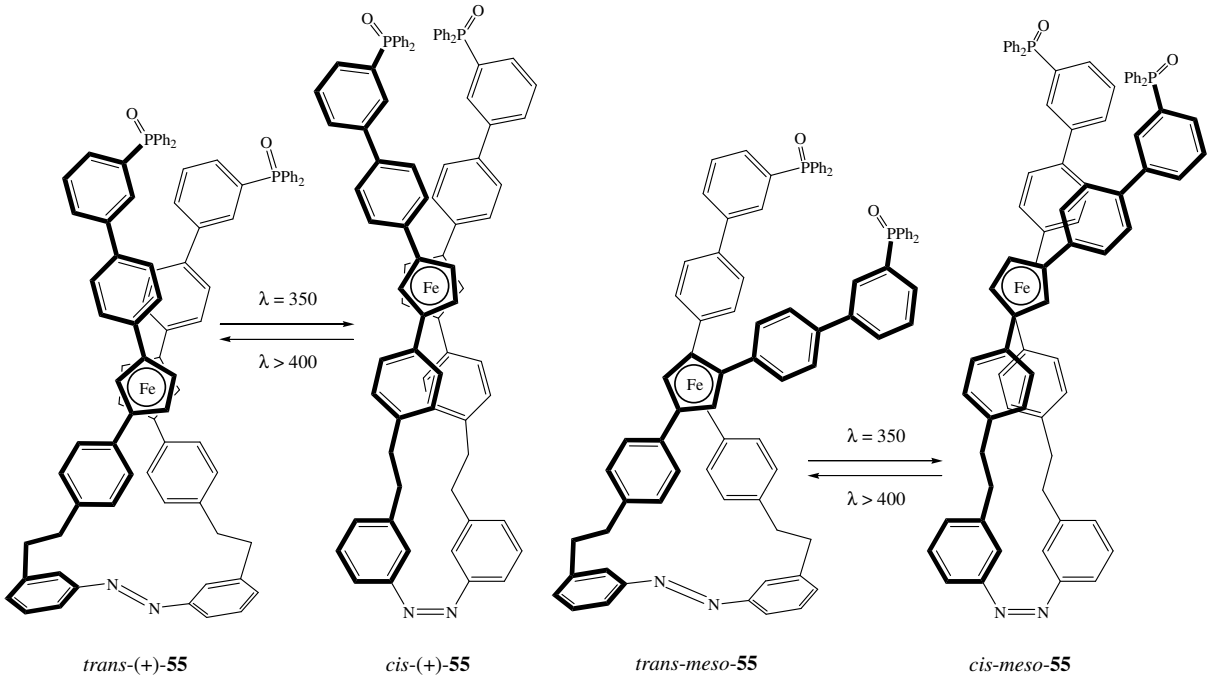

Figure II.35: Schematic representation of the structural changes between *trans* and *cis* configurations for the enantiomer and *meso* forms of diphosphineoxide **55** upon photoisomerization [85].

5.8.3. Circular dichroism analysis

The enantiomer separation of the phosphine oxide **55** was confirmed by CD spectroscopy as depicted in figure II.36. The analysis of the *meso* compound was found to be CD silent (figure II.37).

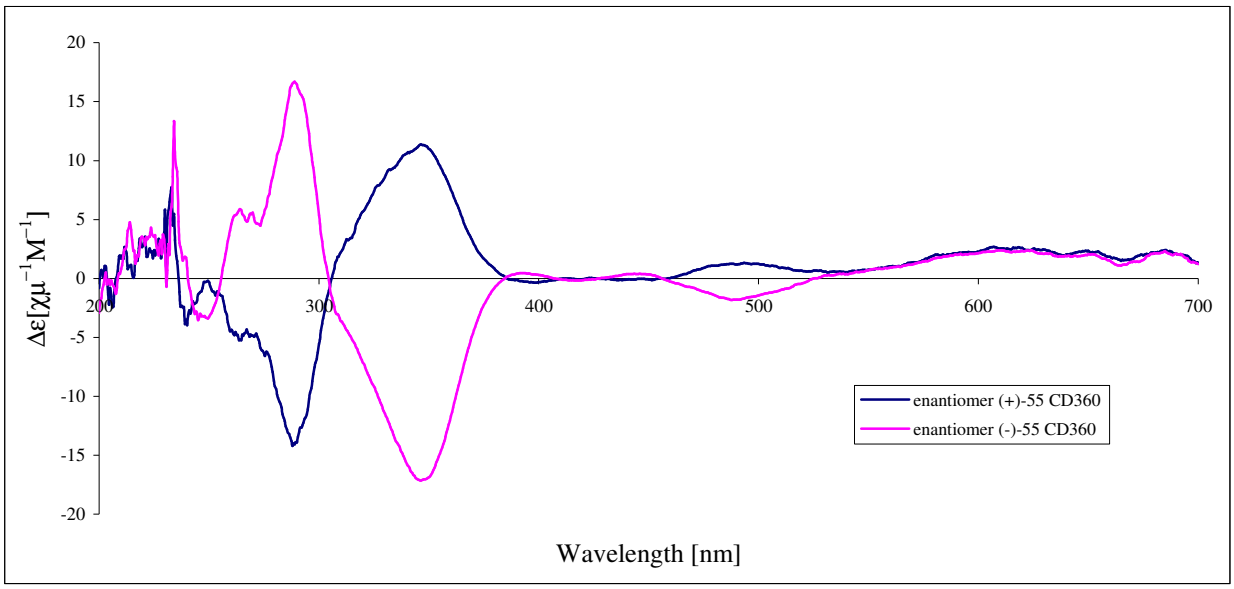

Figure II.36: Circular dichroism spectrum of both enantiomers of **55**. Blue, enantiomer (+)$_{CD360}$-**55**; purple, enantiomer (-)$_{CD360}$-**55**.

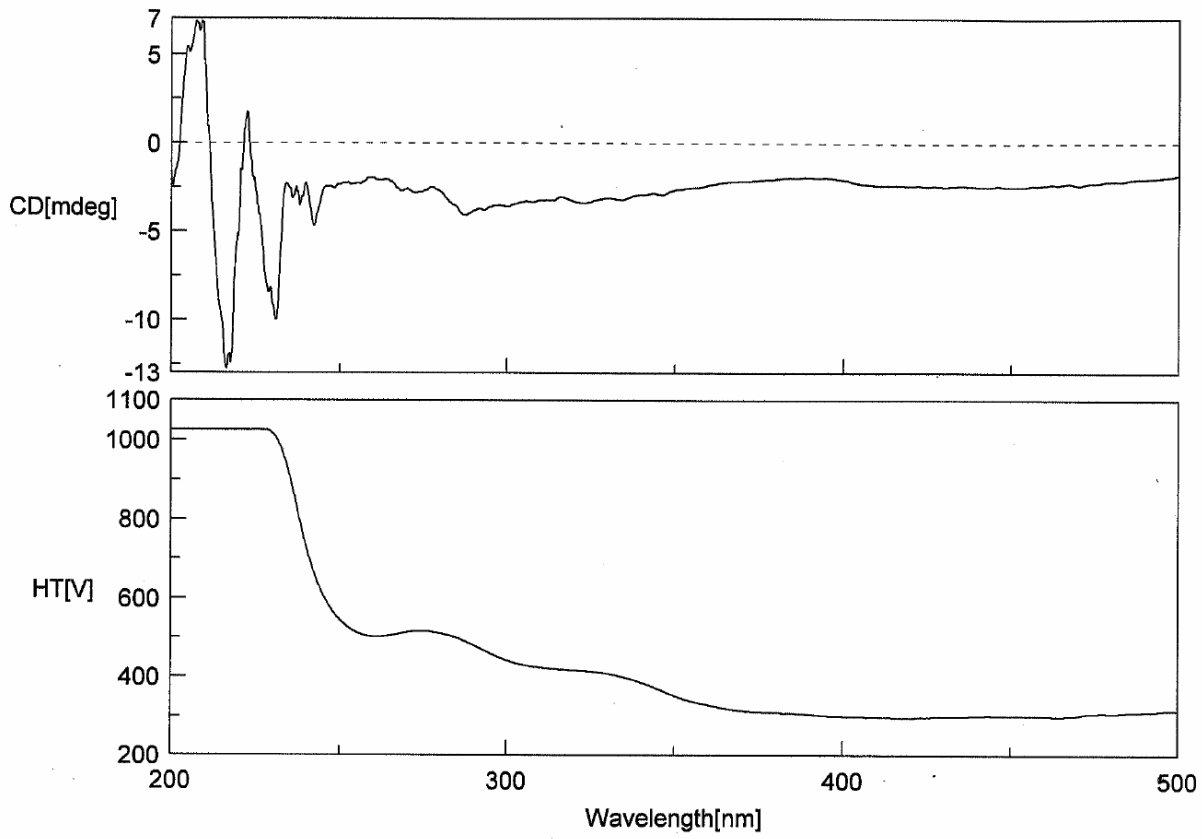

Figure II.37: Circular dichroism spectrum for *meso*-**55** exhibiting a silent response as expected.

5.8.4. Behaviour of the stereoisomers of 55 upon UV-Vis illuminations

The three stereoisomers of **55** were irradiated by either UV or visible light in degassed dichloromethane solutions at room temperature. The process was monitored by absorption spectroscopy while illuminations were carried out by successive irradiations until a photostationary state was reached. Figure II.38 displays a solution of *meso* **55** upon irradiation with 350 nm UV light which was accompanied by a spectral change between 225 nm and 375 nm. Sharp isosbestic points at 265, 287, 300 and 373 nm suggested that the isomerization of the azobenzene unit from *trans* to *cis* was complete after 415 seconds without any side

product formation. Changes in absorption bands reflected the rotary motion of *meso*-**55** around the ferrocene pivot.

a **b**

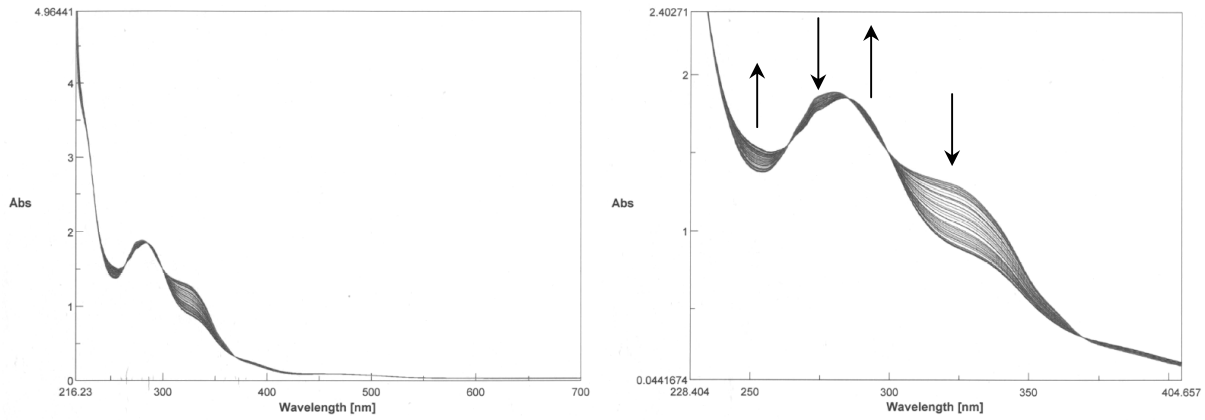

Figure II.38: **a,** Spectral changes of diphosphine oxide *meso*-**55** at room temperature upon 415 seconds UV (λ = 350 nm) irradiation. **b,** Enlargement of the region between 225 and 400 nm and spectral behaviour.

Reversibly, backwards irradiation with visible light (λ > 400 nm) switched the azobenzene back from *cis* to *trans* configuration. This reverse photoisomerization (*cis-trans)* took place much faster than the opening of the blades (47 seconds instead of 415 seconds for UV). As presented in figure II.39, the absorbance curves failed to revert back totally to the initial spectrum (ie. before illumination, included as a reference in the graph). It indicated that the isomerization did not proceed back to its original *cis-trans* ratio. This phenomenon (photostationary *cis-trans* mixture) is well known in the field of azobenzene chemistry [34-38]. Furthermore, sharp isosbestic points at the same wavelengths than the UV irradiation suggested that no side products were formed in the reverse irradiation.

a **b**

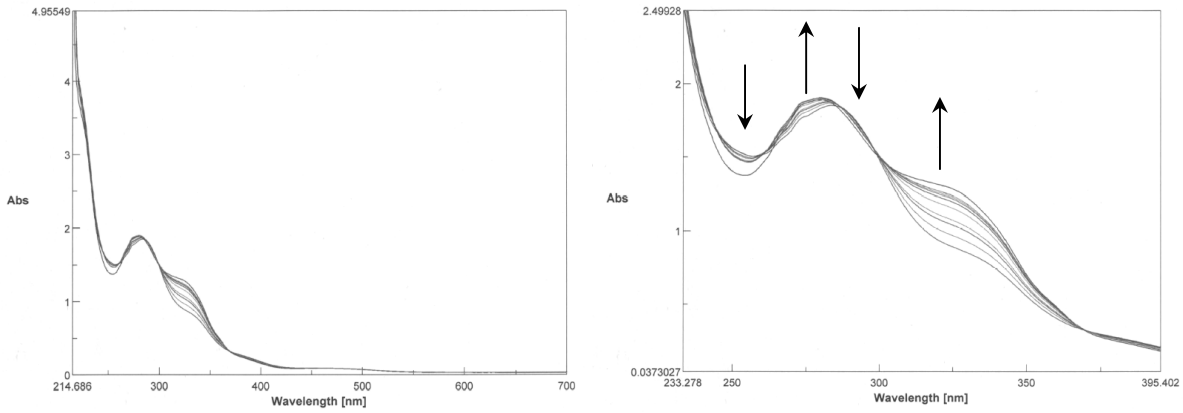

Figure II.39: **a,** Spectral changes of *meso*-**55** at room temperature upon 47 seconds of visible irradiation ($\lambda > 400$ nm). **b,** Enlargement of the region between 225 and 400 nm and spectral behaviour.

This was confirmed by HPLC analysis upon irradiations (figure II.40) that showed the presence of 83 % of the *trans*-isomer, slightly less than the 89 % observed before light exposure.

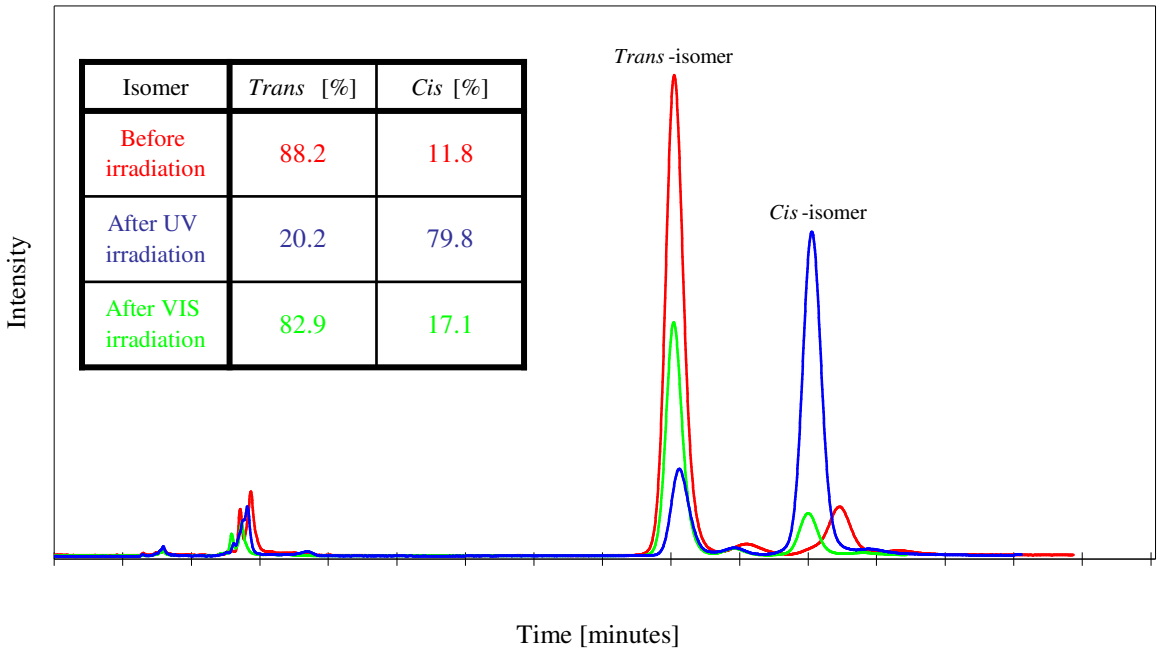

Figure II.40:.*Trans-cis-trans* photoisomerization of diphosphineoxide *meso*-**55** followed by analytical HPLC (Mightysil column; eluent: CH_2Cl_2:EtOH, 97.5:2.5); Red curve, before irradiation; blue curve, 415 seconds of UV (λ = 350 nm) illumination; green curve, 47 seconds visible light irradiation (λ> 400 nm).

Similar analyses were conducted for the two enantiomers of diphosphineoxide **55** and demonstrated similar behaviour (figure II.41-II-44). However, only two isosbestic point were identified on the spectrum for the enantiopure (+)-**55** and (-)-**55**. Sharp isosbestic points at 267 nm and 375 nm were found on the spectrum, for both enantiomers and for both isomerization processes. It suggested that equilibrium was achieved between both species, with no side product formation.

a **b**

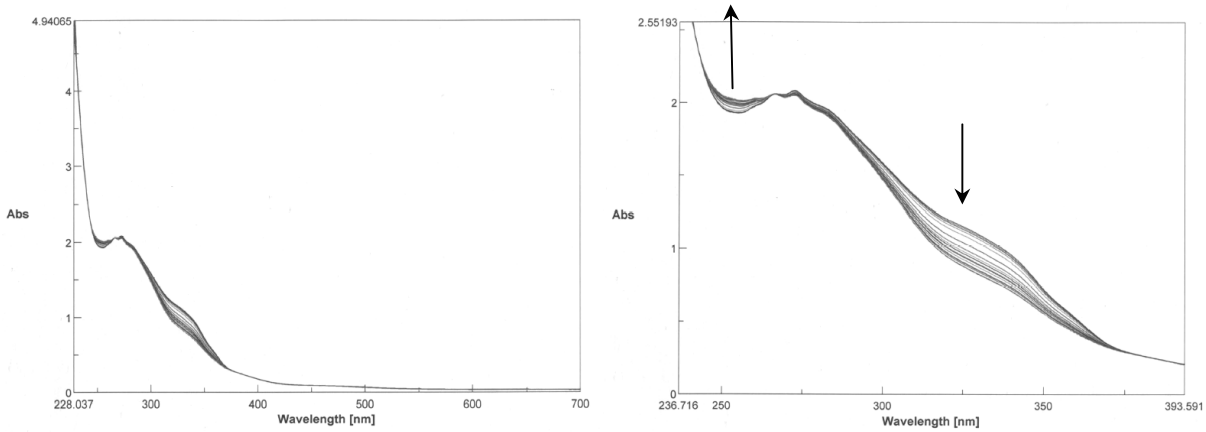

Figure II.41: **a,** Spectral changes of diphosphineoxide (+)-**55** at room temperature upon 205 seconds of UV (λ = 350 nm) irradiation. **b,** Enlargement of the region between 225 and 400 nm and spectral behaviour. Isosbestic points: 267 nm and 375 nm.

a **b**

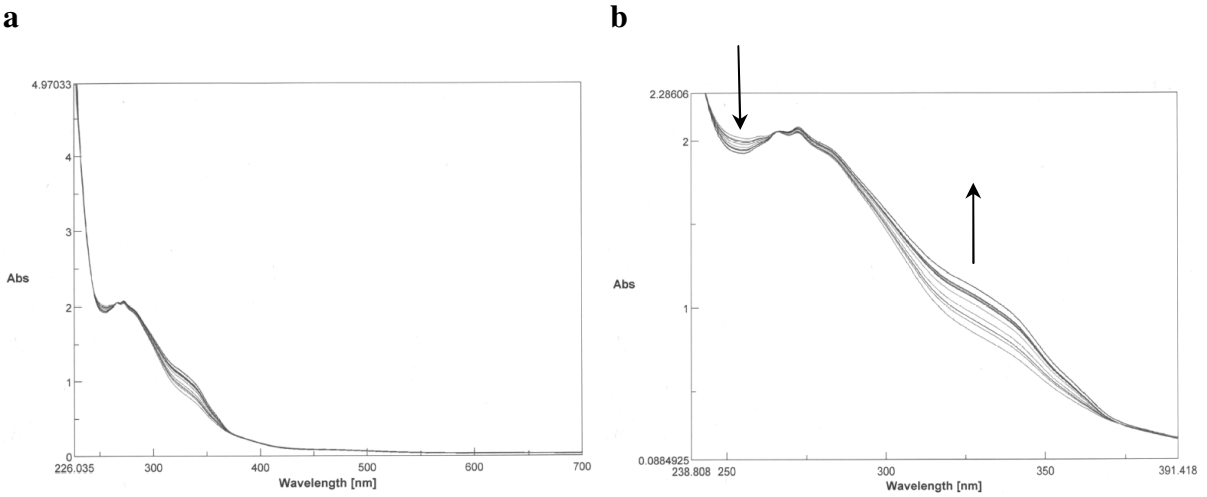

Figure II.42: Spectral changes of diphosphineoxide (+)-**55** at room temperature upon 27 seconds of visible irradiation (λ > 400 nm). **b,** Enlargement of the region between 225 and 400 nm and spectral behaviour. Isosbestic points: 267 nm and 375 nm.

a **b**

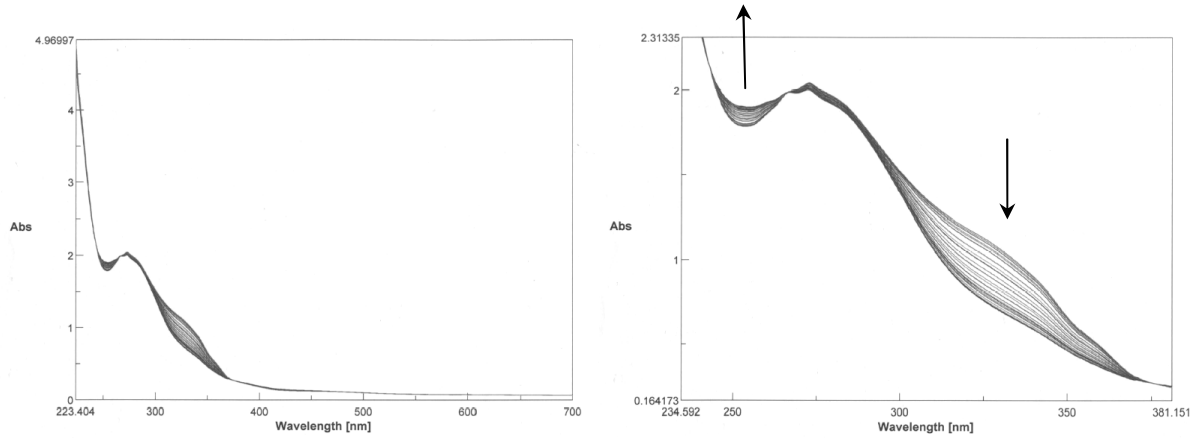

Figure II.43: **a,** Spectral changes of diphosphineoxide (-)-**55** at room temperature upon 320 seconds of UV (λ = 350 nm) irradiation. **b,** Enlargement of the region between 225 and 400 nm and spectral behaviour. Isosbestic points: 266 nm and 375 nm.

a **b**

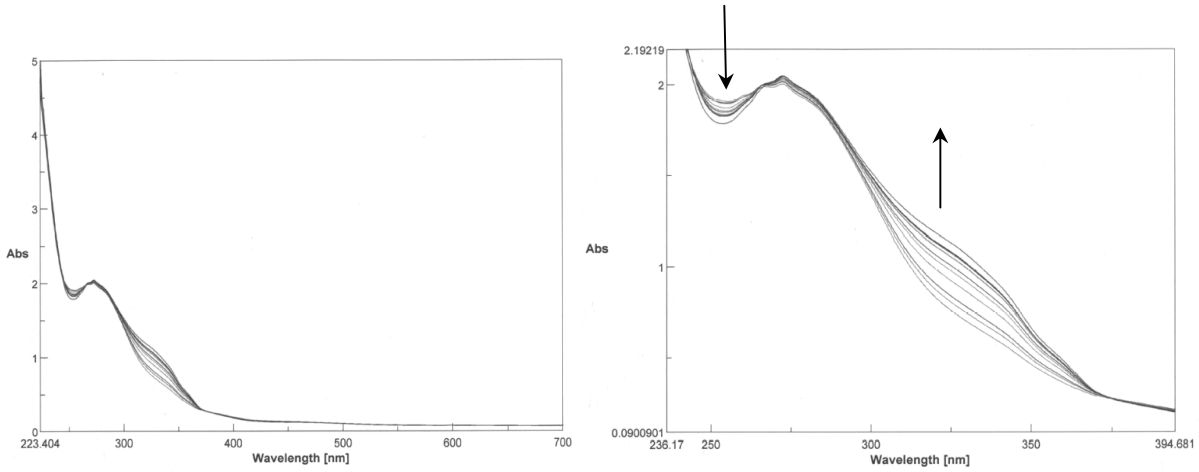

Figure II.44: Spectral changes of diphosphineoxide (-)-**55** at room temperature upon 27 seconds of visible irradiation (λ > 400 nm). **b,** Enlargement of the region between 225 and 400 nm and spectral behaviour. Isosbestic points: 266 nm and 375 nm.

Attempts to isomerize the azobenzene thermally by heating a toluene (100 μM) solution of *meso*-**55** during 12 hours resulted in no absorption spectral changes.

5.9. Reduction of the phosphine oxides

In order to coordinate the ligand to the metastable nickel (II) metal, we first needed to deprotect the diphosphine oxide **55** by reduction with trimethylsilane [112]. This reaction was accompanied by side products **55** and **55a** due to the fast reoxidation of the diphenylphosphine moieties under air (figure II.45).

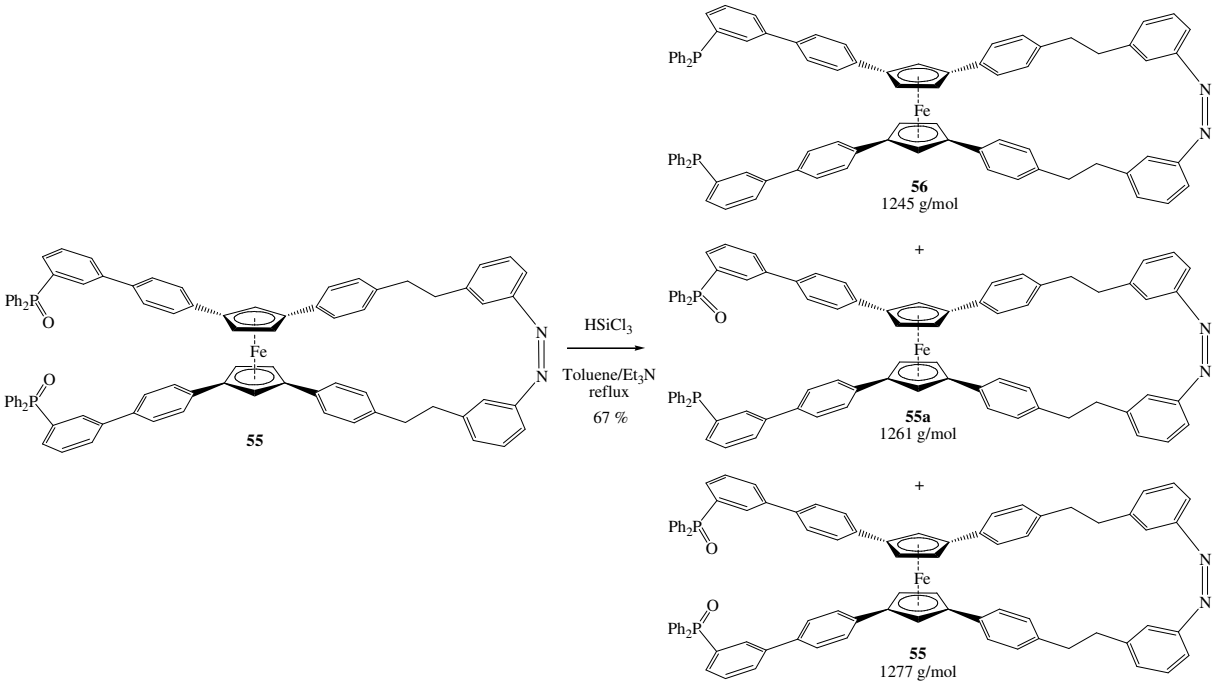

Figure II.45: Deprotection of diphosphineoxide **55** with trimethylsilane affording scissor ligand **56** in 67% yield.

Before reducing the precious diphosphineoxide **55**, we tested the reaction conditions on triphenylphosphine oxide in the presence of azobenzene because we supposed that trichlorosilane might be too harsh for the azo functionality. We found out that in a toluene triethyl amine mixture at reflux, the azo group remained intact while the diphosphine oxide was quantitatively reduced.

Thereafter, we discovered that the treatment of the reaction after the reduction of diphosphineoxide **55**, according to Casy and coworkers with dilute aqueous solutions of $NaHCO_3$ and HCl [112], cleaved the azobenzene moiety (figure II.46).

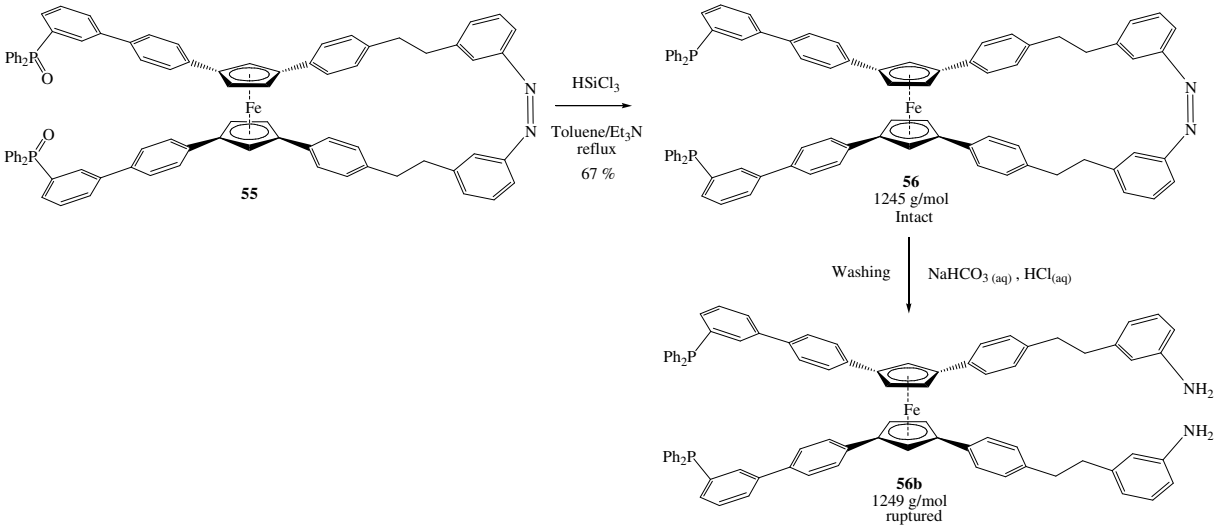

Figure II.46: Effect of the washing on the azobenzene, resulting in a cleavage of the strap.

After washing and column chromatography, the fractions were analyzed by MS (figure II.47), indicating that the major compound was side product **56b** (m/z = 1249.35) with 4 more g/mol than **56** due to the 4 amines protons. Peaks at m/z = 1264.35 and 1281.34, representing respectively the monoxide and dioxide of **56b**, confirmed this rupture of the azobenzene strap, due to reduction of the azobenzene moiety.

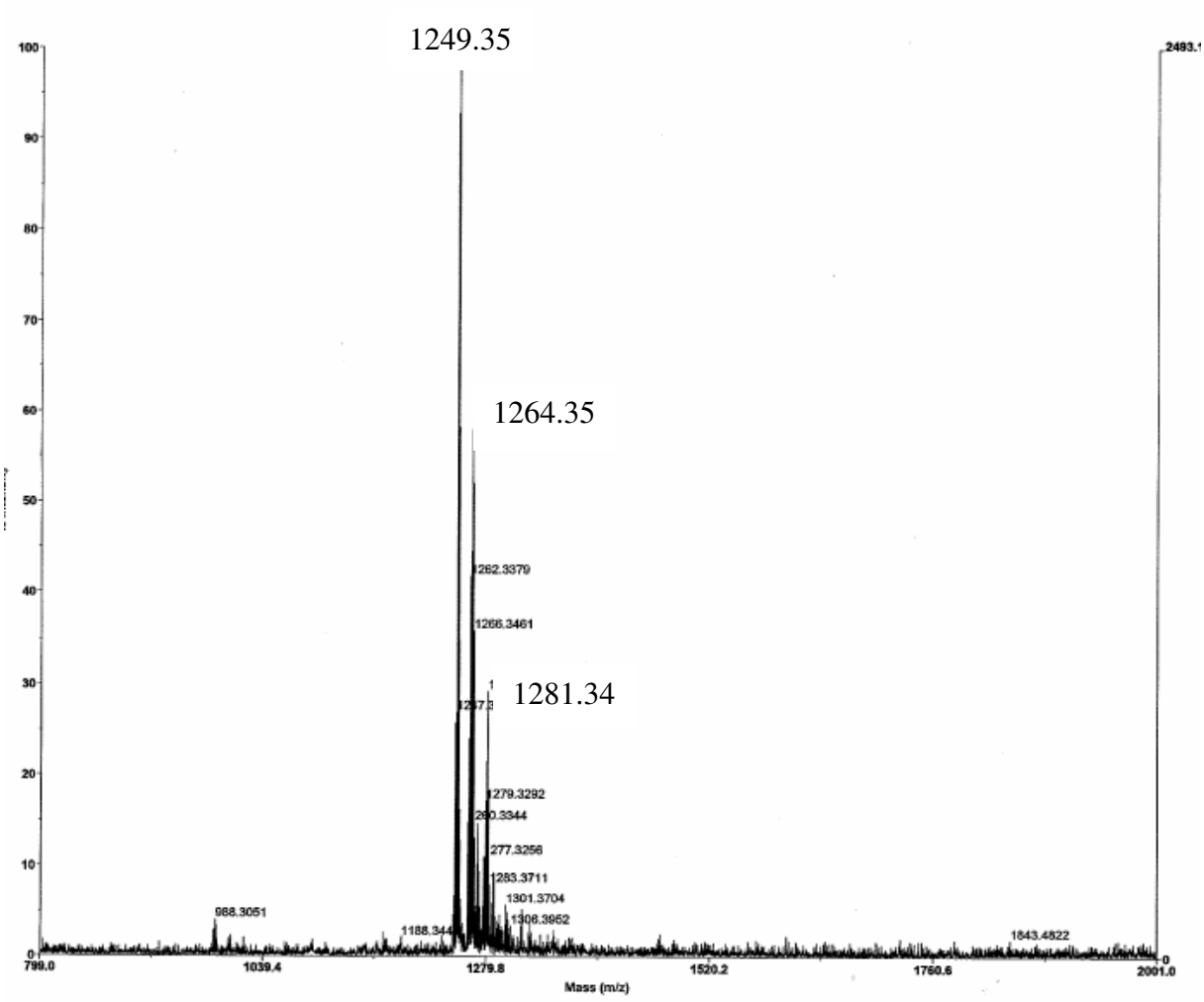

Figure II.47: MALDI-TOF MS spectrum displaying a major peak at m/z = 1249.35 for cleaved **56b** accompanied by peaks for the monoxide and dioxide.

We therefore shifted to another purification procedure and carried out a solid deposit by adding silica directly in the reaction mixture. After removal of the solvent, the product was purified by column chromatography on silica gel under argon. A MALDI-TOF MS analysis displayed a peak at m/z = 1245 (figure II.48) confirming the double reduction to yield diphosphine scissor ligand (+)-**56**. Furthermore, two singlets in ^{31}P NMR around -2.6 ppm attested that the reaction yielded the diphosphine scissor ligand (+)-**56** in majority (figure II.49). These signals were attributed to both *trans*- and *cis*-azobenzene diastereoisomers of

(+)-**56**. Indeed, the phosphorus atoms found themselves in different environments and thus exhibited two signals.

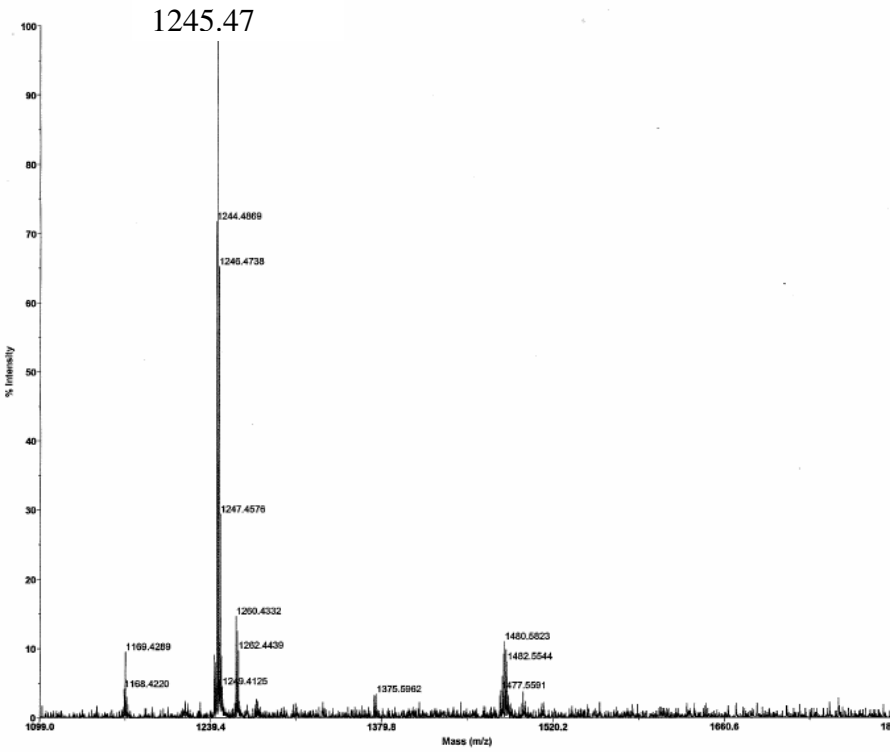

Figure II.48: MALDI-TOF MS spectrum of crude diphosphine bidentate scissor ligand (+)-**56** before washing, displaying a major peak at m/z = 1245.47, $[M]^+$ calculated: 1245.25 ($C_{86}H_{66}FeN_2P_2$).

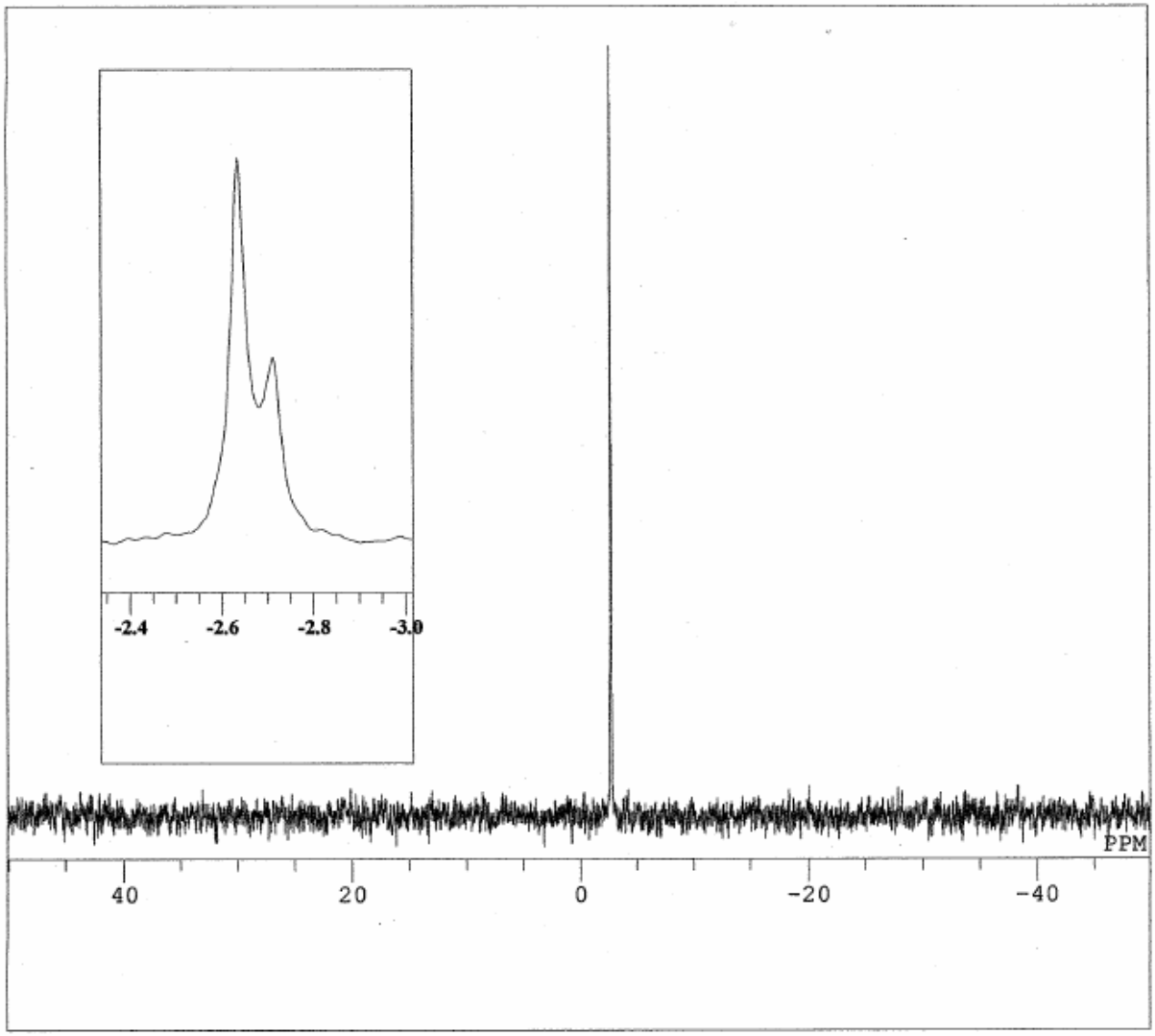

Figure II.49: Phosphorus NMR of diphosphine scissor ligand (+)-**56** displaying two singlets due to the two diastereoisomers.

The deprotected phosphine moieties are air sensitive and oxidise rapidly in solution (1 mM). Indeed, we left a sample of diphosphine scissor ligand (+)-**56** in solution under air and monitored the oxidation by MALDI-TOF MS. As displayed in Figure II.50, the set of peaks represent the three states of the phosphines: Free (1245 g/mol), monoxide (1261 g/mol) and dioxide (1277 g/mol). The oxidation proceeded rapidly and was almost completed within 8 hours.

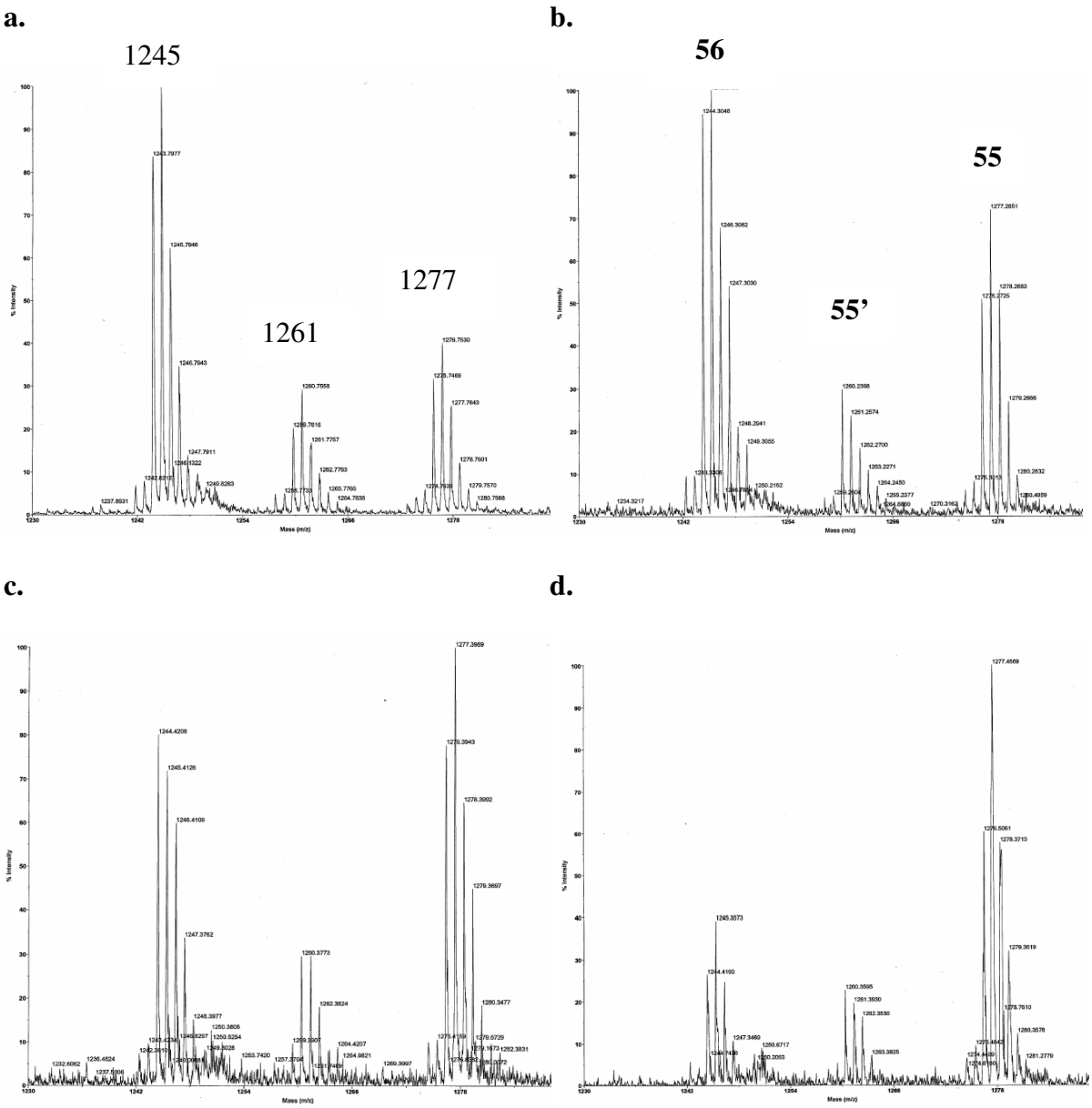

Figure II.50: MALDI-TOF MS showing the behaviour of diphosphine scissor ligand (+)-**56** left under air in CH_2Cl_2 solution; left set of peaks (m/z = 1245), diphosphine; middle set (m/z = 1261), monophosphine; right set, diphosphine oxide (m/z = 1277). **a**, left under air one hour; **b**, two hours; **c**, 4 hours; **d**, 8 hours.

6. Coordination properties of diphosphine scissors ligand 56 with d^8 metal ions.

6.1. Rhodium (I) complexation with diphosphine scissor ligand 56 and behaviour upon light irradiations.

A structure correlation was performed on all *cis*-$[Rh(CO)_2(PR_3)_2]^+$ complexes reported in the Cambridge Structural Database (August 2008). The diphosphine bite angle of each complex was plotted as a function of the dihedral angle between the plane of the diphosphines and the plane from the two carbon monoxides. Only three *cis*-$[Rh(CO)_2(PR_3)_2]^+$ complexes were found and all adopted a square planar geometry (figure II.51). One of which, a bis-diphenylphosphine ferrocene $[Rh(CO)_2(dppf)]^+$ rhodium complex that closely resembles our system [115]. As second row transition metal with large d orbital splitting, rhodium (I) was used as an archetype for square planar complexes.

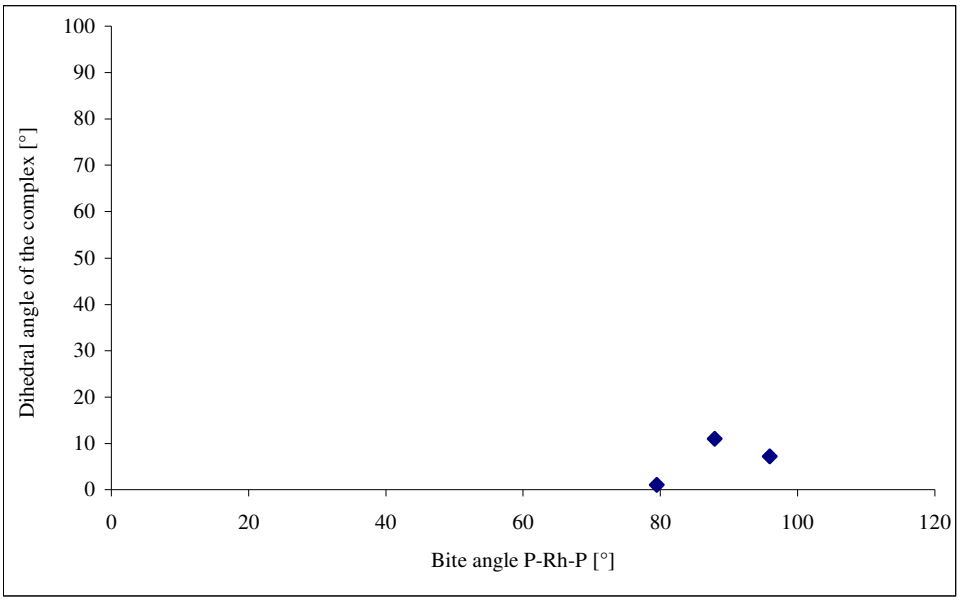

Figure II.51: Plot of the dihedral angle between the plane of the diphosphines and the plane of the carbon monoxide as a function of the bite angle of the diphosphine in $[R_3P^{\frown}PR_3Rh(CO)_2]^+$ deposited in the Cambridge Structural Database (August 2008).

In order to familiarize ourselves with the complexation properties of diphosphine chelating ligand **56** towards square planar geometry, we reacted $[RhCl(CO)_2]_2$ with 2 equivalents of the enantiopure diphosphine (+)-**56** (figure II.52).

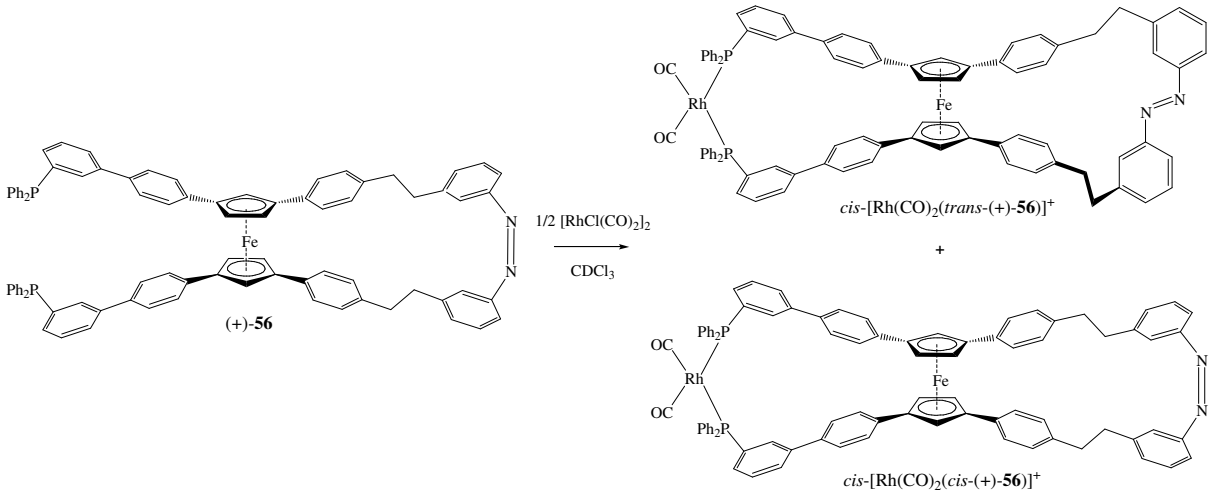

Figure II.52: Complexation of chelating enantiomer (+)-**56** with rhodium (I) in deuterated chloroform.

The reaction was performed in $CDCl_3$ in an NMR tube under argon at room temperature and the progress of the reaction monitored by phosphorus NMR. The first spectrum recorded after one hour exhibited four doublets (29.05 ppm, ^{1}J Rh-P: 123 Hz; 31.99 ppm, ^{1}J Rh-P: 125 Hz; 48.06 ppm, ^{1}J Rh-P: 177 Hz; 51.27 ppm, ^{1}J Rh-P: 177 Hz). These signals are presumably due to the presence of *cis*- and *trans*- configurations of the azobenzene and around the rhodium center affording 4 different species: *trans*-$[Rh(CO)_2$(*trans*-(+)-**56**)$]^+$, *trans*-$[Rh(CO)_2$(*cis*-**56**)$]^+$, *cis*-$[Rh(CO)_2$(*trans*-(+)-**56**)$]^+$ and *cis*-$[Rh(CO)_2$(*cis*-(+)-**56**)$]^+$ respectively. Only the two lower field doublets centered at 48.06 and 51.27 ppm, with a *trans* percentage of 88.1%, remained after 12 hours of reaction (figure II.53). This ratio is similar to the ratio measured by HPLC for the diphosphineoxide *meso*-**55** (figure II.40). We hypothesized that *cis*-$[Rh(CO)_2$(*trans*-

(+)-**56**)] and *cis*-[Rh(CO)$_2$(*cis*-(+)-**56**)]$^+$ were thermodynamically favoured and thus explained the disappearance of the two other doublets. The absorption spectrum of *cis*-[Rh(CO)$_2$((+)-**56**)]$^+$ diverged distinctly from the spectrum of the free ligand (+)-**56** as depicted in figure II.54.

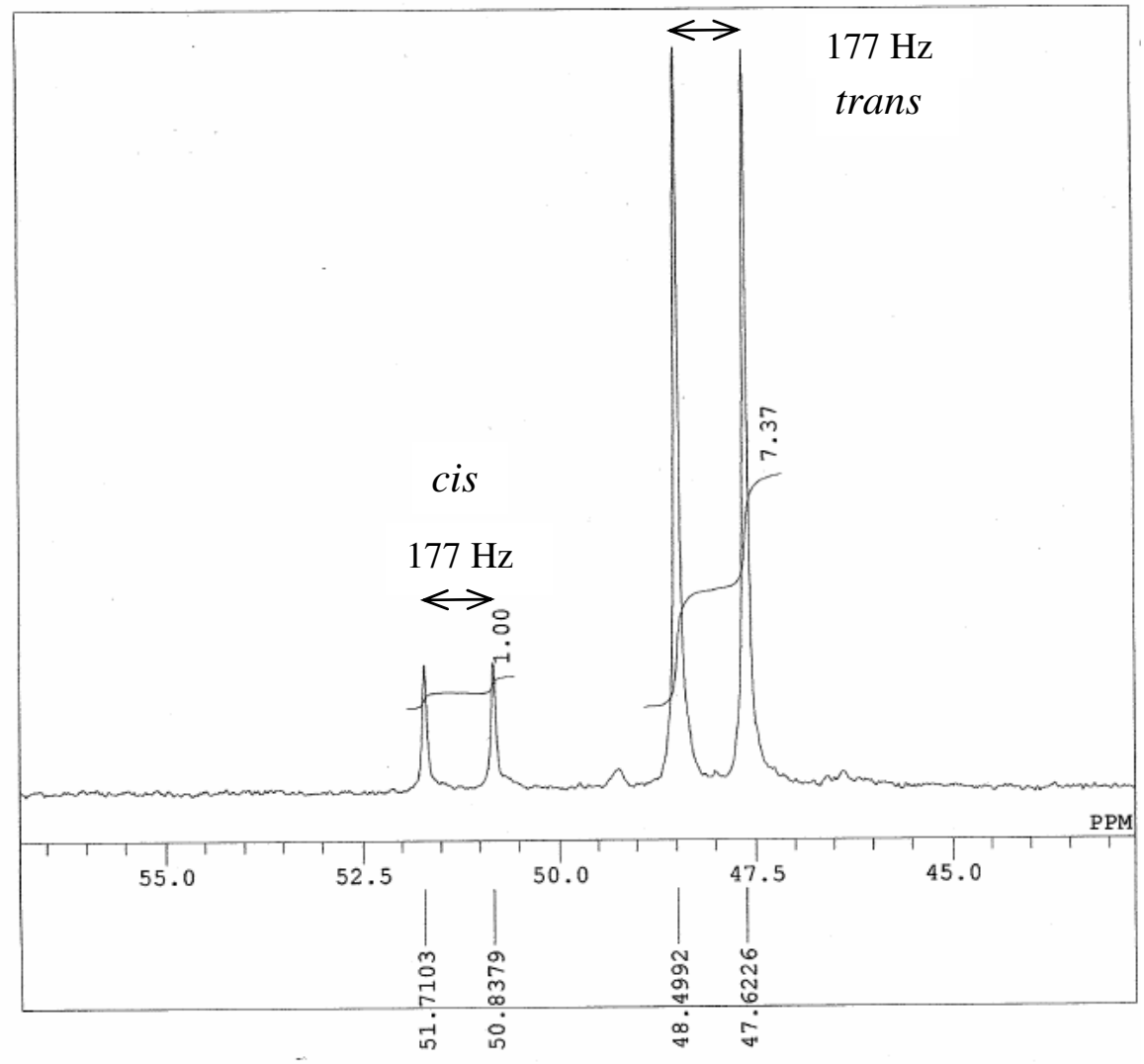

Figure II.53: ^{31}P NMR spectrum of *cis*-[Rh(CO)$_2$(*trans*-**56**)]$^+$ and *cis*-[Rh(CO)$_2$(*cis*-**56**)]$^+$ centered at respectively 48.06 and 51.27 ppm with a *cis*:*trans* ratio of 11.9:88.1; ^{1}J Rh-P = 177 Hz.

Upon UV irradiation (350 nm), a degassed CH_2Cl_2 solution of *cis*-[Rh(CO)$_2$((+)-**56**)]$^+$ (100 µM) did not exhibit any changes in the UV-vis spectrum after 90 seconds, indicating that no *cis* to *trans* photoisomerization occurred.

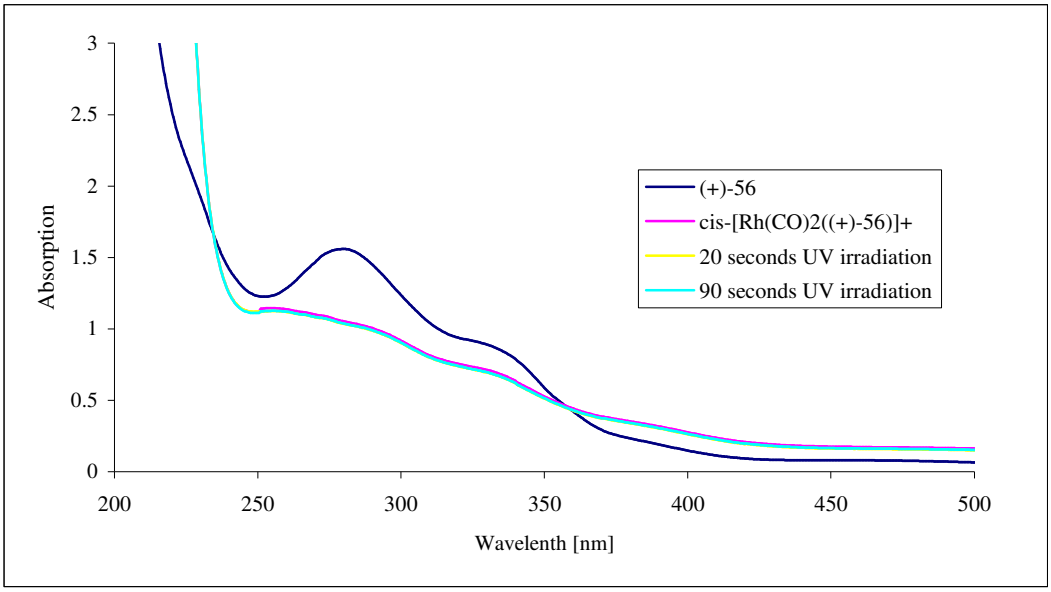

Figure II.54: Behaviour of the UV-Vis spectrum of ligand (+)-**56** upon complexation with rhodium (I) and after UV light irradiation; blue curve, (+)-**56**; pink, *cis*-[Rh(CO)$_2$((+)-**56**)]$^+$; yellow, after 20 seconds of UV irradiation, cyan, after 90 s.

Complexation of diphosphine scissor ligand *meso*-**56** with rhodium was performed similarly to the procedure described above with an enantiomer (+)-**56**. Phosphorus NMR, measured after 12 hours of reaction, revealed two doublets (46.23 ppm, ^{1}J Rh-P: 177 Hz; 46.54 ppm, ^{1}J Rh-P: 178 Hz) that slightly overlapped, representing both *cis*-[Rh(CO)$_2$(*trans-meso*-**56**)]$^+$ and *cis*-[Rh(CO)$_2$(*cis-meso*-**56**)]$^+$, respectively. Unfortunately, the *cis*:*trans* ratio could not be determined precisely because of the overlapping signals (figure II.55).

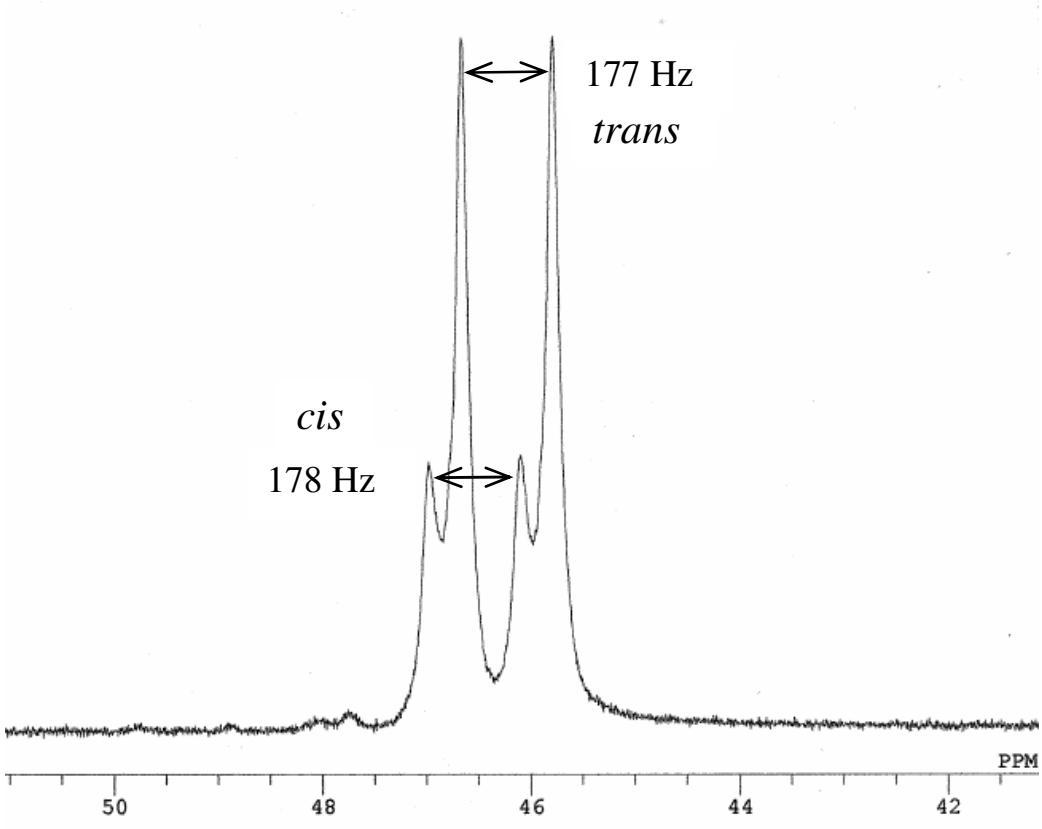

Figure II.55: ^{31}P NMR spectrum of *cis*-[Rh(CO)$_2$(*trans-meso*-**56**)]$^+$ and *cis*-[Rh(CO)$_2$(*cis-meso*-**56**)]$^+$ centered at respectively 46.23 and 46.54 ppm with ^{1}J Rh-P of 177 and 178 Hz.

We hypothesized, according to the overlapping of the ^{31}P NMR doublets, that the configurations of the scissor blades in *cis*-[Rh(CO)$_2$(*trans-meso*-**56**)]$^+$ and *cis*-[Rh(CO)$_2$(*cis-meso*-**56**)]$^+$ are relatively similar. On the other hand and in strong contrast, the doublets of *cis*-[Rh(CO)$_2$((+)-**56**)]$^+$ were apart, suggesting bigger differences in geometry between the two diastereoisomers in the complex.

The *trans-cis* photoisomerization of the *meso*-ligand bound to rhodium (I) was investigated next. We consequently irradiated a CH_2Cl_2 solution (100 μM) of *cis*-[Rh(CO)$_2$(*meso*-**56**)]$^+$ at 350 nm and monitored the progress of the photochemical isomerization by UV-vis

spectroscopy. It was accompanied by changes in the absorption spectrum between 250 and 410 nm (figure II.56).

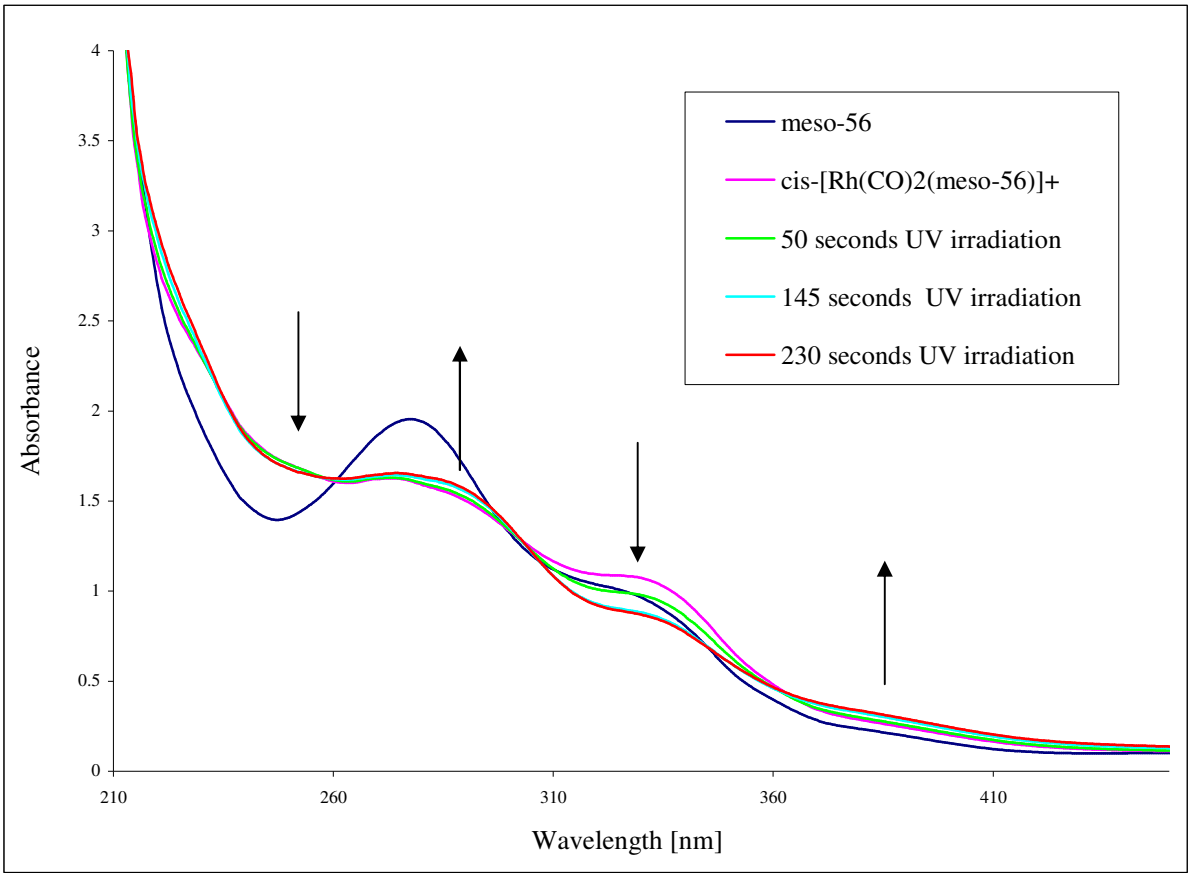

Figure II.56: Behaviour of the UV-vis spectrum of *cis*-[Rh(CO)$_2$(*meso*-**56**)]$^+$ upon complexation and UV light irradiation (350 nm); blue curve, *meso*-**56**; pink, *cis*-[Rh(CO)$_2$(*meso*-**56**)]$^+$; green, after 50 seconds of UV irradiation, cyan, 145 s; red, 230 s.

The presence of isosbestic points at 241, 263, 298 and 361 nm suggested that the photoisomerization occurred intramolecularly and that no side products were formed. We thus speculated that UV irradiation induced a *trans* to *cis* isomerization yielding mainly the *cis*-[Rh(CO)$_2$(*cis-meso*-**56**)]$^+$. Backward photoisomerization with visible light ($\lambda > 400$ nm) on the same sample from *cis*-[Rh(CO)$_2$(*cis-meso*-**56**)]$^+$ to *cis*-[Rh(CO)$_2$(*trans-meso*-**56**)]$^+$

provoked no change in the absorption spectrum, even after 400 seconds of irradiation. We hypothesized that the stability of the *cis*-[$Rh(CO)_2$(*cis-meso*-**56**)]$^+$ prevented the inverse photochemical isomerization of the azobenzene.

Regrettably, the photoisomerization were only possible at very low concentrations and could only be followed by means of UV-vis spectroscopy. All attempts to monitor and subsequently analyze the photoisomerization products by NMR spectroscopy were unfruitful. Unfortunately, no signal corresponding to the molecular weight of either *cis*-[$Rh(CO)_2$((+)-**56**)]$^+$ or *cis*-[$Rh(CO)_2$(*meso*-**56**)]$^+$ could be detected by MALDI TOF MS.

To conclude, we compare the dissimilar behaviour of (±)-**56** and *meso*-**56** complexes, due to their various configurations. We determined that both enantiomers (±)-**56** and *meso*-**56,** and both their *cis* and *trans* diastereoisomers, were able to coordinate to square planar d^8 rhodium (I). However, *cis*-[$Rh(CO)_2$(*trans*-(+)-**56**)]$^+$ complex was favoured and did not switch to *cis*-[$Rh(CO)_2$(*cis*-(+)-**56**)]$^+$ upon UV irradiation whereas *meso*-**56** rhodium (I) complex was photoisomerized. In the ^{31}P NMR spectrum of *meso*-**56** rhodium complex, the doublets due to both diastereoisomers almost overlapped whereas, the doublets were better resolved for the (+)-**56** complex. Based on these observations, we speculated that the phosphine bite angle in *cis*-[$Rh(CO)_2$((+)-**56**)]$^+$ was larger than that of *cis*-[$Rh(CO)_2$(*meso*-**56**)]$^+$, due to the different configurations of the ligands. We also hypothesized that larger bite angle in enantiopure ligand (+)-**56** prevented the photoisomerization upon UV irradiations (350 nm).

6.2. Ligand (+)-56 in catalytical asymmetric hydrogenation.

We next tested diphosphine scissor ligand (+)-**56**, as a mixture of its *trans* and *cis* diastereoisomers, in asymmetric catalytic hydrogenation of various prochiral substrates and

catalyzed by rhodium. For this purpose, we reacted $[Rh(COD)_2]^+BF_4^-$ and bidentate ligand (+)-**56** (1 mol%) with each prochiral substrates **57**, **58**, **59** and **60** in degassed CH_2Cl_2 under 5 bars of hydrogen (figure II.57). All four catalyses were prepared in a glove box under N_2 atmosphere.

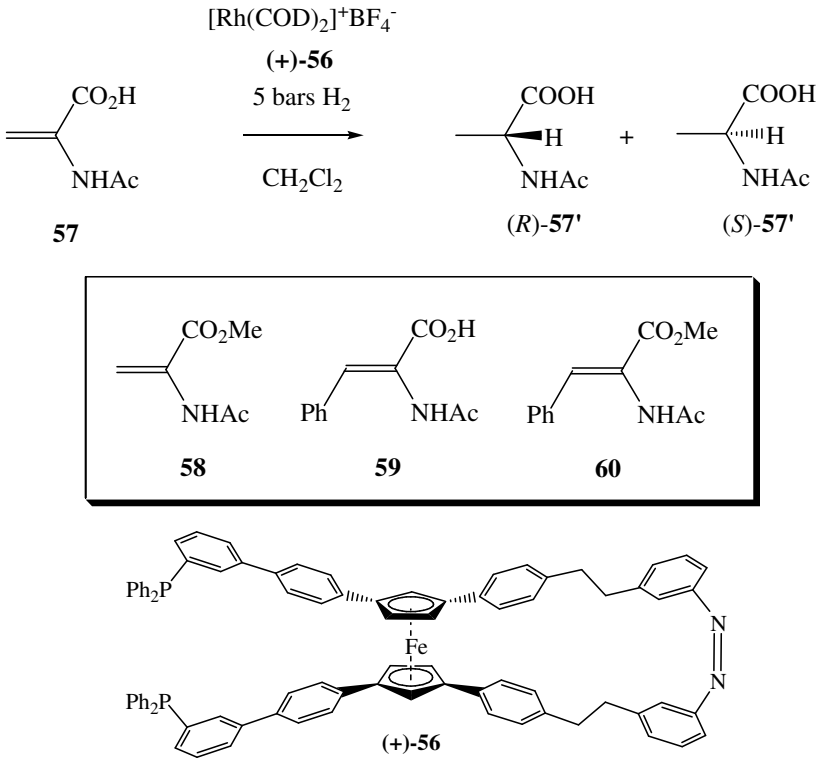

Figure II.57: Enantioselective hydrogenation of various prochiral substrates catalyzed by $[Rh(COD)((+)\text{-}\mathbf{56})]^+$.

After 12 hours of reaction, the four substrates were extracted with methanol. For better detection by gas chromatography (GC), acrylic acid **57'** and cinamic acid **59'** were esterified stoichiometrically by trimethylsulfonium hydroxide in methanol. After injection in the gas chromatograph, the enantiomeric excesses and the conversion percentages were calculated with the help of the integrals. The results of these catalyses are summarized in table II.1.

Under the same conditions, similar catalyses were carried out by replacing diphosphine scissor ligand (+)-**56** with (*S*)-BINAP, a reference ligand for asymmetric hydrogenation (table II.1).

	Catalysis with ligand (+)-**56**		Catalysis with (*S*)-BINAP	
substrate	*ee* in favour of (*R*)-product [%]	Conversion [%]	*ee* in favour of (*R*)-product [%]	Conversion [%]
57	18	38	53	100
58	0	100	7	100
59	4	75	42	100
60	0	73	33	100

Table II.1: Enantiomeric excess and conversions percentages for the asymmetric catalytic hydrogenation of acrylic and cinnamic substrates.

We concluded that the use of diphosphine scissor ligand (+)-**56** in catalytic hydrogenation results in very small enantiomeric excesses in comparison to the results obtained with the (*S*)-BINAP rhodium complex.

6.3. Nickel (II) complexation with diphosphine scissor ligand 56, behaviour upon titration and irradiation.

Various nickel dichloride as well as synthetic procedures have been used in the past for the preparation of *cis*-$[NiCl_2(PR_3)_2]$-type complexes [94, 98, 113, 114]. In most cases, the complexes were synthesized in ethanol or methanol solutions. As diphosphine scissor ligand

56 was only sparingly soluble in ethanol, large quantities of solvent were necessary. In order to study the coordination properties of diphosphine scissor ligand **56**, we used the commercially available bis-diphenylphosphine ferrocene as a model. From these studies, we identified [$NiCl_2$(DME)] [116], whose solubility in dimethoxyethane (DME) is good, as the most suitable starting material for complexation with diphosphine scissor ligand **56**.

A DME solution of [$NiCl_2$(DME)] was reacted with one equivalent of bidentate diphosphine ligand *meso*-**56** (figure II.58) in a highly diluted ethanol solution, and the mixture was subsequently heated to 80°C for 12 hours.

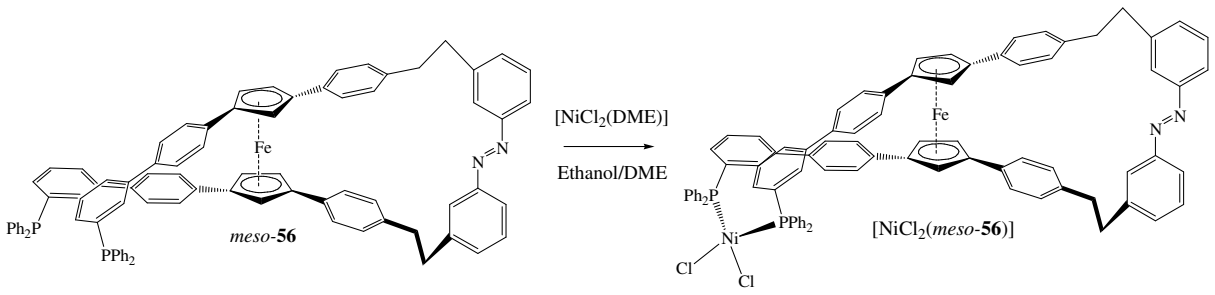

Figure II.58: Complexation of *meso*-**56** with [$NiCl_2$(DME)] affording the *cis*-[$NiCl_2$(*meso*-**56**)] complex.

a

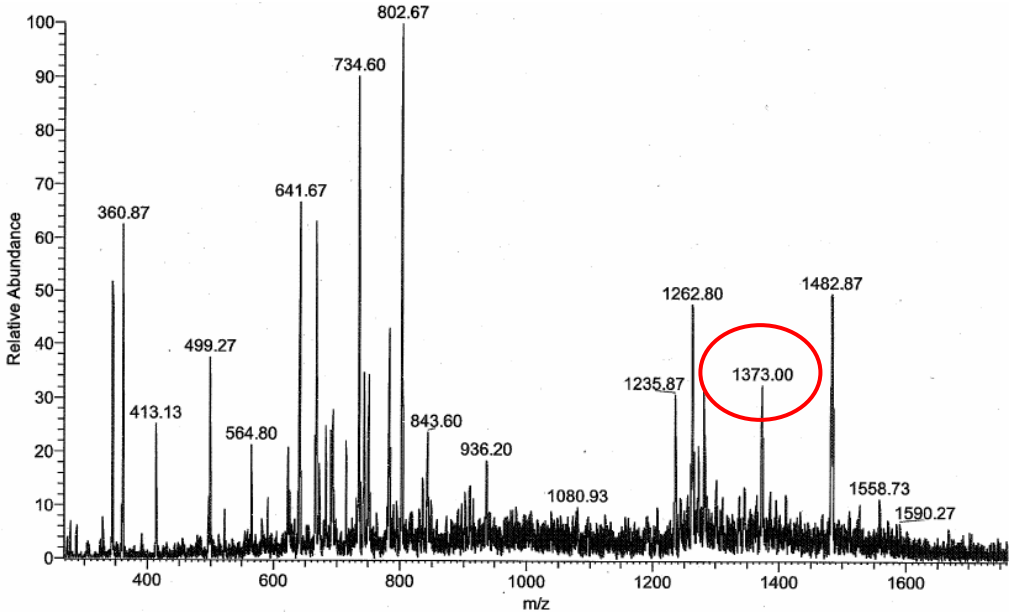

b

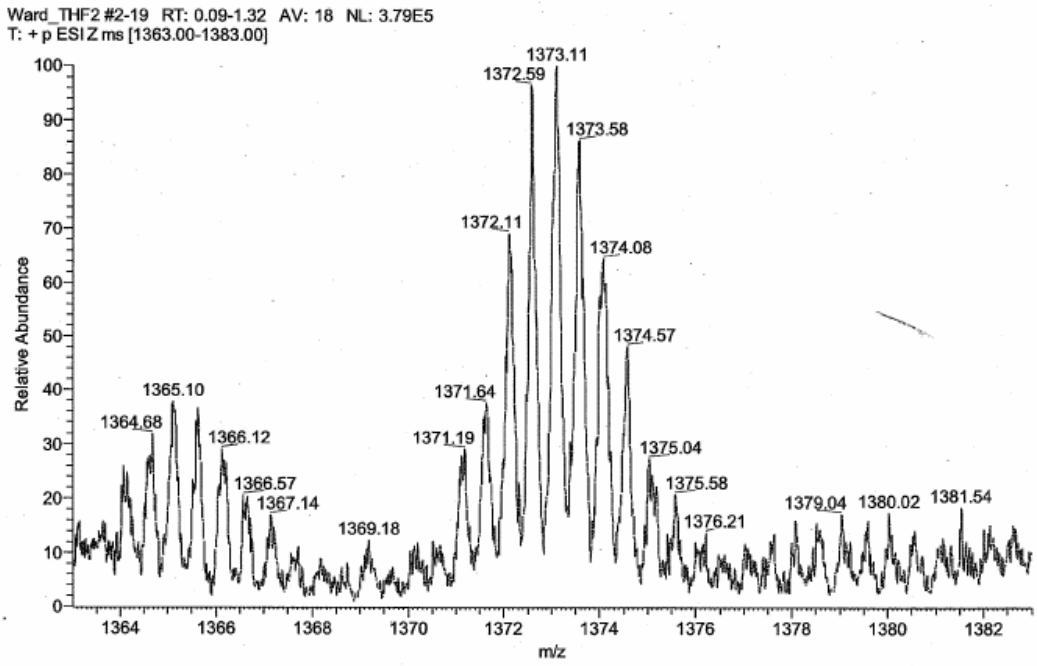

Figure II.59: **a.** SIM ESI MS spectrum of complex *cis*-[$NiCl_2$(*meso*-**56**)] (calculated: 1374.35 g/mol, $C_{86}H_{66}Cl_2FeN_2NiP_2$) displaying the desired nickel (II) molecular switch as a minor product (m/z = 1373.10). **b.** Enlargement of the region of interest displaying the isotopic distribution.

After removal of the solvent, phosphorus and proton NMR analyses yielded no interpretable signals suggesting that the phosphine donors were coordinated to a paramagnetic nickel (II) center forming a *cis*-[$NiCl_2$(*meso*-**56**)] complex. As for *cis*-[$Rh(CO)_2$(**56**)]$^+$ (m/z = 1411), MALDI TOF MS analysis failed to yield a signal corresponding to the molecular weight of *cis*-[$NiCl_2$(*meso*-**56**)]. However, a small signal corresponding to *cis*-[$NiCl_2$(*meso*-**56**)] (m/z = 1374) was identified by selected ion monitoring electro spray ionization SIM ESI MS (figure II.59). Unfortunately, the isotopic distribution did not correlate exactly with a simulation of the isotopic pattern for $C_{86}H_{66}Cl_2FeN_2NiP_2$ as depicted in figure II.60.

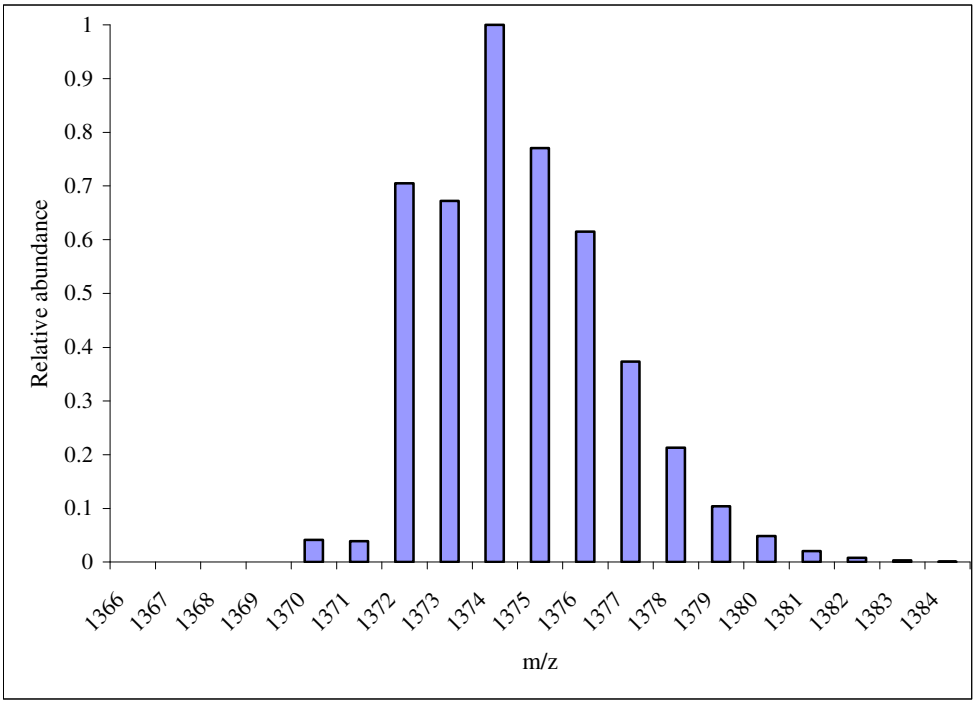

Figure II.60: Calculated simulation of the isotopic pattern for $C_{86}H_{66}Cl_2FeN_2NiP_2$

The same procedures were performed for the formation of *cis*-[$NiCl_2$(**56**)] with enantiopure diphosphine scissor ligand (+)-**56** and (-)-**56**.

Next, we monitored the formation of *cis*-[$NiCl_2$((-)-**56**)] by CD spectroscopy. For this purpose, aliquots of (-)-**56** were added to *cis*-[$NiCl_2$(DME)] in DME (160 µM). The resulting solutions were heated for 1 hour at 40° before CD analysis. Unfortunately and as observed (figure II.61) for the free phosphine ligand (-)-**56**, the CD signal saturated at wavelengths below 330 nm.

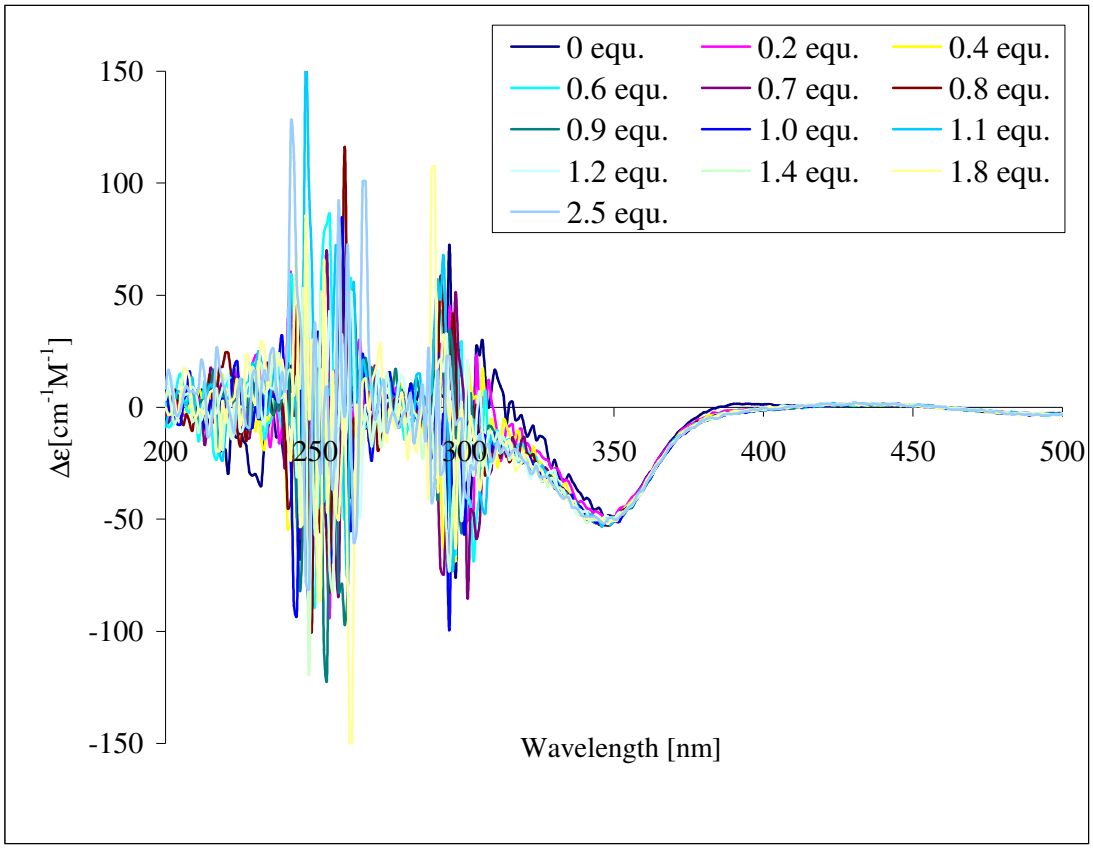

Figure II.61: Titration of diphosphine scissor ligand (-)-**56** with [$NiCl_2$(DME)].

Trans-cis photoisomerization of *cis*-[$NiCl_2$(*trans-meso*-**56**)] in dichloromethane (100 µM) was studied next by absorption spectroscopy upon UV irradiation (350 nm). As displayed in figure II.62, the band decreased between 300 and 360 nm after irradiation, but no isosbestic points could be detected.

a.

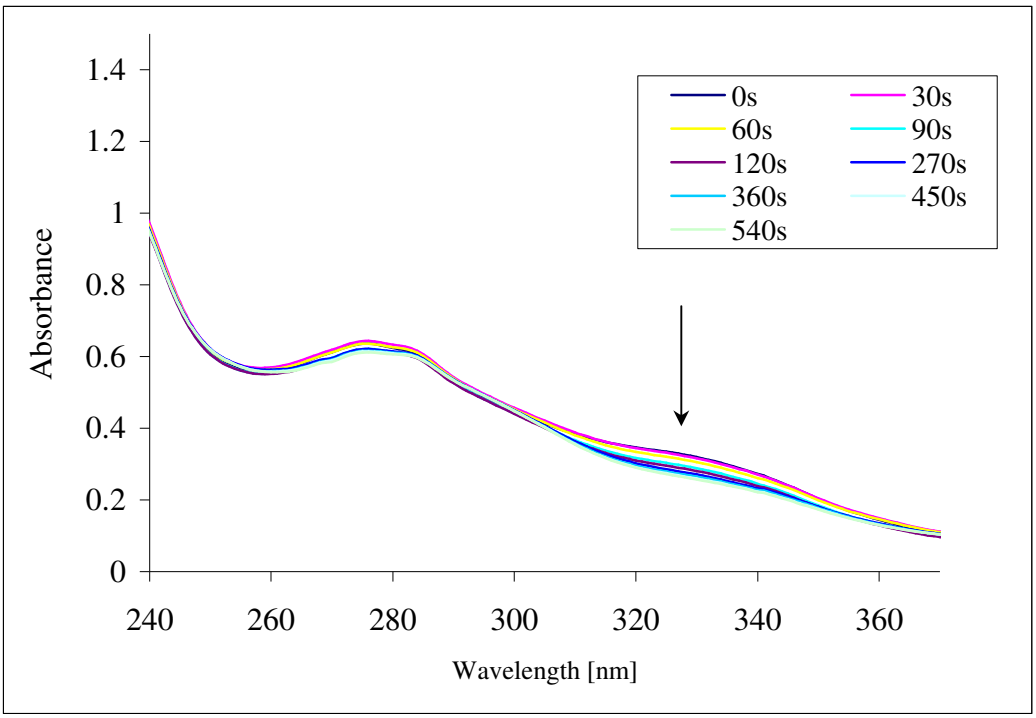

b.

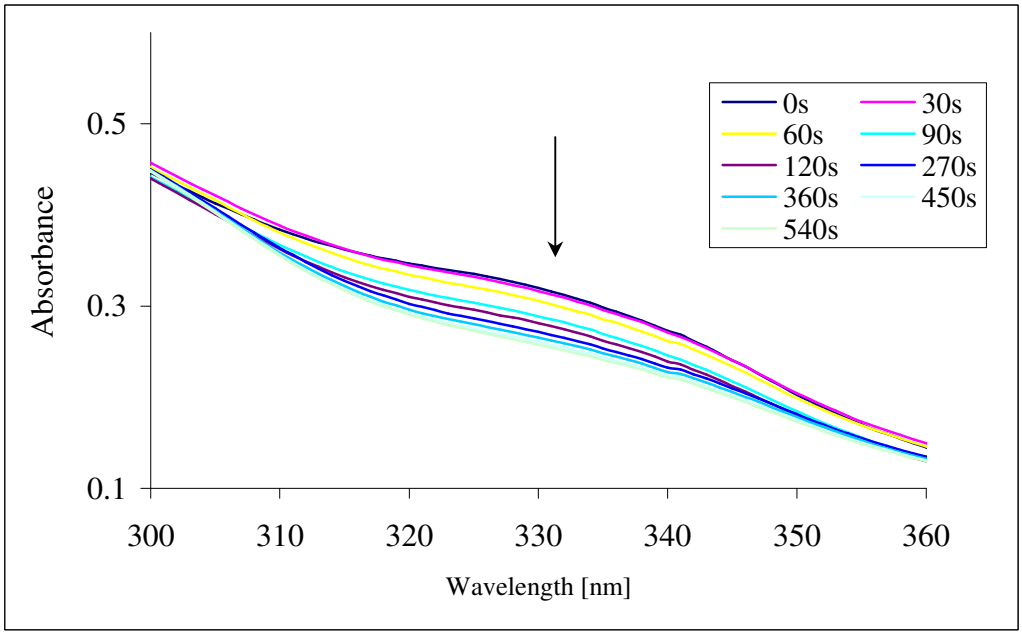

Figure II.62: **a**, Absorbance changes in the spectrum upon photochemical (λ = 350 nm) *trans* to *cis* isomerization in *cis*-[$NiCl_2$(*meso*-**56**)]. **b**, zoom on the active region.

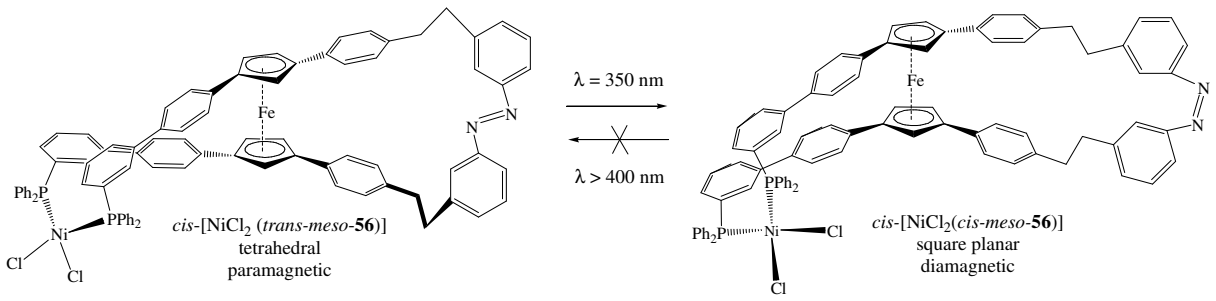

Figure II.63: Photoisomerization of *cis*-[$NiCl_2$(*meso*-**56**)] from *trans* to *cis* isomers of the ligand, inducing a change in geometry and thus in magnetic susceptibility.

On the same solution, reverse *cis* to *trans* isomerization was attempted by visible light ($\lambda >$ 400 nm) irradiation. No significant change in the absorption spectrum upon irradiation could be detected. Again, we speculate that *cis*-[$NiCl_2$(*cis-meso*-**56**)] adopted a thermodynamically favoured square planar geometry thus preventing the *cis* to *trans* photochemical irradiation of the ligand. This is in strong contrast with the visible light irradiation performed on ($\lambda >$ 400 nm) free diphosphine oxide scissor ligand *cis*-**55** (figure II.39), which upon visible irradiation, return back to *trans*-**55**. This suggests that diphosphine scissor ligand *meso*-**56** was indeed coordinated to the nickel center. On the other hand this behaviour correlates with the absence of *cis* to *trans* isomerization observed when *cis*-[$Rh(CO)_2$(*meso*-**56**)]$^+$ was irradiated with visible light (figure II.55).

Similar studies were conducted with *cis*-[$NiCl_2$((+)-**56**)], but no apparent changes in absorption spectrum were identified upon either UV or visible light irradiation. These results confirm the absence of photoisomerization of *cis*-[$Rh(CO)_2$((-)-**56**)]$^+$.

6.4. Behaviour of the magnetic susceptibility of [$NiCl_2$(*meso*-**56**)] upon irradiation

In collaboration with the group of Prof. S. Decurtins (University of Bern), a sample of *cis*-[$NiCl_2$(*trans-meso*-**56**)] was subjected to SQUID magnetometry. The results exhibited an increasing susceptibility on cooling and the $\chi T(T)$ plot shows a constant value around 0.82 $cm^3 \cdot K \cdot mol^{-1}$ down to 150 K, upon which, zero-field splitting caused the value to increase before dropping towards zero (figure II.64).

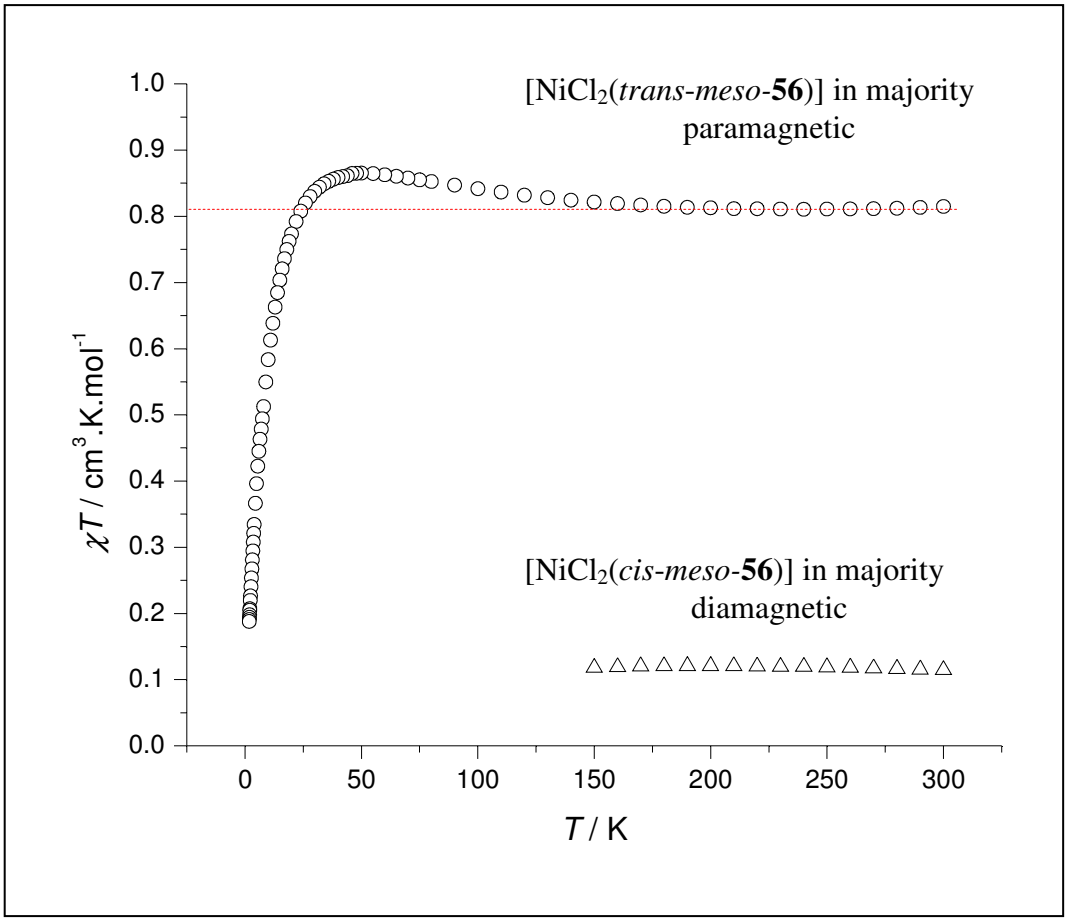

Figure II.64: Magnetic susceptibility behaviour of complex *cis*-[$NiCl_2$(*meso*-**56**)] upon UV irradiation. (o) Before irradiation. (Δ) After 2 hours of UV irradiation at 350 nm.

As the sample was oily even after a long period of drying under vacuum, the g-value could not be derived from the data as the diamagnetic correction for the solvent and exact amount of *cis*-[$NiCl_2$(*meso*-**56**)] were unknown. Subsequently, the sample was dissolved in dichloromethane and irradiated with UV light (λ = 350 nm) during two hours. After evaporation of the solvent, the sample was analyzed by SQUID magnetometry and revealed a $\chi T(T)$ plot between 300-150 K displaying a markedly lower value. This suggested that the sample was mostly in the diamagnetic state and that the ligand in *cis*-[$NiCl_2$(*meso*-**56**)] had photoisomerized from *trans* to *cis*. The same sample was dissolved again in dichloromethane and subjected to visible light (λ > 400 nm) but displayed no magnetic susceptibility change. It showed that the process was irreversible, which is most likely due to the more stable square planar environment of the nickel atom in *cis*-[$NiCl_2$(*cis-meso*-**56**)]. It also confirmed the results obtained by visible light irradiation monitored by absorption of the same complex described above (figure II. 62).

Similar experiments were performed with *cis*-[$NiCl_2$((+)-**56**)] and *cis*-[$NiCl_2$((-)-**56**)] which displayed a similar susceptibility to *cis*-[$NiCl_2$(*meso*-**56**)]. No difference in magnetic susceptibility was identified after irradiation with neither UV (2 hours at 350 nm) nor visible light (2 hours at λ > 400 nm). It confirmed that the complexes composed of the enantiopure diphosphine scissor ligand (+)-**56** and (-)-**56** were unable to isomerize photochemically. Taken together, these data suggested that the larger bite angles in the enantiopure ligand **56**, due to their configuration (figure II.35), precluded the photoisomerization.

7. Conclusions and outlook

All the data gathered suggest that we have created a nickel-based photomagnetic molecular fuse. Insertion of a diphosphine moiety on a bromo scissor yielded a photosensitive ligand which, upon irradiation, changed its configuration and thus its bite angle between the two phosphorus donors. This photoinduced variation of the bite angle could be translated into a magnetic response upon complexation with a $\{NiCl_2\}$ moiety. Despite a thermodynamic preference toward *trans*-azobenzene[34-38], the photochemical isomerization of the ligands, leading to square planar diamagnetic *cis*-[$NiCl_2$(*cis-meso*-**56**)] and *cis*-[$Rh(CO)_2$(*cis-meso*-**56**)]$^+$ occurred irreversibly. As all the complexes composed of enantiopure ligands did not respond to irradiation, we speculated that the diphosphine bite angle in these ligands was too large to be changed. The system thus acted as a molecular fuse and could be a step towards information storage at the molecular level. Our enantiopure ligands (+) and (-)-**56** could lead to light directed enantioselective catalysis, a feat that has never been achieved before. However the photoirradiation at lower dilution should further be studied for this purpose. Complexation to other bistable metal ion could also be conceivable.

- Chapter III -

Materials and methods

This chapter deals with the abbreviations, apparatus, reactants, solvents and utilized techniques. The operating procedures for the synthesis and the analyses carried out in this research are also described.

1. Abbreviations

The significations of each abbreviation used in this thesis are presented below.

°C:	Degree Celsius
Å:	Ångström
AcOEt:	Ethyl Acetate
$AlCl_3$:	Aluminium Chloride
ADP:	Adenosine diphosphate
Ar:	Aromatic (in NMR characterisation)
Ar.:	Argon
ATP:	Adenosine triphosphate
$B(EtO)_3$:	Triethyl borate
n-BuLi:	Buthyllithium
t-BuOK:	Potassium terbutoxyde

$CaCl_2$:	Calcium Chloride
CD:	Circular Dichroism
$CDCl_3$:	Deuterated Chloroform
cGMP:	Cyclic guanosine monophosphate
$CHCl_3$:	Chloroform
CH_2Cl_2:	Dichloromethane
Co.:	Coworkers
COSY:	Correlation spectroscopy
Cp:	Cyclopentadien
Cs_2CO_3:	Cesium carbonate
CuCl:	Copper Chloride
CuI:	Copper iodine
DEPT:	Distortionless enhancement by polarization transfer
DME:	Dimethoxyethane
DMSO-d_6:	Deuterated dimethyl sulfoxyde
dpp:	Diphenyl phenanthroline
EtOH:	Ethanol
ESI:	Electrospray ionization
$FeCl_3$:	Iron chloride
FliC:	Flagelin
g:	gram
GPC:	Gel permeation chromatography
h:	hour
H_2:	Hydrogen
HETCOR:	Heteronuclear correlation spectroscopy
H_2SO_4:	Sulfuric acid
HOMO:	Highest occupied molecular orbital
HPLC:	High pressure liquid chromatography
HS:	High spin
Hz:	Herz
KSCN:	Potassiun thiocyanate
Liesst:	Light-induced excited spin state trapping
LS:	Low spin
LUMO:	Lowest unoccupied molecular orbital

M:	Molar (mol/liter)
MALDI:	Matrix-assisted laser desorption/ionisation
$MgSO_4$:	Magnesium sulfate
MHz:	Mega Hertz
min.:	Minute
ml:	Milliliter
mm:	Millimeter
mmol:	Millimol
µmol:	Micromol
MS:	Mass spectroscopy
N_2:	Nitrogen
NaCl:	Sodium chloride
$NaHCO_3$:	Sodium hydrogenocarbonate
Na_2SO_3:	Sodium sulfite
Na_2SO_4:	Sodium sulfate
NH_4Cl:	Ammonium chloride
nm:	Nanometer
NMR:	Nuclear magnetic resonance
NOESY:	Nuclear overhauser effect spectroscopy
O_2:	Oxygen
pap:	Phenylazopyridine
$Pd(PPh_3)_4$:	Tetrakis(triphenylphosphine) palladium
$Pd(PPh_3)_2Cl_2$:	Dichloro-(bistriphenylphosphine) palladium
PET:	Photoinduced electron transfer
P_2O_5:	Phosphorus pentoxide
ppm:	Parts per million
ps:	Picosecond
PtO_2:	Platinum dioxide
RNA:	Ribonucleic acid
SIM:	Selective ion-monitoring
SQUID:	Supraconducting quantum interferences devices
terpy:	Terpyridine
THF:	Tetrahydrofurane
TMS:	Trimethylsilane

TOF:	Time of flight
UV:	Ultraviolet
Vis:	Visible
W:	Watt

2. Solvents and reactants

The degree of purity and the provenance of the reactants and the solvents are presented in the following table.

Product	Origin	Degree of purity
Acetonitrile	Across	≥ 99.9 %
$AlCl_3$	Fluka	99 %
Benzene	Riedel de Haen	99.5 %
Benzophenon	Fluka	99 %
Bromobenzene	Across	99 %
n-BuLi	Across, 1.6 M in hexane	
t-BuOK	Fluka	≥ 97 %
$CaCl_2$ (dehydrated)	Fluka	≥ 97 %
Celite	Fluka, 545, 10-60 Å	
Chlorodiphenylphosphine	Across	98 %
Chloroform	VWR, Prolabo	98 %
Cs_2CO_3	Aldrich	≥ 99 %
CuCl	Fluka	≥ 97 %

CuI	Across	98 %
1,2-Dibromobenzene	Across	97 %
Dichloromethane	Reactolab	technical
Dichloromethane (HPLC)	Fluka	≥ 99.9 % (GC)
1,2-Dimethoxyethane	Fluka	(under molecular sieve)
Ethanol (synthesis)	Merck	≥ 99.9 %
Ethanol (work up)	Reactolab	technical
Ethanol (HPLC)	Fluka	≥ 99.8 % (GC)
Ethylacetate	reactolab	technical
3-Ethynylaniline	Aldrich	≥ 98 %
$FeCl_3$	Fluka	≥ 97 %
$FeCl_3 \cdot 6\ H_2O$	Aldrich	97 %
Hexane	Reactolab	technical
H_2SO_4	Reactolab	96 %
Iodine	Across	99.8 %
p-Iodoacetophenon	Across	98 %
KSCN	Fluka	98 %
$MgSO_4$ anhydrous	Fluka	≥ 98 %
Molecular sieve	Fluka, Union Carbide	type 3Å
NaCl	Fluka	≥ 99.5 %
$NaHCO_3$	Fluka	≥ 99.0 %
Na_2SO_3	Fluka	≥ 98 %
Na_2SO_4 anhydrous	Fluka	≥ 99.5 %
NH_4Cl	Fluka	≥ 99.5 %
$Pd(PPh_3)_4$	Fluka	≥ 97 %

$Pd(PPh_3)_2Cl_2$	Fluka	≥ 98 %
P_2O_5	Fluka	≥ 97 %
PtO_2	Across	83 % (Pt)
Pinacol anhydrous	Fluka	≥ 98 %
Pyridine	Across	≥ 99 %
Silica gel (SiO_2)	Brunschwig, 32-63, 60 Å	
Succinic anhydride	Across	≥ 99 %
Tetrahydrofurane	Across	99.9 %
Toluene	VWR, Prolabo	98 %
Trichlorosilane	Across	99 %
Triethylamine	Riedel de Haen	99 %
Triethylborate	Aldrich	99 %

3. Apparatus

All the apparatus used during this research are described in the next section. As our research was partly accomplished in the University of Tokyo as well as other universities, we also mention the equipment utilized outside of the University of Neuchâtel.

3.1. Nuclear Magnetic Resonance

University of Neuchâtel:

NMR measurements were carried out with a Varian Gemini XL-2000 spectrometer, ^{1}H at 200 MHz, ^{13}C at 50 MHz and ^{31}P at 162 MHz. Better resolutions were obtained with a Brucker AMX-400 spectrometer, ^{1}H at 400 MHz, ^{13}C at 100 MHz and ^{31}P at 162 MHz. The

frequencies as well as the solvent are specified in parentheses in each case. All the chemical shifts are given in parts per million (ppm) and the coupling constants *J* in Hertz (Hz). The internal standard for the proton spectrums are: (^{1}H) TMS (δ_H = 0.00 ppm) or $CHCl_3$ (δ_H = 7.26 ppm); for the carbon spectrums (^{13}C) $CDCl_3$ (δ_C = 77.00 ppm). To help the interpretation as well as the characterisation, low or short range HETCOR, COSY, DEPT or NOESY spectrum were measured. The deuterated solvents all came from Cambridge Isotope Laboratories. For the analysis, the peaks are denoted, s for singlet, d for doublet, t for triplet, q for quadruplet, dd for doublet of doublets, m for multiplet and br for a broad peak.

University of Tokyo:

^{1}H, ^{13}C and ^{31}P NMR spectra were recorded on JEOL type GSX-270 and GSX-500 spectrometers using a residual non deuterated solvent as an internal reference.

3.2 Electronic absorption spectroscopy (UV-Vis)

University of Neuchatel:

UU-Vis measurements were conducted on a Uvikon 930 spectrometer in a 10 mm path length quartz cell.

University of Tokyo:

UV-Vis spectrometry experiments were conducted on a JASCO type V-560 spectrometer in a 10 mm path length quartz cell.

3.3. Circular Dichroism (CD) spectrometry

University of Neuchâtel:

CD spectra were recorded with a JASCO 710 spectropolarimeter in a 10 mm path length quartz cell.

University of Tokyo:

CD analyses were performed on a JASCO type J-720 spectropolarimeter in a 10mm path length quartz cell.

3.4. Mass Spectroscopy (MS)

University of Neuchâtel:

ESI and APCI mass spectra were recorded with a LCQ-IT Finnigan spectrometer.

University of Tokyo:

Matrix-assisted laser desorption/ionization time-of-flight mass (MALDI-TOF-MS) spectrometry was conducted with dithranol as the matrix on an Applied Biosystems BioSpectrometry Workstation model Voyager-DE STR spectrometer.

Ecole Polytechnique Fédérale de Lausanne

Selected ion monitoring electro spray ionization mass spectroscopy (SIM ESI MS) was performed on a Thermo Finnigan LCQ Deca XP Plus quadrupole ion-trap instrument equipped with an offline nanoelectrospray source.

3.5. High Pressure Liquid Chromatography (HPLC)

University of Tokyo:

Preparative high performance liquid chromatography (HPLC) was performed on phosphineoxide scissors **55** at room temperature using a 20 mm- Ø × 250 mm long amylose column (DAICEL CHIRALPAK IA) on a Japan Analytical Industry Model LC-918 recycling preparative HPLC system using a mixture of CH_2Cl_2:ethanol 97:3 as eluent, equipped with a variable wavelength UV-Vis detector. Isomers *trans*-**55** and *cis*-**55** were isolated as the first and second fractions in analytical HPLC with a Mightysil Si 60 column using CH_2Cl_2:ethanol (97.5:2.5) as an eluent to determine their molar ratio.

3.6. Photoirradiations

University of Tokyo:

Photoirradiations were conducted at 20 °C on degassed CH_2Cl_2 solutions of samples in a 10 mm thick quartz cell under, using a 150 W xenon arc lamp with a band pass filter (Kenko) of $\lambda = 350 \pm 10$ nm for UV irradiations or a cut filter (Kenko) of $\lambda > 420$ nm for visible light illuminations.

3.7. Column gel permeation chromatography (column GPC)

Gel permeation chromatography was performed with a column filled with Bio-Beads S-X3 beads from Bio-Rad laboratories.

3.8. Supraconducting quantum interference device (SQUID)

University of Bern:

Magnetic susceptibility measurements were performed on a Quantum Designs MPMS SQUID-*XL* magnetometer in an applied field of 1000 G. Samples for measurement were prepared in saran foil bags.

4. Synthesis of phosphinated cyclopentadiene 39'

4.1 Synthesis of 2-(4-bromophenyle)-1,3-dioxolane (35) [101]

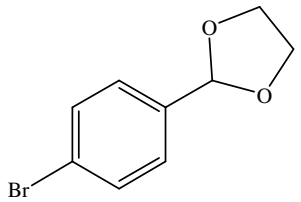

35

To a stirred solution of *p*-bromobenzaldehyde **34** (10.00 g, 54.00 mmol) in anhydrous toluene (60 ml), *p*-TSA (44 mg, 0.20 mmol) and ethylene glycol (5.00 g, 80.60 mmol) were added at room temperature under nitrogen. The solution was heated at reflux in a Dean-Stark appartus during 24 hours. The resulting mixture was allowed to cool down to room temperature and washed with a saturated aqueous solution of $NaHCO_3$ (20 ml) and a NaCl solution (20 ml). The organic extracts were dried over anhydrous $MgSO_4$ and the solvent evaporated under vacuum. The resulting yellow oil was purified by vacuum distillation (78°C, 0.23 mbar) to give the pure bromoacetal **35** as a colourless liquid; yield, 45.23 g (88%); ^{1}H NMR (400 MHz, $CDCl_3$, 22°C, ppm) δ 3.98-4.13 (m, 4H, OCH_2CH_2O), 5.77 (s, 1H, CH), 7.34-7.54 (m, 4H, H-Ar).^{13}C-NMR (100 MHz, $CDCl_3$, 22°C, ppm) δ 65.7 (s, 2C, OCH_2CH_2O), 103.4 (s, 1C, CH), 123.7 (s, 1C, Ar-Br), 128.6 (s, 2C, Ar-H), 131.9 (s, 2C, Ar-H), 137.5 (s, 1C, Ar-H).

4.2 Synthesis of [4-(1,3-dioxolane-yl)phenyl]diphenylphosphine (36) [101]

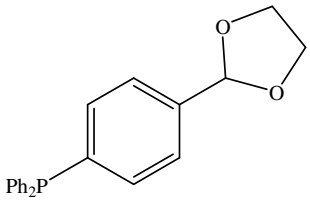

36

Butyl lithium (30.7 ml, 49.10 mmol, 1.6M in hexane) was added dropwise over 20 minutes to a stirred solution of bromo acetal **35** (9.13 g, 39.90 mmol) in THF (58 ml) at -78 °C under nitrogen. The solution was stirred at -78 °C during 40 minutes before a solution of chlorodiphenylphosphine (9.77 g, 44.30 mmol) in THF (48 ml) was added. The mixture was allowed to warm to room temperature, stirred 3 hours and quenched with an aqueous saturated solution of NH_4Cl (30 ml). The organic phase was washed with a brine solution (30 ml), dried with anhydrous $MgS0_4$ and the solvent removed under vacuum. Crude diphenylphosphine acetal **36** was recrystallized from ethanol and yielded the pure product as a white solid ; yield, 9.93 g, (75%); ^{1}H NMR (400 MHz, $CDCl_3$, 22°C, ppm) δ 4.03-4.15 (m, 4H, OCH_2CH_2O), 5.81 (s, 1H, CH), 7.31-7.49(m, 4H, H-Ar.), 7.50-7.84 (m, 10H, H-Ar.);^{13}C RMN (100 MHz, $CDCl_3$, 22°C, ppm) δ 65.8 (s, 2C, OCH_2CH_2O), 103.9 (s, 1C, CH), 127.0, 128.9, 129.2, 134.1, 137.3, 138.8, 138.9(s, 18C, C-Ar.); ^{31}P RMN (162 MHz $CDCl_3$, 22°C, ppm) δ -4.97 (s); APCI-MS positive mode: *m/z* = 335.20 ($[M+H]^+$ calculated: 335.35).

4.3 Synthesis of 4-(diphenylphosphino)benzaldehyde (37) [101]

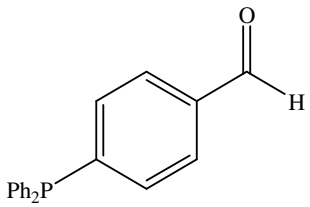

37

To a stirred solution of diphenylphosphine acetal **36** (2.50 g, 7.40 mmol) in THF (45 ml) and H_2O (5 ml), *p*-TSA (47 mg, 0.20 mmol) was added under nitrogen. The mixture was heated at reflux for 7 hours, cooled to room temperature and diluted with H_2O (10 ml). After extraction with ether (2 × 100 ml), the organic phases were dried with anhydrous $MgS0_4$ and the solvent was evaporated under vacuum. The crude product was purified by column chromatography with AcOEt:hexane (1:10) as eluent and afforded pure diphenylphosphine benzaldehyde **37** as a white solid; yield, 1.72 g (80%). ^{1}H NMR (400 MHz, $CDCl_3$, 22°C, ppm) δ 7.35-7.46 (m, 12H, H-Ar), 7.83 and 7.86 (dd, 2H, H-Ar), 10.03 (s, 1H, CHO); ^{13}C NMR (100 MHz, $CDCl_3$, 22°C, ppm) δ 129.1, 129.6, 133.9, 134.1, 136.3, 136.6, 136.0 (s, 18C, C-Ar), 192.0 (s, 1C, CHO); ^{31}P NMR (162 MHz, $CDCl_3$, 22°C, ppm) δ -3.05 (s); APCI MS positive mode: *m/z* = 291 ($[M+H]^+$ calculated: 291)

4.4 Synthesis of oxobutanoate (38) [102]

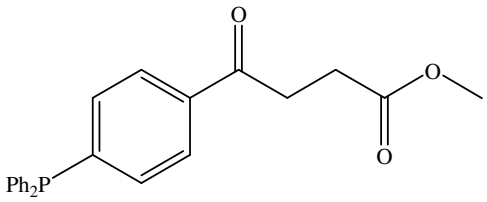

38

A solution of aldehyde **37** (3.00 g, 10.30 mmol) and sodium cyanide (87 mg, 1.80 mmol) in degased DMF (21 ml) was stirred 1 hour at room temperature and under nitrogen. Methyl acrylate (0.89 g, 10.3 mmol) in degased DMF (9 ml) were added dropwise over 30 minutes and the solution stirred 2 hours. The reaction was quenched (H_2O 60 ml) and the mixture was extracted with chloroform (3 × 50 ml). The organic extracts were washed with dilute aqueous solution of H_2SO_4 (100 ml), dilute aqueous solution of $NaHCO_3$ (100 ml) and H_2O (100 ml). After drying over anhydrous $MgSO_4$, the solvent was evacuated under vacuum. The resulting

product was purified by column chromatography with an EtOAc:Hexane 1:5 yielding phosphine oxobutanoate **38** as a yellowish oil; yield, 2.64 g (68%); ^{1}H NMR (400 MHz, $CDCl_3$, 22°C, ppm) δ 2.78 (t, 2H, CH_2COO), 3.31 (t, 2H, $OCCH_2$), 3.73 (s, 3H, OCH_3), 7.32-7.95 (m, 14H, H-Ar.); ^{13}C NMR (100 MHz, $CDCl_3$, 22°C, ppm) δ 27.9 (s, 1C, CH_2), 33.4 (s, 1C, CH_2), 51.8 (s, 1C, CH_3), 127.7, 128.7, 129.2, 133.2, 133.9, 134.05, 136.1, 144.6 (s, 18C, C-Ar), 173.3 (s, 1C, COO), 189.0 (s, 1C, CO). ^{31}P NMR (162 MHz, $CDCl_3$, 22°C, ppm) δ -4.29 (s); ESI MS positive mode: *m/z* = 376 ($[M]^+$ calculated: 376).

4.5 Synthesis of diphenylphosphineoxide cyclopentadiene 39'[103]

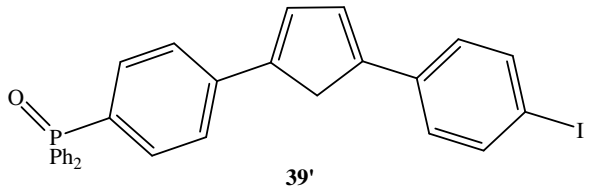

39'

To a stirred sodium ethoxyde (0.18 g, 2.72 mmol) in dry benzene (1.3 ml), iodoacetophenone in dry benzene (0.5 ml) was added over 30 minutes at 0°C under nitrogen. After it warmed to room temperature, the solution was added to oxobutanoate **38** (500 mg, 1.32 mmol) in dry benzene (1 ml). The mixture was heated at 40°C, stirred during 16 hours and quenched with H_2O at 0°C (2.2 ml). The aqueous phase was washed with toluene (3 × 2 ml) and heated at 70°C at which point cyclopentadiene phosphineoxide **39'** precipitated as a yellowish solid; yield, 150 mg (22%); ^{1}H NMR (400 MHz, $CDCl_3$, 22°C, ppm) δ 3.76 (s, 2H, Cp-H_2), 6.99 and 7.06 (dt, 2H, Cp-H), 7.30-7.79(m, 14H, H-Ar); ^{13}C NMR (100 MHz, $CDCl_3$, 22°C, ppm) δ 41.06 (s, 1C, C-Cp), 125.1, 127.1, 128.9, 129.3, 131.1, 132.3, 132.5, 133.0, 138.2 (s, 28C, Ar-C.); ^{31}P NMR (162 MHz $CDCl_3$, 22°C, ppm) δ 29.86 (s, P=O); ESI MS positive mode: *m/z* = 545 ($[M+H]^+$ calculated : 545).

5. Synthesis of chelating diphosphine scissor ligand 56

5.1. Synthesis of 4-(4-bromophenyl)-4-oxobutanoic acid (44) [83, 103]

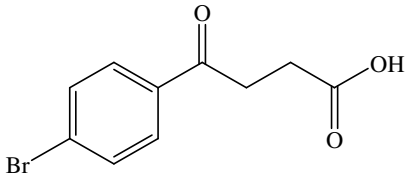

44

Commercially available anhydrous aluminium chloride (53.00 g, 0.40 mol) was added in one portion to a mechanically stirred mixture of powdered succinic anhydride (20.00 g, 0.10 mol) in bromobenzene (225 g, 0.62 mol) at -5 °C, under argon. The reaction temperature was maintained at -5 °C for 4 h and was then allowed to warm to room temperature. The reaction mixture was stirred at room temperature for 96 h (ceasing of HCl gas evolution indicating a completeness of the reaction). The reaction mixture was poured onto a mechanically stirred solution of dilute hydrochloric acid (500 ml, 18%) at 0 °C, and the mixture was stirred for a further 30 min while the solution was allowed to warm to room temperature. The yellowish white solid was filtered off, washed with water, and dried in vacuo ($CaCl_2$, P_2O_5, 1 day). The crude product was purified by recrystallization in toluene to afford a white crystalline solid (bromo oxobutanoic acid **44**) which was dried in vacuo ($CaCl_2$, P_2O_5, 1 day); yield, 45.23 g (88%); ^{1}H NMR (400 MHz, DMSO-d_6, 22°C, ppm) δ 2.59 (t, 2H, CH_2), 3.24 (t, 2H, $COOCH_2$), 7.75 (d, 2H, H-Ar), 7.92 (d, 2H, H-Ar), 12.18 (b, 1H, COOH); ^{13}C NMR (100 MHz, DMSO-d_6, 22°C, ppm) δ 28.77 (CH_2), 33.99 (CH_2), 128.16 (Ar-Br), 130.76 (2C, Ar-H), 132.67 (2C, Ar-H), 136.26 (Ar-C), 174.63 (COOH), 198.64 (CO).

5.2. Synthesis of oxobutanoate 45

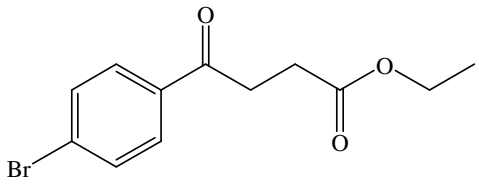

45

Concentrated H_2SO_4 (1 ml) was added to an EtOH solution (300 ml) of 4-(4-bromophenyl)-4-oxobutanoic acid **44** (36.00 g, 0.14 mol) under N_2 at room temperature. The solution was stirred at reflux for 20 h and allowed to come back at room temperature. After evaporation to dryness, a CH_2Cl_2 (300 ml) solution of the remainder was washed with a saturated aqueous solution of $NaHCO_3$ (250 ml) and water (250 ml). The organic phase was dried with Na_2SO_4 and evaporated under vacuum to afford pure oxobutanoate **45** as a white solid: yield, 38.13 g (96%); ^{1}H NMR (400 MHz, $CDCl_3$, 22°C, ppm) δ 1.26 (t, 3H, CH_3) 2.74 (t, 2H, CH_2), 3.26 (t, 2H, CH_2), 4.15 (q, 2H, $COOCH_2$), 7.59 (d, 2H, H-Ar), 7.83 (d, 2H, H-Ar); ^{13}C NMR (100 MHz, $CDCl_3$, 22°C, ppm) δ 14.60 (CH_3), 28.56 (CH_2), 33.70 (CH_2), 61.11 ($COOCH_2$), 128.75 (Ar-Br), 129.96 (2C, Ar-H), 132.31 (2C, Ar-H), 135.67 (Ar-C), 173.14 (COO), 197.53 (CO).

5.3. Synthesis of cyclopentadiene 46 [83, 102]

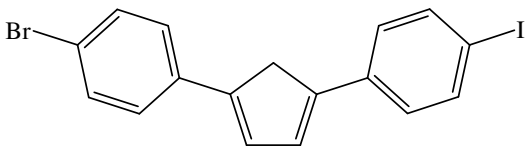

46

Oxobutanoate **45** (19.00 g, 66.00 mmol) and potassium *tert*-butoxyde (14.95 g, 0.13 mol) were placed under vacuum for 1 h and solubilized in dry benzene (80 ml) at 0 °C under N_2. After 30 min stirring, the solution was added with *p*-iodoacetophenon (16.44 g, 0.07 mol) in dry benzene (100 ml). The resulting in dark red mixture was stirred 24 h at 45 °C, cooled in ice water (500 ml) and stirred 30 min. The aqueous solution was washed with hexane (3 ×300 ml) and heated at 70 °C in an open flask until decarboxylation and precipitation occurred after 2h. After filtration, the yellow cyclopentadiene **46** was dried *in vacuo* ($CaCl_2$, P_2O_5, 1 day): yield, 10.61 g (38%); ^{1}H NMR (400 MHz, toluene-d_8, 22°C, ppm) 3.01 (s, 2H, Cp-H_2), 6.53 (m, 2H, H-Cp), 6.83 (d, 2H, H-Ar), 6.94 (d, 2H, H-Ar), 7.26 (d, 2H, H-Ar), 7.47 (d, 2H, H-Ar); MALDI-TOF-MS (dithranol): m/z = 423 ([M^+] calculated: 423).

5.4. Synthesis of tetrasubstituted ferrocene 47 [83, 104]

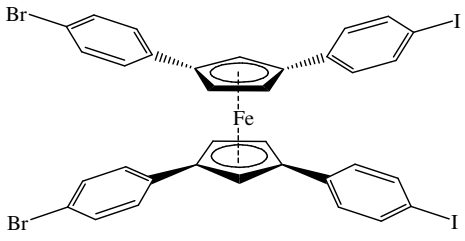

47

A dry THF solution (60 ml) of cyclopentadiene **46** (5.00 g, 11.80 mmol) was added at 0 °C with a solution of *t*-BuOK (1.50 g, 13.28 mmol) in dry THF (30 ml) under N_2 and stirred 1h. at 0 °C resulting in a brown-yellowish mixture. It was added to a gray suspension of $FeCl_2$ in dry THF which was prepared by refluxing anhydrous $FeCl_3$ (4.4 g, 27.00 mmol) and Fe powder under N_2 (3.50 g, 54.00 mmol) in dry THF (60 ml) during 5h [94]. After 20 h. at reflux, the reaction mixture was cooled down to room temperature and quenched with water (500 ml). It was then extracted with CH_2Cl_2 (2 × 600 ml), washed with brine solution and

dried with anhydrous Na_2SO_4. The solvent was evaporated under vacuum affording the crude ferrocene **47** was as a mixture of *meso* and racemic stereoisomers. Purification was carried out by recrystalisation in toluene to give a bright orange compound: yield, 3.45 g, (65 %); ^{1}H NMR (400 MHz, $CDCl_3$, 22°C, ppm) 4.52 (s, 4H, H-Cp), 4.82 (s, 2H, H-Cp), 6.84 (d, 4H, H-Ar), 6.96 (d, 4H, H-Ar), 7.25 (d, 4H, H-Ar), 7.44 (d, 4H, H-Ar); ^{13}C NMR (100 MHz, $CDCl_3$, 22°C, ppm) δ 65.73, 69.84, 69.95, 76.70, 86.64, 91.19, 100.48, 120.03,126.99, 127.25, 131.46, 134.91, 135.58, 137.40; MALDI-TOF-MS (dithranol): *m/z* = 900 ([M^+] calculated: 900).

5.5. Synthesis of dialkyne ferrocene 48 [83, 105]

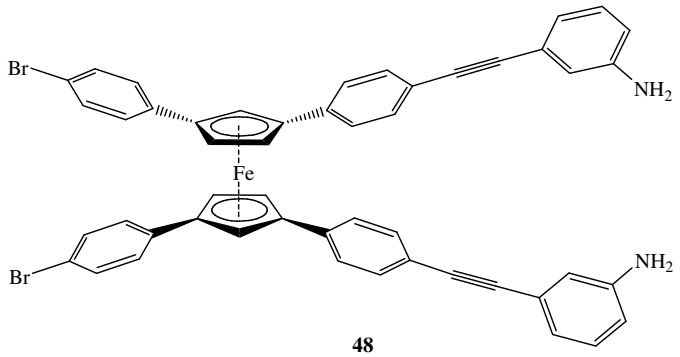

48

To a dry THF/Et_3N (20 ml/12 ml) suspension of tetrasubstituted ferrocene **47** (2.00 g, 2.22 mmol), CuI (20 mg, 0.11 mmol) and $PdCl_2(PPh_3)_2$ (16 mg, 22.79 μmol) was added 3-ethynylaniline (1.04 g, 8.88 mmol) under N_2. The reaction mixture was stirred overnight, quenched with water (500 ml) and extracted with CH_2Cl_2 (2 × 1000 ml). After being dried with anhydrous Na_2SO_4, the combined organic phases were evaporated under vacuum and the residue purified by column chromatography with CH_2Cl_2 as eluent. Dark orange dialkyne ferrocene **48** was produced as a mixture of *meso* and racemic stereoisomers; yield,1.87 g, (96 %); ^{1}H NMR (400 MHz, $CDCl_3$, 22°C, ppm) δ 3.67 (br, 4H, NH_2), 4.48 (s, 4H, H-Cp), 4.78 (s, 2H, H-Cp), 6.64-7.41 (m, 24H, H-Ar); ^{13}C NMR (100 MHz, $CDCl_3$, 22°C, ppm) δ 29.91,

65.18, 68.94, 85.57, 114.24, 115.21, 116.82, 117.37, 118.98, 124.37, 126.05, 128.35, 130.44, 121.95, 130.64, 145.29; MALDI-TOF-MS (dithranol): m/z = 878 ([M^+] calculated: 878).

5.6. Synthesis of hexaaryl ferrocene 49 [83, 106]

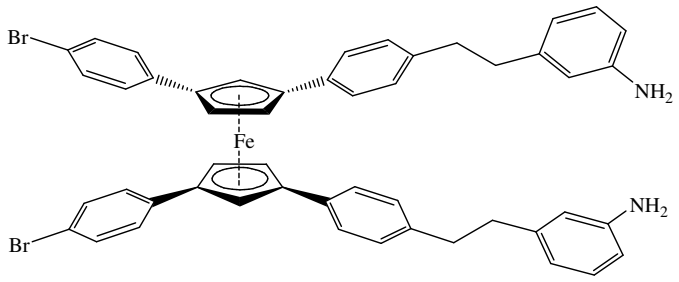

49

To a THF/ETOH (40 ml/20 ml) solution of dialkyne ferrocene **48** (0.50 g, 0.57 mmol) PtO_2 was added (0.05 g, 220. 19 μmol, 10 % mass). The solution was degassed by three freeze-pump-thaw cycles and pressurized with H_2 (1 atm.). The reaction mixture was stirred at room temperature and monitored by MALDI-TOF-MS until the alkyne was totally reduced (4 hours). After celite filtration and evaporation of the solvent, the remainder was purified by column chromatography with CH_2Cl_2 as the eluent. The reduced hexaaryl ferrocene **49** was recovered as a light-orange solid and as a mixture of *meso* and racemic stereoisomers; yield, 276.00 mg (55 %); ^{1}H NMR (400 MHz, $CDCl_3$, 22°C, ppm) δ 2.91 (s, 8H, CH_2), 3.61 (b, 4H, NH_2), 4.41(s, 4H, H-Cp), 4.73 (s, 2H, H-Cp), 6.51-7.27 (m, 24H, H-Ar); ^{13}C NMR (100 MHz, $CDCl_3$, 22°C, ppm) δ 30.96, 35.84, 37.5, 37.79, 66.3, 70.2, 85.8, 88.00, 112.59, 112.87, 115.32, 115.34, 118.86, 118. 91, 125.69, 125.78, 127.08, 127.16, 128.42, 129.31, 131.27, 131.33,140.01, 143.10, 146.48; MALDI-TOF-MS (dithranol): m/z = 886 ([M^+] calculated: 886).

5.7. Synthesis of bromo scissors (50) [83, 107]

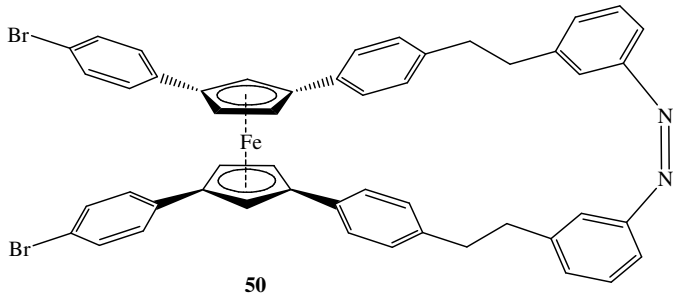

50

A dry pyridine (25 ml) solution of hexaaryl ferrocene **49** (0.10 g, 112.87 μmol) was added dropwise over 2 hours to CuCl (0.10 g, 1.01 mmol) and molecular sieves 3Å (1.00 g) in dry pyridine (25 ml). The suspension was stirred under air in the dark at room temperature during 12 h and neutralized with water (1000 ml). After CH_2Cl_2 (3 × 500 ml) extraction, the combined organic extracts were dried over anhydrous Na_2SO_4 and the solvent evaporated under vacuum. The crude orange residue was purified by column chromatography with CH_2Cl_2 as eluent to afford bromo scissors **50** as a dark orange solid and as a mixture of *meso* and racemic stereoisomers; yield, 31.00 mg (31 %); ^{1}H NMR (400 MHz, $CDCl_3$, 22°C, ppm) δ 2.92 (d, 4H, CH_2 of *cis*-**50)** 3.15 (d, 4H, CH_2 of *trans*-**50**), 3.24 (d, 4H, CH_2), 3.76 (s, 2H, H-Cp), 4.51 (s, 2H, H-Cp), 4.80 (s, 2H, H-Cp), 6.86-7.66 (m, 24H, H-Ar); MALDI-TOF-MS (dithranol): m/z = 882 ([M^+] calculated: 882).

5.8. Synthesis of (3-bromophenyl)diphenylphosphane (57) [109]

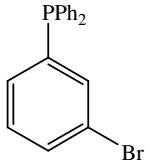

57

To commercially available 1,3-dibromobenzene (4.2 ml, 34.75 mmol) in dry THF (40 ml) at -90°C under argon, *n*-BuLi (1.6 M in hexane, 22.18 ml, 36.49 mmol) was added dropwise and the solution was stirred during 45 min. Chloro(diphenyl)phosphine (6.23 ml, 34.75 mmol) was added dropwise and the mixture was allowed to warm at room temperature. Filtration through a pad of celite, evaporation *in vacuo* and plug filtration with hexane as eluent yielded bromo triphenylphosphine **57** as a colourless viscous oil; 7.61 g yield, (64 %); ^{1}H NMR (400 MHz, $CDCl_3$, 22°C, ppm) δ 7.22-7.52 (m, 14H, H-Ar); ^{13}C NMR (100 MHz, $CDCl_3$, 22°C, ppm) δ 123.49, 123.57, 129.08, 129.16, 129.53, 130.44,130.51,132.15, 132.45, 132.64, 134.13,134.33, 136.32, 136.51,136.65, 136.77,140.90, 141.04; ^{31}P NMR (162 MHz, $CDCl_3$, 22°C, ppm) δ -4.06 (s).

5.9. Synthesis of 2-[3-(diphenylphosphanyl)phenyl]-4,4,5,5-tetramethyl-1,3,2-dioxoborolane (58) [109]

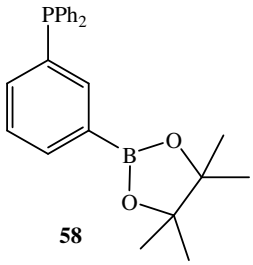

58

The bromo triphenylphosphine **57** (7.60 g, 22.18 mmol) was dissolved in dry THF (45 ml) and cooled to -90°C under Ar. *n*-BuLi (1.6 M in hexane, 14.63 ml, 23.41 mmol) was added dropewise and the solution stirred 1h. $(EtO)_3B$ (5.04 ml, 44.36 mmol) was added rapidly at -90°C, the reaction mixture allowed to warm at room temperature and the solvent evacuated under vacuum. The remainder was suspended in toluene (45 ml) and pinacol (2.91 g, 24.62 mmol) was added. The mixture was heated to reflux, neutralized with solid NH_4Cl (2.51 g,

46.92 mmol) and stirred 2 h. at reflux. After *in vacuo* removal of the solvent, the residue was dissolved in CH_2Cl_2 (150 ml). The solution was washed with saturated aqueous solutions $NaHCO_3$ (3 × 100 ml) and NaCl (3 × 100 ml), dried with anhydrous $MgSO_4$ and the solvent evaporated under vacuum. Column chromatography (hexane → hexane/CH_2Cl_2 4:1 → 3:2) afforded boronate phosphine **58** as a colourless viscous oil; yield, 1.62 g (19 %); ^{1}H NMR (400 MHz, $CDCl_3$, 22°C, ppm) δ 1.32 (s, 12H, CH_3), 7.28-7.70 (m, 12H, H-Ar), 7.80 (d,1H, H-Ar), 7.99 (d, 1H, H-Ar); ^{13}C NMR (100 MHz, $CDCl_3$, 22°C, ppm) δ 24.86, 83.89, 128.02, 128.06, 128.44, 128.50, 128.59, 128.67,132.24, 133.61, 133.80, 135.33, 136.13, 136.22, 140.85, 141.16; ^{31}P NMR (162 MHz, $CDCl_3$, 22°C, ppm) δ -5.90 (s), 29.73 (s, P=O).

5.10. Synthesis of dipheny[3-(4,4,5,5-tetramethyl-1,3,2-dioxaborolan-2-yl) phenyl]phosphane oxide (54) [109-110]

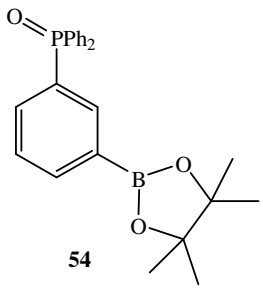

54

An acetonitrile (30 ml) solution of boronate phosphine **58** (1.62 g, 4.17 mmol), $FeCl_3 \cdot 6\ H_2O$ (102.00 mg, 0.38 mmol) and KSCN (77.00 mg, 0.79 mmol) was heated to 80°C and with vigorous O_2 bubbling. Iodine (tip of a spatula) was added and the solution was stirred 15 minutes before it was cooled down to room temperature. After *in vacuo* removal of the solvent, the residue was dissolved in $CHCl_3$ (100 ml), washed with 5 % aqueous solution of Na_2SO_3 (20 ml) and water (2 × 100 ml). The organic phase was dried with anhydrous $MgSO_4$, decolorized with active charcoal and filtered. After evaporation under vacuum, the residue

was recrystallized in (1:1, AcOEt:hexane) to afford the oxidised phosphine boronate **54** as cream coloured needles; yield, 1.67 g (99%); ^{1}H NMR (400 MHz, $CDCl_3$, 22°C, ppm) δ 1.31 (s, 12H, CH_3), 7.43-7.71 (m, 12H, H-Ar), 8.00 (d,1H, H-Ar), 8.30 (d, 1H, H-Ar); ^{13}C NMR (100 MHz, $CDCl_3$, 22°C, ppm) δ 25.27, 84.51, 127.97, 128.09, 128.84, 128.96; 131.57, 132.30, 132.48,132.53, 132.59, 133.56, 134.95, 135.05, 138.63, 138.74;^{31}P NMR (162 MHz, $CDCl_3$, 22°C, ppm) δ 29.76 (s, P=O).

5.11. Synthesis of ferrocenyldiphosphineoxide 55 [111]

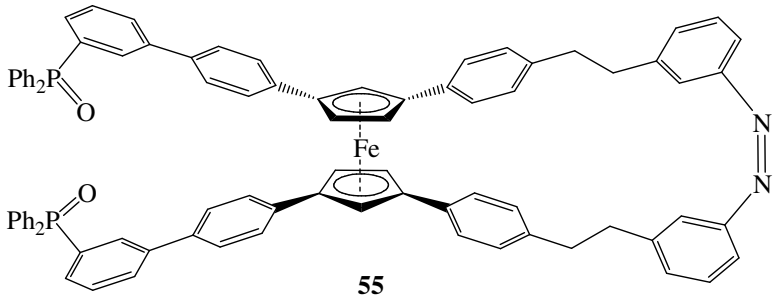

55

To a dry degassed DME (50 ml) solution of bromo scissors **50** (0.1 g, 0.11 mmol) and phosphineoxide boronate **54** (0.30 g, 1.13 mmol), $Pd(PPH_3)_4$ (20.00 mg, 17.32 μmol) and Cs_2CO_3 (243.00 mg, 1.26 mmol) were added under argon. The solution was heated to reflux, stirred overnight and the solvent removed. The residue was first subjected to column chromatography with EtOH/CH_2Cl_2 (3:97) as eluent and then further purified by GPC column (eluent: $CHCl_3$) to remove the excess of phosphine oxide boronate **54**. The mixture of *meso* and racemic isomers were separated through chiral preparative recycling HPLC with an eluent composed of EtOH/CH_2Cl_2 (3:97) that afforded three orange stereoisomers of ferrocenyldiphosphineoxide **55**; *meso*-**55**, enantiomer (+)-**55** and enantiomer (-)-**55**; respective yields, 26.00 mg (18 %), 11.00 mg (8 %), 13.00 mg (9%) (*cis* and *trans*-isomers);

The following spectra characterize *meso*-**55**, ^{1}H NMR (400 MHz, $CDCl_3$, 22°C, ppm) δ 2.93 (d, 8H, CH_2, *cis-meso*-**55**), 3.19 (d, 8H, CH_2, *trans-meso*-**55**), 4.14 (s, 4H, H-Cp), 4.42 (s, 2H, H-Cp), 6.52-8.14 (m, 52H, H-Ar); ^{13}C NMR (100 MHz, $CDCl_3$, 22°C, ppm) δ 18.45, 30.33, 34.82, 58.40, 71.13, 86.01, 89.04, 120.50, 122.88, 126.44, 126.61, 127.00, 128.56, 128.68, 128.92, 129.02, 130.24, 130.34,130.58, 130.69, 131.67, 131.95, 132.11, 132.22, 132.52, 132.98, 133.56, 135.67, 137.39, 138.49, 138.85, 142.10, 152.51; ^{31}P NMR (162 MHz, $CDCl_3$, 22°C, ppm) δ 29.54 (s, *cis*-P=O), 29.70 (s, *trans*-P=O); MALDI-TOF-MS (dithranol): *m/z* = 1277 ([M^+] calculated: 1277).

5.12. Synthesis of ferrocenyldiphosphine *meso*-56 [112]

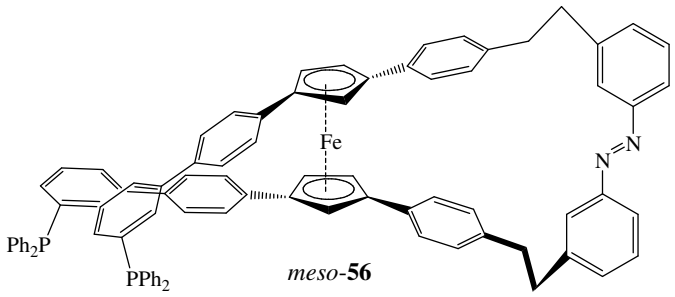

meso-**56**

A toluene/Et_3N (30 ml/3 ml) solution of ferrocenyldiphosphineoxide *meso*-**55** (26 mg, 20.36 μmol) was degassed by three freeze-pump-thaw cycles. $HSiCl_3$ (1.20 ml, 1.19 mmol) was added under argon and the reaction mixture heated at reflux and stirred overnight. After being cooled to room temperature, silica gel was added to the solution and the solvent evacuated under vacuum. The solid deposit was purified by column chromatography with CH_2Cl_2 as eluent to give *meso*-**56** (*cis* and *trans*-azo isomers)as an orange solid; yield, 17.00 mg (67 %); ^{1}H NMR (400 MHz, $CDCl_3$, 22°C, ppm) δ 2.93 (d, 8H, CH_2, *cis-meso*-**56**) 3.19 (d, 8H, CH_2, *trans-meso*-**56**), 3.78 (s, 2H, H-Cp), 4.49 (s, 2H, H-Cp), 4.88 (s, 2H, H-Cp), 7.13-7.93 (m,

52H, H-Ar); ^{31}P NMR (162 MHz, $CDCl_3$, 22°C, ppm) δ -2.72 (s, *cis*-P=O), -2.64 (s, *trans*-P=O); MALDI-TOF-MS (dithranol): *m/z* = 1245 ([M^+] calculated: 1245).

The same protocol was carried out for the reduction of the enantiomers (+)-**55** and (-)-**55**.

6. Coordination of ligand 56 to d^8 metals

6.1. Synthesis of *cis*-[$Rh(CO)_2$(*meso*-**56**)]$^+Cl^-$

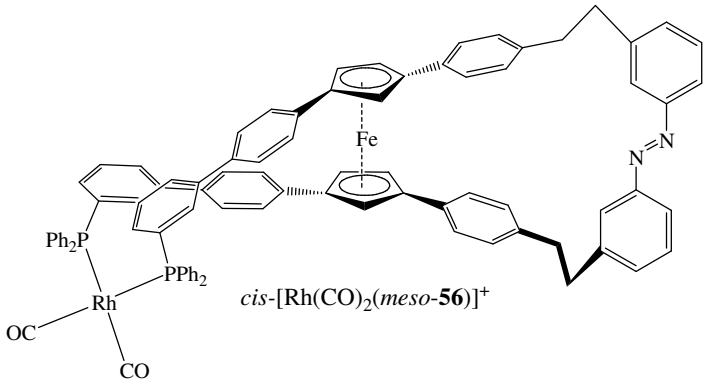

cis-[$Rh(CO)_2$(*meso*-**56**)]$^+$

A $CDCl_3$ (1.5 ml) solution of ferrocenyldiphosphine *meso*-**56** (14 mg,11.24 μmol) and $[RhCl(CO)_2]_2$ (2.18 mg, 5.62 μmol) was stirred overnight in an NMR tube under argon at room temperature; ^{1}H NMR (400 MHz, $CDCl_3$, 22°C, ppm) δ 3.18 (d, 8H, CH_2), 3.79 (s, 2H, H-Cp), 4.46 (s, 2H, H-Cp), 4.87 (s, 2H, H-Cp), 6.86-8.01 (m, 52H, H-Ar); ^{31}P NMR (162 MHz, $CDCl_3$, 22°C, ppm) δ 46.23 (d, P-Rh *trans-meso*-**56**, ^{1}J = 177 Hz), 46.54 (d, P-Rh *cis-meso*-**56**, ^{1}J = 178 Hz).

6.2. Synthesis of *cis*-[$Rh(CO)_2$((+)-56)]$^+Cl^-$

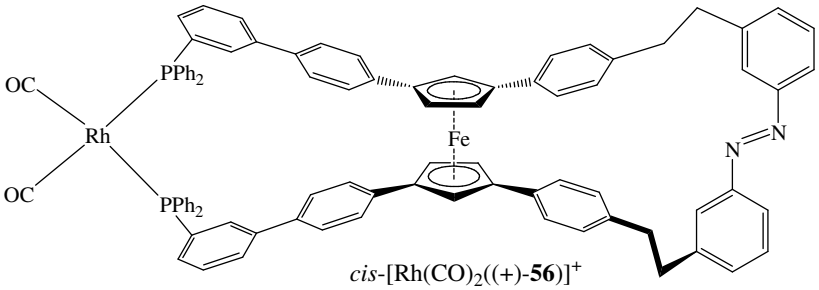

cis-[$Rh(CO)_2$((+)-**56**)]$^+$

A $CDCl_3$ (1.5 ml) solution of ferrocenyldiphosphine (+)-**56** (14 mg, 11.24 μmol) and $[RhCl(CO)_2]_2$ (2.18 mg, 5.62 μmol) was stirred overnight in an NMR tube under argon at room temperature; ^{31}P NMR (162 MHz, $CDCl_3$, 22°C, ppm) δ 48.06 (d, P-Rh *trans*-(+)-**56**, ^1J = 177 Hz), 51.27 (d, P-Rh *cis*-(+)-**56**, ^1J = 177 Hz).

6.3. Synthesis of *cis*-[$NiCl_2$(meso-56)]

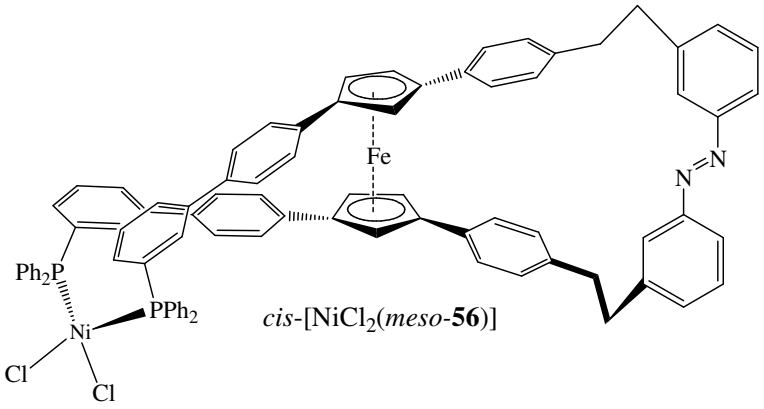

cis-[$NiCl_2$(*meso*-**56**)]

To a degassed dilute solution of ferrocenyldiphosphine *meso*-**56** (17 mg, 13.65 μmol) in EtOH (400 ml), [$NiCl_2$(DME)] (2.99 mg, 13.65 μmol) in DME (10 ml) was added under Ar. at room temperature. The reaction mixture was stirred overnight at 50°C and the solvent

removed *in vacuo* to afford complex *cis*-[$NiCl_2$(*meso*-**56**)] as a light-orange viscous solid (*cis* and *trans*-isomers); yield, 18.00 mg (96 %).

References

[1] Kinbara, K.; Aida, T. *Chem. Rev.* **2005,** 105.

[2] Yoshida, M.; Muneynki, E.; Hisabori, T. *Nat. Rev. Mol. Cell Biol.* **2001**, *2*, 669.

[3] Boyer, P. D. *Nature* **1999**, *402*, 247.

[4] Stock, D.; Leslie, A. G. W.; Walker, J. E. *Science* **1999**, *286*, 1700.

[5] Boyer, P. D. *Biochim. Biophys. Acta* **1993**, *1140*, 215.

[6] Abrahams, J. P.; Leslie, A. G. W.; Lutter, R.; Walker, J. E. *Nature* **1994**, *370*, 621.

[7] Noji, H.; Yasuda, R.; Yoshida, M.; Kinosita, K., Jr. *Nature* **1997**, *386*, 299.

[8] Menz, R. I.; Walker, J. E.; Leslie, A. G. W. *Cell* **2001**, *106*, 331.

[9] http://www2.bc.edu/~krilov/c_atp.html

[10] Yasuda, R.; Noji, H.; Kinoshita, K., Jr.; Yoshida, M. *Cell* **1998**, *93*, 1117.

[11] *Molecular Motors*; Schliwa, M., Ed.; Wiley-VCH: Weinheim, **2003**.

[12] Berg, H. C. *Annu. Rev. Biochem.* **2003**, *72*, 19.

[13] Namba, K.; Vonderviszt, F. *Q. Rev. Biophys.* **1997**, *30*, 1.

[14] Darnton, N.; Turner, L.; Breuer, K.; Berg, H. C. *Biophys. J.* **2003**, *86*, 1863.

[15] http://leisureguy.wordpress.com/2008/02/17/irreducible-complexity-is-reducible-after-all/

[16] Kabsch, W.; Mannherz, H. G.; Suck, D.; Pai, E. F.; Holmes, K. C. *Nature* **1990**, *347*, 37.

[17] Holmes, K. C.; Popp, D.; Gebhard, W.; Kabsch, W. *Nature* **1990**, *347*, 44.

[18] Mermall, V.; Post, P. L.; Mooseker, M. S. *Science* **1998**, *279*, 527.

[19] Sellers, J. R. *Biochim. Biophys. Acta* **2000**, *1496*, 3.

[20] Berg, J. S.; Powell, B. C.; Cheney, R. E. *Mol. Biol. Cell* **2001**, *12*, 780.

[21] De La Cruz, E. M.; Ostap, E. M. *Curr. Opin. Cell Biol.* **2004**, *16*, 61.

[22] Kühne, W. *Leipzig, Verlag von Wilhelm Engelmann* **1864**.

[23] http://finkbeiner.com/Editorial/Images/sarc.jpg

[24] Vale, R. D.; Reese, T. S.; Sheetz, M. P. *Cell* **1985**, *42*, 39.

[25] Nogales, E.; Whittaker, M.; Milligan, R. A.; Downing, K. H. *Cell* **1999**, *96*, 79.

[26] Lowe, J.; Li, H.; Downing, K. H.; Nogales, E. *J. Mol. Biol* **2001**, *313*, 1045.

[27] http://www.studiodaily.com/main/searchlist/6850.html

[28] http://www.blackwellpublishing.com/matthews/rhodopsin.html

[29] http://www.howelaboratory.harvard.edu

[30] Saibil, H. R.; Ranson, N. A. *Trends Biochem. Sci.* **2002**, *27*, 627.

[31] Wang, J.; Chen, L. *J. Mol. Biol.* **2003**, *334*, 489.

[32] Ishii, D.; Kinbara, K.; Ishida, Y.; Ishii, N.; Okochi, M.; Yohda, M.; Aida, T. *Nature* **2003**, *423*, 628.

[33] Feynman, R. P. *Eng. Sci.* **1960**, *23*, 22.

[34] Shinkai, S.; Nakaji, T.; Nishida, Y.; Ogawa, T.; Manabe, O. *J. Am. Chem. Soc.* **1980**, *102*, 5860.

[35] Shinkai, S.; Nakaji, T.; Ogawa, T.; Shigematsu, K.; Manabe, O. *J. Am. Chem. Soc.* **1981**, *103*, 111.

[36] Shinkai, S.; Ishiara, M.; Ueda, K. ; Manabe, O. *Chem. Commun.* **1984**, *11*, 727.

[37] Shinkai, S.; Ogawa, T.; Nakaji, T.; Kusano, Y.; Manabe, O. *Tetrahedron Lett.* **1979**, *20*, 4569.

[38] Shinkai, S.; Honda, Y.; Kusano, Y.; Manabe, O. *J. Chem. Soc., Chem. Commun.* **1982**, 848.

[39] Dürr, H.; Bouas-Laurent, H. ; Eds. *Photochromism*, Elsevier : Amsterdam, **1990**.

[40] Smets, G. *Adv. Polym. Sci*, **1983**, *50*, 17.

[41] Kaneko, A.; Tomoda, A.; Ishizuka, M.; Suzuki, H.; Matsushima, H. *Bull. Chem. Soc. Jpn*. **1988**, 61, 3569.

[42] Irie, M.; Sakemura, K.; Okinaka, M.; Uchida, K. *J. Org. Chem*. **1995**, *60*, 8305.

[43] Nakamura, S. ; Irie, M.; *J. Org. Chem*. **1988**, 53, 6136.

[44] Ushida, K. ; Matsuoka, K. ; Sayo, K.; Iwamoto, M; Hayashi, I. ; Irie, M. *Chem. lett*. **1999**, 835.

[45] Takeshita, M. ; Irie, M. *Tetrehedron. lett*. **1998**, *39*, 613.

[46] Takeshita, M. ; Irie, M. *J. Org. Chem*. **1998**, *63* , 6643.

[47] Takeshita, M. ; Irie, M. *J. Chem. Soc*., *Chem. Commun*. **1996**, 1807.

[48] Takeshita, M. ; Irie, M. *Chem. lett*. **1995**, 969.

[49] Gilat, S. L.; Kawai, H.; Lehn, J.-M. *Chem. Eur. J*. **1995**, *1*, 275.

[50] Gilat, S. L.; Kawai, H.; Lehn, J.-M. *J. Chem. Soc*., *Chem. Commun*. **1993**, 1439.

[51] Stobbe, H. *Ber*. **1905,** *38*, 3673.

[52] Darcy, P. J.; Heller, H.G.; Strydom, P.J.; Whitall, J. *J. Chem. Soc. Perkins Trans. 1*. **1981**, 202.

[53] Walz, J.; Ulrich, K.; Port, H.; Wolf, H. C.; Wonner, J.; Effenberg, F. *Chem. Phys. Lett*. **1993**, *213*, 321.

[54] Seibold, M.; Port, H.; Wolf, H.C. *Mol. Cryst. Liq. Cryst*. **1996**, *283*, 75.

[55] Koumura, N.; Zijistra, R. W. J.; van Delden, R. A.; Harada, N.; Feringa, B. L. *Nature* **1999**, *401*, 152.

[56] Koumura, N.; Geertsema, E. M.; Meetsma, A.; Feringa, B. L. *J. Am. Chem. Soc.* **2000**, *122*, 12005.

[57] Koumura, N.; Geertsema, E. M.; van Gelder, M. B.; Meetsma, A.; Feringa, B. L. *J. Am. Chem. Soc*. **2002**, *124*, 5037.

[58] Van Delden, R. A.; Koumura, N.; Schoevaars, A.; Meetsma, A.; Feringa, B. L. *Org. Biomol. Chem.* **2003**, *1*, 33.

[59] Schill, G. *Catenanes, Rotaxanes and Knots*; Academic Press: New-York and London, 1971.

[60] Pascard, C.; Guilhem, J.; Chardon-Noblat S.; Sauvage J.-P. *New J. Chem.* **1993**, *17*, 331.

[61] Deisenhofer, J.; Epp, O.; Miki, K.; Huber, R.; Michel, H. *J. Mol. Biol.* **1984**, *180*, 385.

[62] Huber, R. *Angew. Chem. Int. Ed. Engl.* **1989**, *28*, 848.

[63] Deisenhofer, J.; Michel, H. *Angew. Chem. Int. Ed. Engl.* **1989**, *28*, 848.

[64] Woodburry, N. W.; Becker, N.; Middendorf, D.; Parson W. W. *Biochemistry* **1985**, *24*, 7516

[65] Breton, J.; Martin, J.-L.; Migus, A. ; Antonetti, A. ; Orszag, A. *Proc. Natl. Acad. Sci. U.S.A* **1986**, *83*, 5121.

[66] Martin, J.-L.; Breton, J.; Hoff, A. J.; Migus, A. ; Antonetti, A. *Proc. Natl. Acad. Sci. U.S.A* **1986**, *83*, 957.

[67] Chardon-Noblat, S.; Sauvage J.-P. *Tetrahedron* **1991**, *47*, 5123.

[68] Heitz, V.; Chardon-Noblat, S.; Sauvage, J.-P. *Tetrahedron Lett.* **1991**, *32*, 197.

[69] Brun, A. M.; Atherton, S.; Harriman, A.; Heitz, V.; Sauvage J.-P. *J. Am. Chem. Soc.* **1992**, *114*, 4632.

[70] Chambron, J.-C.; Heitz, V.; Sauvage J.-P. *J. Am. Chem. Soc.* **1993**, *115*, 12378.

[71] Chambron, J.-C.; Heitz, V.; Sauvage J.-P. *J. Chem. Soc., Chem. Commun.* **1992**, 1131.

[72] Livoreil, A.; Dieterich-Buchecker, C. O.; Sauvage J.-P. *J. Am. Chem. Soc.* **1994**, *116*, 9399.

[73]] Livoreil, A.; Sauvage J.-P.; Armaroli, N.; Balzani, V.; Flamigni, L.; Ventura, B. *J. Am. Chem. Soc.* **1997**, *119*, 12114.

[74] Collin, J.-P.; Dietrich-Buchecker, C.; Gavina, P.; Jimenez-Molero, M. C.; Sauvage, J.-P. *Acc. Chem. Res.* **2001**, *34*, 477.

[75] Jimenez, M. C.; Dietrich-Buchecker, C.; Sauvage, J.-P. *Angew. Chem. Int. Ed.* **2000**, *39*, 3284.

[76] Jimenez-Molero, M. C.; Dietrich-Buchecker, C.; Sauvage, J.-P. *Chem. Eur. J.* **2002**, *8*, 1456.

[77] Jimenez-Molero, M. C.; Dietrich-Buchecker, C.; Sauvage, J.-P. *Chem. Commun.* **2003**, 1613.

[78] Lutz, A.; Ward, T.; Albrecht, M. *J. Chem. Soc.* **1962**, 693

[79] Lutz, A.; Ward, T. *Helv. Chim. Acta* **1998**, *81*, 207

[80] Zelikovich, L.; Libman, J.; Shanzer, A. *Nature* **1995**, *374*, 790.

[81] De Silva, A. P.; McClenaghan, N. D. *Chem. Eur. J.* **2004**, *10*, 574.

[82] De Silva, A. P.; Gunaratne, H. Q. N.; McCoy, C. P. *J. Am. Chem. Soc.* **1997**, *119*, 7891.

[83] Muraoka, T.; Kinbara, K.; Kobayashi, Y.; Aida, T. *J. Am. Chem. Soc.* **2003,** *125*, 5612.

[84] Muraoka, T.; Kinbara, K.; Aida, T. *Nature* **2006,** *440*, 512.

[85] Muraoka, T.; Kinbara, K.; Aida, T. *Chem. Commun.* **2007**, 1441.

[86] Muraoka, T.; Kinbara, K.; Wakamiya, A.; Yamaguchi, S.; Aida, T. *Chem. Eur. J.* **2007**, *13*, 1724.

[87] Muraoka, T.; Kinbara, K.; Aida, T. *J. Am. Chem. Soc.* **2006**, *128*, 11600.

[88] Cambi, L.; Szego, L. *Ber. Drsch. Chem. Ges.* B **1931**, *64*, 259.

[89] Kahn, O.; Jay Martinez, C. *Science* **1998**, *279*, 44.

[90] Boillot, M.-L.; Sour, A.; Delhaès, P.; Mingotaud C.; Soyer, H. *Coord. Chem. Rev.* **1999,** *190–192*, 47.

[91] Decurtins, S.; Gütlich , P.; Kohler, C. P.; Spiering, H.; Hauser, H. *Chem. Phys. Lett.* **1984**, *105*, 1.

[92] Hauser, A. *Chem. Phys. Lett.* **1986**, 1*24*, 543.

[93] Hayami, S.; Gu, Z. Z.; Shiro, M.; Einaga, Y.; Fujishima, A.; Sato, O. *J. Am. Chem. Soc.* **2000,** *122,* 7126.

[94] Browning, M. C.; Mellor, J. R.; Morgan, D. J.; Pratt, S. A.; Sutton, L. E.; Venanzi, L. M. *J. Chem. Soc.* **1962**, 693.

[95] Evans, D. A.; Thomson, R. J. *J. Am. Chem. Soc.* **2005,** *127,* 10506.

[96] Imamura, Y.; Mizuta, T.; Miyoshi, K. *Organomettalics* **2005**, *25*, 882.

[97] Kuang, S. M.; Cutteli, D. G.; McMillin, D. R.; Fanwick, P. E.; Walton, R. A. *Inorg. Chem.* **2002**, *41*, 3313.

[98] Heins, W.; Stossel, P.; Mayer, H.A.; Fawzi, R.; Steinmann, M. *J. Organometal. Chem.* **1999**, *587*, 258.

[99] Peluso, A.; Salahub, D.R.; Goursot, A. *Inorg. Chem.* **1990**, *29*, 1544.

[100] Summerville, R. H.; Hoffmann, R. *J. Am. Chem. Soc* **1976**, *98*, 7240

[101] Hon, Y.-S.; Lee, C.-F.; Chen, R.-J.; Szu, P.-H. *Tetrahedron* **2001,** *57*, 5991.

[102] Stetter, H.; Schreckenberg, M.; Wiemann, K. *Chem. Ber.* **1976**, *109*, 541.

[103] Drake, N. L. & Adams, J. R., Jr, *J. Am. Chem. Soc.* **1939**, *61*, 1326.

[104] Sonpatki, V. M.; Herbert, M. R.; Sandvos, L. M.; Seed, A. J. *J. Org. Chem.* **2001**, *66*, 7283.

[105] King, R. B.; Bisnette, M. B. *J. Organometal. Chem.* **1967**, *8*, 287.

[106] Sonogashira, K.; Tohda, Y.; Hagihara, N. A. *Tetrahedron Lett.* **1975**, *50***,** 4467.

[107] Just, G.; Wang, Z. Y.; Chan, L. *J. Org. Chem.* **1988**, *53*, 1030.

[108] Kinoshita, K. *Bull. Chem. Soc. Jpn.* **1952**, *32*, 777.

[109] Lustenberger, P.; Diederich, F. *Helv. Chim. Acta* **2000**, *83*, 2865.

[110] Ondrejkovikova, I.; Vancova, V.; Ondrejovic, G. *Collect. Czech. Chem. Commun.* **1983**, *48*, 254.

[111] Miyaura, N.; Suzuki, A. *Chem. Rev.* **1995***, 95***,** 2457.

[112] Henschke, J. P.; Burk, M. J.; Malan, C. G.; Herzberg, D.; Peterson, J. A.; Wildsmith, A. J.; Cobley J. C.; Casy, G. *Adv. Synth. Catal.* **2003***, 345*, 300.

[113] Hierso, J.C.; Fihri, A. ; Ivanov, V.V. ; Hanquet, B. ; Pirio, N. ; Donnadieu, B. ; Rebiere, B.; Amardeil, R.; Meunier, P. *J. Am. Chem. Soc*., **2004**, *126*, 11077.

[114] Widhalm, M.; Kratky, C. *Chem. Ber*. **1992**, *125*, 679.

[115] Bianchini. C.; Oberhauser, W.; Orlandini, A.; Giannelli, C.; Frediani, P. *Organometallics* **2005**, *24*, 3692.

[116] Smith, R. C.; Protasiewicz, J. D. *Organometallics* **2004,** *23,* 4215.